Jansen, E., Raymo, M.E., Blum, P., et al., 1996
*Proceedings of the Ocean Drilling Program, Initial Reports,* Vol. 162

# 9. SITE 986[1]

Shipboard Scientific Party[2]

## HOLE 986A

**Position:** 77°20.438′N, 9°04.661′E

**Start hole:** 1215 hr, 10 August 1995

**End hole:** 1230 hr, 11 August 1995

**Time on hole:** 24.25 hr (1.01 days)

**Seafloor (drill pipe measurement from rig floor, mbrf):** 2062.9

**Total depth (drill pipe measurement from rig floor, mbrf):** 2268.9

**Distance between rig floor and sea level (m):** 11.4

**Water depth (drill pipe measurement from sea level, m):** 2051.5

**Penetration (mbsf):** 206.0

**Coring totals:**
- Type: APC
  Number: 14
  Cored: 113.9 m
  Recovered: 121.26 m, 106.5%
- Type: XCB
  Number: 10
  Cored: 92.1 m
  Recovered: 60.04 m, 65.2%
- Total:
  Number: 24
  Cored: 206.0 m
  Recovered: 181.30 m, 88.0%

**Formation:**
- Unit I: 0–98.0 mbsf; Holocene to late Pleistocene; silty clay, clay with silt, nannofossil mixed sediment
- Unit II: 98.0–206.0 mbsf; late Pleistocene; silty clay, clay with silt, many dropstones

## HOLE 986B

**Position:** 77°20.431′N, 9°04.664′E

**Start hole:** 1230 hr, 11 August 1995

**End hole:** 1430 hr, 11 August 1995

**Time on hole:** 2.00 hr (0.08 days)

**Seafloor (drill pipe measurement from rig floor, mbrf):** 2064.5

**Total depth (drill pipe measurement from rig floor, mbrf):** 2080.0

**Distance between rig floor and sea level (m):** 11.4

**Water depth (drill pipe measurement from sea level, m):** 2053.1

**Penetration (mbsf):** 15.5

**Coring totals:**
- Type: APC
  Number: 2
  Cored: 15.5 m
  Recovered: 15.10 m, 97.4%

**Formation:**
- Unit I: 0–15.5 mbsf; Holocene to late Pleistocene; silty clay, clay with silt, nannofossil mixed sediment

## HOLE 986C

**Position:** 77°20.431′N, 9°04.664′E

**Start hole:** 1430 hr, 11 August 1995

**End hole:** 1500 hr, 14 August 1995

**Time on hole:** 72.50 hr (3.02 days)

**Seafloor (drill pipe measurement from rig floor, mbrf):** 2063.0

**Total depth (drill pipe measurement from rig floor, mbrf):** 2471.0

**Distance between rig floor and sea level (m):** 11.5

**Water depth (drill pipe measurement from sea level, m):** 2051.5

**Penetration (mbsf):** 408.0

**Coring totals:**
- Type: APC
  Number: 8
  Cored: 71.8 m
  Recovered: 69.58 m, 96.9%
- Type: XCB
  Number: 36
  Cored: 336.2 m
  Recovered: 160.20 m, 47.7%
- Total:
  Number: 44
  Cored: 408.0 m
  Recovered: 229.78 m, 56.3%

**Formation:**
- Unit I: 0–98.0 mbsf; Holocene to late Pleistocene; silty clay, clay with silt, nannofossil mixed sediment
- Unit II: 98.0–408.0 mbsf; late to early Pleistocene; silty clay, clay with silt, many dropstones

## HOLE 986D

**Position:** 77°20.408′N, 9°04.654′E

**Start hole:** 1500 hr, 14 August 1995

**End hole:** 2100 hr, 20 August 1995

**Time on hole:** 150.00 hr (6.25 days)

**Seafloor (drill pipe measurement from rig floor, mbrf):** 2063.0

**Total depth (drill pipe measurement from rig floor, mbrf):** 3027.6

[1]Jansen, E., Raymo, M.E., Blum, P., et al., 1996. *Proc. ODP, Init. Repts.,* 162: College Station, TX (Ocean Drilling Program).
[2]Shipboard Scientific Party is given in the list preceding the Table of Contents.

**Distance between rig floor and sea level (m):** 11.5

**Water depth (drill pipe measurement from sea level, m):** 2051.5

**Penetration (mbsf):** 964.6

**Drilled interval (mbsf):** 0–387.8

**Coring totals:**

Type: RCB
Number: 60
Cored: 576.8 m
Recovered: 241.56 m, 41.9%

**Formation:**

Unit I: 0–98.0 mbsf; Holocene to early Pleistocene; silty clay, clay with silt, nannofossil mixed sediment

Unit II: 98.0–561.8 mbsf; late to early Pleistocene; silty clay, clay with silt, many dropstones

Unit III: 561.8–820.3 mbsf; late Pleistocene to early Pliocene; clayey silt with sand, silty clay with sand

Unit IV: 820.3–964.6 mbsf; (?)early Pliocene; silty clay, clay with silt.

**Principal results:** Four holes were drilled at Site 986 (SVAL-1), with a maximum penetration of 964.6 mbsf. The sequence penetrates all the main regional reflectors (R1–R7) of the Svalbard–Barents Sea margin, with good ties to the reflectors and main seismic sequences shown by core physical property measurements and wireline logging. This major objective was successfully reached, enabling a documentation of the main phases of glacial erosion and deposition on the margin. The sediments recovered are predominantly fine- to coarse-grained siliciclastics with varying amounts of gravel. Dropstones (>1.0 cm in size) are abundant in most cores of the upper sedimentary sequence (0–561.8 mbsf). Sedimentary rocks are common among the dropstones throughout this sequence, whereas igneous and/or metamorphic rock fragments are more common in the interval from 380 to 550 mbsf. Over 500 dropstones greater than 1.0 cm in size are present from 2.58 through 845.3 mbsf.

High methane content in the rapidly deposited sediments and high dropstone content lead to variable recovery. However, all main units are documented by recovery, and important additional information from wireline logging of the upper 500 m of the sequence enables a comprehensive description of the formations, consisting of four lithostratigraphic units. A composite section was developed for the upper 210 mcd of Site 986, providing relative alignments between adjacent holes but confirmed overlap was maintained only through the top 60 mcd.

Unit I (0–98.0 mbsf, Holocene to late Pleistocene) is primarily defined by the presence of relatively common calcareous nannofossils. The lower boundary of this unit is marked by a decrease in the silt content. The sediments of Unit I are predominantly dark gray to very dark greenish gray silty clay and clay with silt, with interbedded layers of more nannofossil-rich sediments. Numerous dropstones, some as large as 7.9 cm, were identified throughout this Unit.

Unit II (98.0–561.8 mbsf; late to early Pleistocene) comprises the bulk of the sedimentary sequence at Site 986. The unit is composed exclusively of dark to very dark greenish gray and dark to very dark gray silty clay and clay with silt. The most significant change is the increase in the amount of dropstones within this unit. Up to 30 dropstones per core as large as 16.5 cm were found throughout this unit. Numerous well-defined millimeter- to decimeter-scale sandy to silty layers characterize the sediments of the uppermost part of this unit. Reworked shell fragments commonly appear in the uppermost 230 mbsf. In addition, wireline logging results show an increased number of intervals larger than 10 m thick that have increased resistivity and low magnetic susceptibility within the interval from 235 to 550 mbsf. These intervals are interpreted as debris-flow deposits.

Unit III (561.8–820.3 mbsf; late to middle Pliocene[?]) is primarily characterized by relatively high sand content and the absence of dropstones. The primary lithologies of Unit III are very dark gray to very dark greenish gray silty clay with sand, clayey silt with sand, silty clay, and sandy silty clay. Unit III is characterized by the re-occurrence of biogenic calcareous sediment, which is present throughout the unit.

Unit IV (820.3–964.6 mbsf; middle Pliocene[?]) comprises the deepest sediments recovered at this site (Hole 986D). The transition from Unit III to Unit IV is marked by a gradual decrease in sand-sized grains and in the amount of silt- to sand-sized terrigenous components.

Although age constraints are relatively poor throughout the sedimentary sequence, sedimentation rates at Site 986 appear to have remained between 160 and 320 m/m.y. from the Pliocene to Holocene. Post-cruise work will concentrate on improving the shipboard chronology. Shipboard biostratigraphic and paleomagnetic age indications for the bottom of the sequence are not consistent. Foraminifer and calcareous nannofossil evidence indicate an age between 3.6 and 2.4 Ma for the sequence below 700 mbsf, whereas dominantly reversed magnetization in the lower sequence may indicate an even younger age. The shipboard results document that the main fan buildup on the Svalbard Margin happened during the Pliocene–Pleistocene, due to glacial erosion/deposition. A major shift in glacial style and ice-sheet size took place in the Quaternary, characterized by the onset of excessive debris-flow sedimentation, probably originating from ice sheets grounded at the shelf break. During the first phase of this development debris flows were more conspicuous and thicker (Unit II) than during the later stages (Unit I).

Methanogenesis occurs as shallow as 20 mbsf at Site 986 due to the high sedimentation rates. High methane content prevails throughout the section, with higher hydrocarbons increasing in abundance with burial depth. A low salinity level at about 50 mbsf may indicate possible decomposition of methane clathrates, whereas a strong reduction in chlorine content and salinity deeper in the hole may be due to dewatering of clays under the influence of high heat flow. Downhole temperature measurements and shipboard thermal conductivity measurements document higher heat flux (151 W/m$^2$) at the site than was anticipated.

## BACKGROUND AND OBJECTIVES

Site 986 (SVAL-1B) was drilled on the Svalbard Margin (Fig. 1) to examine the onset of glaciation in the European Arctic and establish the history of the Svalbard–Barents Sea Ice Sheet, including a probable transition from a terrestrial- to marine-based ice sheet in the Barents Sea. The initial phase of the late Cenozoic glaciation was most likely in the form of limited mountain, valley, and fjord glaciers reaching sea level. The Svalbard archipelago, which probably has been subaerially exposed since at least the Miocene, may represent, due to its northern position in the high Arctic, the likely location for the initiation of Pliocene glaciation in the European Arctic (Faleide et al., 1996).

Basic information on the development of the north European glaciations and late Cenozoic paleoclimatic history has been obtained from the results of drilling on the Vøring Plateau in the Norwegian-Greenland Sea, ODP Leg 104, and on the Iceland and Yermak Plateaus, Leg 151. Stable isotope and ice-rafted debris (IRD) data indicate the onset of an early stage of glaciation and climatic cooling from about 12 Ma, with intensification at about 7 Ma, a major stage of intensified glaciations in northern Europe from 2.72 Ma, and increased IRD deposition in response to the shift to 100-k.y. cycles at about 1 Ma (Jansen et al., 1988; Jansen and Sjøholm, 1991; Wolf and Thiede, 1991; Myhre, Thiede, Firth, et al., 1995; Fronval and Jansen, in press). The location and size of pre-2.72-Ma ice sheets are still poorly constrained. It is important for our understanding of the transformation of the climate system into the ice-age world with increased sensitivity to orbital forcing to identify where and why ice sheets started to form. In the Pliocene–Pleistocene, three major ice sheets have terminated along the margins of the Nordic Seas: the Greenland, Scandinavian, and Svalbard–Barents Sea Ice Sheets. Information on the inception, variability, and dynamics of these ice masses needs to be assessed individually for each ice sheet, in order to understand which areas are the most sensitive to early ice-sheet growth, when glaciation style shifted from mountain-and-fjord-style glaciation to

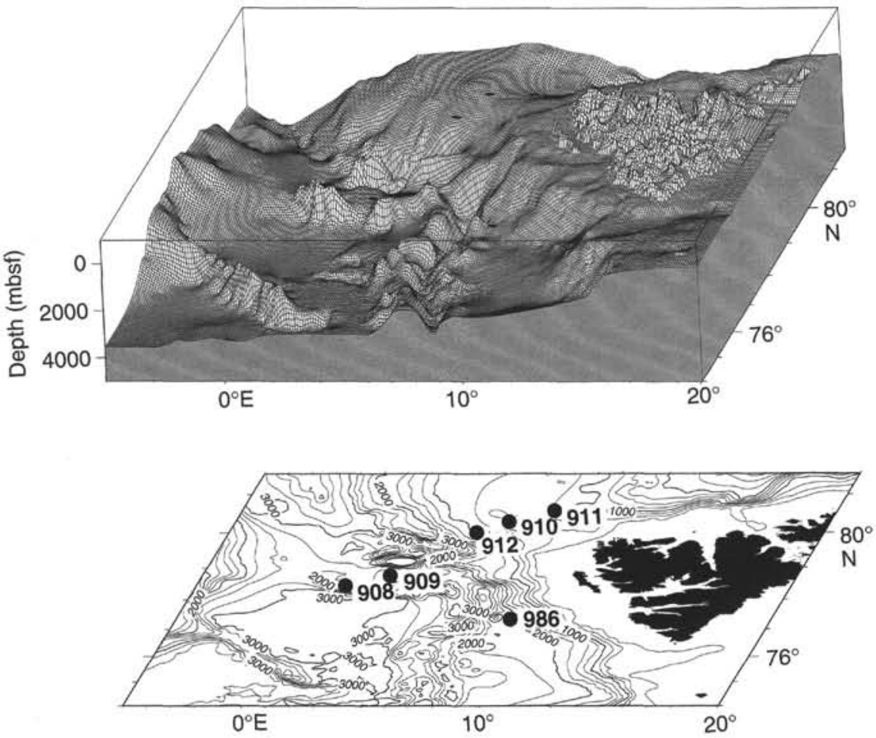


Figure 1. Bathymetry of the Svalbard Margin, Yermak Plateau, and Barents Sea, showing location of Site 986 (Leg 162) and Sites 908–912 (Leg 151).

full-fledged ice sheets, and when marine-based ice sheets extending to the outer shelf area started to form. Drilling in relatively proximal areas of the ice masses is necessary to obtain this information. Sites 986 and 987 (EGM-4) are therefore located on the lower continental slope adjacent to the Svalbard–Barents and Greenland Ice Sheets, respectively.

Recently, the importance of glacial erosion has been discussed in relation to late Cenozoic uplift and mountain range formation (Molnar and England, 1990; Riis and Fjeldskaar, 1989). The Svalbard–Barents Sea platform represents more than 1 million km$^2$ of drainage area, and the 2–4-km-thick late Cenozoic glaciogenic wedges along the margin indicate extensive glacial erosion of the platform, varying from 0.5 km in the south to 1.5 km in the northwest (Eidvin et al., 1993; Faleide et al., 1996; Solheim et al., 1996a) (Fig. 2). Thus, the region represents an area where increased erosion as a mechanism for uplift can be investigated. Isopach maps of the glaciogenic sediments have been produced for the entire western Svalbard–Barents Sea margin (Fig. 2).

The glacial sediment sequence has been divided into seven seismic sequences which can be followed from south of the Bear Island Fan to the northwestern part of Svalbard (Fig. 3) (Faleide et al., 1996). Seismic stratigraphy represents a key element in the paleoenvironmental reconstruction of the Svalbard–Barents Sea platform. However, the sequences have not yet been dated. At Site 986, which is located between two glacial fans and has a good tie to the regional seismic grid, we intend to date these major seismic reflectors, verify their true nature, and thus determine the onset and main phases of glacial erosion and deposition. This will also enable calculation of sediment flux and erosion rates during different glacial phases.

During Leg 151, glacial sequences were drilled on the Yermak Plateau (Sites 910, 911, and 912). None of these, however, penetrated the thick young glacial package; hence, it was not possible to date the onset of widespread glaciation on the Arctic shelf of Svalbard (Myhre, Thiede, Firth, et al., 1995; Flower, in press). The presence of overconsolidated sediments at Site 910 suggests that grounded glaciers existed on the Yermak Plateau in the Brunhes Chron (Myhre,

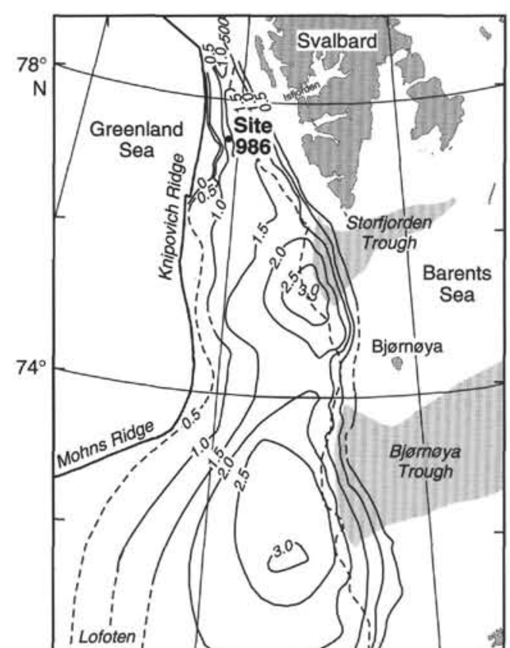


Figure 2. Isopach map of glacial fans off the Svalbard–Barents Sea region (from Faleide et al., 1996). Position of Site 986 is indicated. Isopachs are in seconds two-way traveltime.

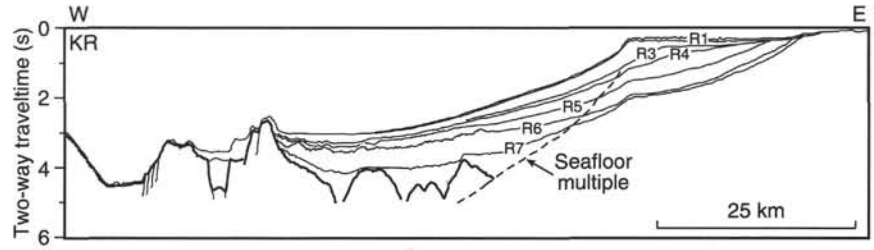


Figure 3. Main regional seismic units of the Svalbard Margin (from Faleide et al., 1996). KR = Knipovich Ridge.

Thiede, Firth, et al., 1995). These were probably times when ice sheets may have formed northward lobes onto the Arctic Ocean shelf. The extent to which these ice sheets became marine-based is important for understanding glacial cyclicity and rapid climate change. The Svalbard–Barents Sea Ice Sheet has been suggested to be a main trigger for rapid deglaciations (Jones and Keigwin, 1988; Berger and Jansen, 1994) due to its marine-based character in the late Quaternary. A shift from terrestrial- to marine-based glaciation in the middle Pleistocene has also been proposed as a cause of the changing style of glaciation from smaller 40-k.y. cycles to larger 100-k.y. cycles with rapid deglaciations (Terminations) at about 1 Ma (Berger and Jansen, 1994). By drilling through the main glacial sequences, and dating the steps in glaciation style, we should be able to test some of these hypotheses.

## OPERATIONS

The vessel covered the 685 nmi to Site 986 (SVAL-1) at an average speed of 11.9 kt and encountered no difficulties while underway. At 0642 hr on 10 August 1995 the vessel slowed to survey speed (5.3 kt) and a seismic survey was carried out near the drill site. The purpose of the survey was mainly to offset the drill site slightly from the proposed site (SVAL-1) to avoid drilling through the entire thickness of a major debris flow identified in the pre-cruise data (see "Seismic Stratigraphy" section, this chapter). Once the survey had been completed the ship returned to the site coordinates using GPS data.

The operational plan for this site called for drilling two APC holes to refusal or approximately 200 mbsf. One hole was to be deepened to XCB refusal, estimated to occur at about 500 mbsf. The third hole was to be drilled down just short of the XCB hole total depth and then continuously RCB cored to a depth of 900 mbsf. This hole would not penetrate basement but would drill thorough the entire glacial sediment package, which constituted the major site objective.

Core orientation was not considered due to the high latitude of the site. A minimum number of Adara temperature measurements were to be taken in the upper (APC) portion of the hole in order to establish a temperature gradient for the site. A full suite of logging tools was to be deployed on the deepest site, although intermediate logging on the XCB hole was to be considered if the hole reached an adequate depth. Position, depths, and coring totals for each hole are summarized at the beginning of this chapter. All cores are listed in Table 1.

The positioning beacon was deployed at 1208 hr on 10 August, initiating Hole 986A. A standard APC/XCB bottom-hole assembly was made up, but a nonmagnetic drill collar was not required at this site. Hole 986A was spudded and routine piston coring continued through Core 986A-14H, which failed to bleed off pressure, indicating incomplete stroke. Since APC refusal occurred at such a shallow depth, it was decided to continue coring operations in this hole with the XCB system to approximately 200 mbsf if recovery and core quality remained acceptable. XCB coring was initiated with Core 986A-15X. With the exception of two cores of zero and 0.75-m recovery, coring continued with excellent recovery, averaging 81%. Coring was halted after Core 986A-24X, when the scientific target for the hole was reached.

Methane was encountered beginning with Core 986A-2H and continued through Core 24X at 206.0 mbsf. Headspace data for the hole indicated methane ($C_1$) ranging from 955 to 57,852 ppm and ethane ($C_2$) from 2 to 65 ppm. Propane ($C_3$) was detected beginning with Core 12H and ranging from 1 to 7 ppm. The methane/ethane ratios varied from 356 to 11,570. No higher hydrocarbons were detected (see "Organic Geochemistry" section, this chapter).

Hole 986B was spudded 15 m south of Hole 986A. It was suspected that the first core barrel may have impacted a dropstone, affecting the total recovery. If this were true the mudline established from this core would be erroneous, and this was not desirable for a hole with a projected deeper penetration. It was therefore decided that a new hole should be spudded.

The spudding of Hole 986C took place at the same location as Hole 986B (no vessel offset) and the bit was positioned at the same level (2061.0 m) prior to spudding. Routine piston coring continued until Cores 986C-6H through 8H failed to bleed off pressure, indicating incomplete stroke. Three successful Adara temperature measurements were taken on Cores 986C-3H, 5H, and 7H, respectively. These measurements indicated a high temperature gradient of 152°C/km.

XCB coring was initiated with Core 986C-9X and continued until coring was halted after Core 986C-44X, when a core barrel became stuck inside the drill pipe. After several attempts at jarring the barrel loose, the barrel came free. Upon recovery it was found that the XCB cutting shoe thread connection had overtorqued, leading to a swollen box and subsequent mechanical failure. Continued coring with the XCB system was deemed unwise and would risk the opportunity to log the existing hole. Therefore, coring operations were suspended.

Hydrocarbons in small quantities continued to be present through Core 986C-44H at a total depth of 408.0 mbsf. Headspace data for the hole indicated methane ($C_1$) ranging from 3334 to 49,887 ppm and ethane ($C_2$) from 10 to 117 ppm. Propane ($C_3$) ranged from 0 to 16 ppm. The methane/ethane ratios varied from 256 to 1672. No higher hydrocarbons were detected.

As was done on previous holes, two annular-hole volumes of seawater were circulated. A wiper trip with the drill string was then made to 2150.4 m (87.4 mbsf). No overpull was experienced during the wiper trip, but 30,000 lb of drag were noted at 2304 m (241 mbsf) during the trip back to bottom. In addition, 15 m of fill was identified on bottom. The go-devil for locking open the lockable float valve was pumped downhole while another two hole volumes of fluid was pumped. The pipe was then pulled to a logging depth of 102.6 mbsf. No drilling mud was required during the drilling operation and the hole was considered to be in excellent condition. It was therefore considered unnecessary to displace the hole with mud for logging. Three successful logging runs were made on this hole. The Quad combination, FMS, and GHMT/NGT tool strings were deployed to within 21.0, 36.0, and 41.0 m of the bottom of the hole, respectively (see "Wireline Logging" section, this chapter). After the final suite of tools was recovered, the logging sheaves were rigged down, the bit was run to bottom, and the hole was filled with heavy mud.

The vessel was offset 50 m to the south in dynamic positioning mode in preparation for drilling Hole 986D. This was the first hole on Leg 162 in which the RCB coring system was used, which required a

**Table 1. Coring summary for Site 986.**

| Core | Date (Aug. 1995) | Time (UTC) | Depth (mbsf) | Length cored (m) | Length recovered (m) | Recovery (%) |
|---|---|---|---|---|---|---|
| 162-986A- | | | | | | |
| 1H | 10 | 1640 | 0.0–4.6 | 4.6 | 4.59 | 99.8 |
| 2H | 10 | 1705 | 4.6–14.1 | 9.5 | 9.92 | 104.0 |
| 3H | 10 | 1745 | 14.1–23.6 | 9.5 | 9.88 | 104.0 |
| 4H | 10 | 1820 | 23.6–33.1 | 9.5 | 9.86 | 104.0 |
| 5H | 10 | 1845 | 33.1–42.6 | 9.5 | 9.86 | 104.0 |
| 6H | 10 | 1920 | 42.6–52.1 | 9.5 | 10.06 | 105.9 |
| 7H | 10 | 2000 | 52.1–61.6 | 9.5 | 10.68 | 112.4 |
| 8H | 10 | 2035 | 61.6–71.1 | 9.5 | 10.29 | 108.3 |
| 9H | 10 | 2140 | 71.1–78.6 | 7.5 | 7.65 | 102.0 |
| 10H | 10 | 2215 | 78.6–88.1 | 9.5 | 10.51 | 110.6 |
| 11H | 10 | 2240 | 88.1–95.6 | 7.5 | 8.04 | 107.0 |
| 12H | 10 | 2330 | 95.6–101.6 | 6.0 | 7.18 | 119.0 |
| 13H | 10 | 0005 | 101.6–105.6 | 4.0 | 4.03 | 100.0 |
| 14H | 11 | 0050 | 105.6–113.9 | 8.3 | 8.71 | 105.0 |
| 15X | 11 | 0150 | 113.9–119.3 | 5.4 | 5.96 | 110.0 |
| 16X | 11 | 0245 | 119.3–128.9 | 9.6 | 5.69 | 59.3 |
| 17X | 11 | 0350 | 128.9–138.5 | 9.6 | 8.86 | 92.3 |
| 18X | 11 | 0435 | 138.5–148.1 | 9.6 | 0.00 | 0.0 |
| 19X | 11 | 0525 | 148.1–157.8 | 9.7 | 6.92 | 71.3 |
| 20X | 11 | 0610 | 157.8–167.5 | 9.7 | 6.89 | 71.0 |
| 21X | 11 | 0715 | 167.5–177.2 | 9.7 | 9.42 | 97.1 |
| 22X | 11 | 0830 | 177.2–186.8 | 9.6 | 0.75 | 7.8 |
| 23X | 11 | 0945 | 186.8–196.4 | 9.6 | 6.25 | 65.1 |
| 24X | 11 | 1120 | 196.4–206.0 | 9.6 | 9.30 | 96.9 |
| | | | Coring totals: | 206.0 | 181.30 | 88.0 |
| 162-986B- | | | | | | |
| 1H | 11 | 1350 | 0.0–6.0 | 6.0 | 5.95 | 99.1 |
| 2H | 11 | 1420 | 6.0–15.5 | 9.5 | 9.15 | 96.3 |
| | | | Coring totals: | 15.5 | 15.10 | 97.4 |
| 162-986C- | | | | | | |
| 1H | 11 | 1500 | 0.0–7.5 | 7.5 | 7.55 | 100.0 |
| 2H | 11 | 1520 | 7.5–17.0 | 9.5 | 7.31 | 76.9 |
| 3H | 11 | 1610 | 17.0–26.5 | 9.5 | 9.35 | 98.4 |
| 4H | 11 | 1645 | 26.5–36.0 | 9.5 | 9.09 | 95.7 |
| 5H | 11 | 1735 | 36.0–45.5 | 9.5 | 9.28 | 97.7 |
| 6H | 11 | 1810 | 45.5–54.3 | 8.8 | 8.95 | 101.0 |
| 7H | 11 | 1915 | 54.3–62.3 | 8.0 | 8.09 | 101.0 |
| 8H | 11 | 1950 | 62.3–71.8 | 9.5 | 9.96 | 105.0 |
| 9X | 11 | 2030 | 71.8–80.6 | 8.8 | 0.00 | 0.0 |
| 10X | 11 | 2115 | 80.6–90.2 | 9.6 | 7.91 | 82.4 |
| 11X | 11 | 2155 | 90.2–99.8 | 9.6 | 7.90 | 82.3 |
| 12X | 11 | 2250 | 99.8–109.5 | 9.7 | 3.77 | 38.8 |
| 13X | 11 | 2335 | 109.5–119.2 | 9.7 | 6.35 | 65.4 |
| 14X | 12 | 0025 | 119.2–128.8 | 9.6 | 9.61 | 100.0 |
| 15X | 12 | 0120 | 128.8–138.5 | 9.7 | 7.04 | 72.6 |
| 16X | 12 | 0215 | 138.5–148.1 | 9.6 | 8.54 | 88.9 |
| 17X | 12 | 0315 | 148.1–157.8 | 9.7 | 8.69 | 89.6 |
| 18X | 12 | 0430 | 157.8–167.4 | 9.6 | 0.22 | 2.3 |
| 19X | 12 | 0530 | 167.4–177.1 | 9.7 | 2.99 | 30.8 |
| 20X | 12 | 0630 | 177.1–186.7 | 9.6 | 2.59 | 27.0 |
| 21X | 12 | 0740 | 186.7–196.3 | 9.6 | 6.76 | 70.4 |
| 22X | 12 | 0845 | 196.3–205.9 | 9.6 | 5.02 | 52.3 |
| 23X | 12 | 1020 | 205.9–215.5 | 9.6 | 0.50 | 5.2 |
| 24X | 12 | 1205 | 215.5–225.1 | 9.6 | 0.93 | 9.7 |
| 25X | 12 | 1310 | 225.1–234.7 | 9.6 | 0.00 | 0.0 |
| 26X | 12 | 1400 | 234.7–244.3 | 9.6 | 0.84 | 8.8 |
| 27X | 12 | 1440 | 244.3–254.0 | 9.7 | 1.53 | 15.8 |
| 28X | 12 | 1520 | 254.0–259.0 | 5.0 | 2.47 | 49.4 |
| 29X | 12 | 1605 | 259.0–263.6 | 4.6 | 6.11 | 133.0 |
| 30X | 12 | 1720 | 263.6–273.2 | 9.6 | 4.64 | 48.3 |
| 31X | 12 | 1855 | 273.2–282.8 | 9.6 | 7.23 | 75.3 |
| 32X | 12 | 1950 | 282.8–292.4 | 9.6 | 0.03 | 0.3 |
| 33X | 12 | 2030 | 292.4–302.1 | 9.7 | 0.09 | 0.9 |
| 34X | 12 | 2130 | 302.1–311.7 | 9.6 | 2.48 | 25.8 |
| 35X | 12 | 2220 | 311.7–321.3 | 9.6 | 2.63 | 27.4 |
| 36X | 12 | 2320 | 321.3–330.9 | 9.6 | 0.99 | 10.3 |
| 37X | 13 | 0100 | 330.9–340.6 | 9.7 | 10.02 | 103.3 |
| 38X | 13 | 0255 | 340.6–350.2 | 9.6 | 5.19 | 54.0 |
| 39X | 13 | 0430 | 350.2–359.8 | 9.6 | 7.43 | 77.4 |
| 40X | 13 | 0605 | 359.8–369.4 | 9.6 | 7.42 | 77.3 |
| 41X | 13 | 0730 | 369.4–379.1 | 9.7 | 6.89 | 71.0 |
| 42X | 13 | 0905 | 379.1–388.7 | 9.6 | 6.05 | 63.0 |
| 43X | 13 | 1055 | 388.7–398.3 | 9.6 | 4.73 | 49.3 |
| 44X | 13 | 1515 | 398.3–408.0 | 9.7 | 4.61 | 47.5 |
| | | | Coring totals: | 408.0 | 229.80 | 56.3 |
| 162-986D- | | | | | | |
| 1R | 15 | 1420 | 387.8–397.4 | 9.6 | 0.05 | 0.5 |
| 2R | 15 | 1555 | 397.4–407.1 | 9.7 | 5.58 | 57.5 |
| 3R | 15 | 1705 | 407.1–416.7 | 9.6 | 0.88 | 9.2 |
| 4R | 15 | 1820 | 416.7–426.3 | 9.6 | 0.00 | 0.0 |
| 5R | 15 | 2015 | 426.3–435.9 | 9.6 | 0.20 | 2.1 |
| 6R | 15 | 2130 | 435.9–445.5 | 9.6 | 1.68 | 17.5 |
| 7R | 15 | 2240 | 445.5–455.1 | 9.6 | 0.04 | 0.4 |
| 8R | 15 | 2350 | 455.1–464.7 | 9.6 | 1.95 | 20.3 |
| 9R | 16 | 0110 | 464.7–474.3 | 9.6 | 0.42 | 4.4 |
| 10R | 16 | 0225 | 474.3–483.9 | 9.6 | 0.10 | 1.0 |
| 11R | 16 | 0350 | 483.9–493.5 | 9.6 | 0.41 | 4.3 |
| 12R | 16 | 0515 | 493.5–503.1 | 9.6 | 0.00 | 0.0 |
| 13R | 16 | 0635 | 503.1–512.7 | 9.6 | 0.00 | 0.0 |
| 14R | 16 | 0805 | 512.7–522.3 | 9.6 | 5.92 | 61.6 |
| 15R | 16 | 0945 | 522.3–531.9 | 9.6 | 9.44 | 98.3 |
| 16R | 16 | 1055 | 531.9–541.5 | 9.6 | 9.61 | 100.0 |
| 17R | 16 | 1205 | 541.5–551.1 | 9.6 | 5.10 | 53.1 |
| 18R | 16 | 1315 | 551.1–560.7 | 9.6 | 7.85 | 81.8 |
| 19R | 16 | 1410 | 560.7–570.3 | 9.6 | 4.18 | 43.5 |
| 20R | 16 | 1505 | 570.3–580.0 | 9.7 | 0.00 | 0.0 |
| 21R | 16 | 1605 | 580.0–589.6 | 9.6 | 4.68 | 48.7 |
| 22R | 16 | 1720 | 589.6–599.2 | 9.6 | 0.00 | 0.0 |
| 23R | 16 | 1830 | 599.2–608.8 | 9.6 | 0.00 | 0.0 |
| 24R | 16 | 1930 | 608.8–618.4 | 9.6 | 0.00 | 0.0 |
| 25R | 16 | 2120 | 618.4–628.1 | 9.7 | 0.00 | 0.0 |
| 26R | 16 | 2225 | 628.1–637.7 | 9.6 | 0.00 | 0.0 |
| 27R | 16 | 2330 | 637.7–647.4 | 9.7 | 0.33 | 3.4 |
| 28R | 17 | 0100 | 647.4–656.9 | 9.5 | 8.44 | 88.8 |
| 29R | 17 | 0225 | 656.9–666.6 | 9.7 | 5.71 | 58.8 |
| 30R | 17 | 0400 | 666.6–676.2 | 9.6 | 5.65 | 58.8 |
| 31R | 17 | 0510 | 676.2–685.8 | 9.6 | 6.58 | 68.5 |
| 32R | 17 | 0615 | 685.8–695.4 | 9.6 | 8.40 | 87.5 |
| 33R | 17 | 0735 | 695.4–705.0 | 9.6 | 1.48 | 15.4 |
| 34R | 17 | 0915 | 705.0–714.6 | 9.6 | 2.32 | 24.1 |
| 35R | 17 | 1045 | 714.6–724.2 | 9.6 | 9.81 | 102.0 |
| 36R | 17 | 1205 | 724.2–733.8 | 9.6 | 0.01 | 0.1 |
| 37R | 17 | 1310 | 733.8–743.4 | 9.6 | 9.54 | 99.4 |
| 38R | 17 | 1415 | 743.4–753.0 | 9.6 | 6.48 | 67.5 |
| 39R | 17 | 1525 | 753.0–762.6 | 9.6 | 8.94 | 93.1 |
| 40R | 17 | 1635 | 762.6–772.2 | 9.6 | 8.91 | 92.8 |
| 41R | 17 | 1755 | 772.2–781.8 | 9.6 | 7.62 | 79.4 |
| 42R | 17 | 1900 | 781.8–791.4 | 9.6 | 9.06 | 94.4 |
| 43R | 17 | 2015 | 791.4–801.1 | 9.7 | 3.92 | 40.4 |
| 44R | 17 | 2140 | 801.1–810.7 | 9.6 | 5.78 | 60.2 |
| 45R | 17 | 2305 | 810.7–820.3 | 9.6 | 9.74 | 101.0 |
| 46R | 18 | 0035 | 820.3–829.9 | 9.6 | 5.46 | 56.9 |
| 47R | 18 | 0210 | 829.9–839.5 | 9.6 | 3.63 | 37.8 |
| 48R | 18 | 0330 | 839.5–849.2 | 9.7 | 2.72 | 28.0 |
| 49R | 18 | 0440 | 849.2–858.8 | 9.6 | 1.74 | 18.1 |
| 50R | 18 | 0605 | 858.8–868.4 | 9.6 | 7.15 | 74.5 |
| 51R | 18 | 0730 | 868.4–878.1 | 9.7 | 9.60 | 98.9 |
| 52R | 18 | 0925 | 878.1–887.6 | 9.5 | 9.67 | 102.0 |
| 53R | 18 | 1055 | 887.6–897.3 | 9.7 | 9.39 | 96.8 |
| 54R | 18 | 1230 | 897.3–906.9 | 9.6 | 1.04 | 10.8 |
| 55R | 18 | 1430 | 906.9–916.5 | 9.6 | 2.85 | 29.7 |
| 56R | 18 | 1725 | 916.5–926.1 | 9.6 | 0.00 | 0.0 |
| 57R | 18 | 2305 | 926.1–935.7 | 9.6 | 2.85 | 29.7 |
| 58R | 19 | 0200 | 935.7–945.3 | 9.6 | 1.91 | 19.9 |
| 59R | 19 | 0350 | 945.3–955.0 | 9.7 | 5.00 | 51.5 |
| 60R | 19 | 0530 | 955.0–964.6 | 9.6 | 1.73 | 18.0 |
| | | | Coring totals: | 576.8 | 241.60 | 41.9 |

change in the bottom-hole assembly (BHA) and the type of rotary core bit used. The new BHA was tripped back to bottom and Hole 986D was spudded at 0137 hr on 15 August. Since the upper several hundred meters of formation was to be drilled rather than cored, the seafloor depth from Hole 986C of 2063.0 m was used. This was more accurate than that which would have been obtained by the driller "feeling" for bottom with the RCB drilling assembly.

Drilling ahead with a center bit in place continued to a depth of 2450.8 m, or 387.8 mbsf. The center bit was recovered via wireline, and hole deviation measurements were taken on bottom and at 100-m increments on the way out of the hole. A hole deviation of approximately 3.6° was determined based on the measurements.

Continuous RCB coring commenced with Core 986-1R and continued with highly variable recovery, ranging from 100% to as low as zero. Beginning with Core 986D-22R a string of five straight empty core barrels was retrieved through an apparent coarse-grained sandy debris-flow zone. Flows of this nature were not unexpected in this geological environment. Core 986D-27R recovered a mere 0.33 m, and then core recovery improved significantly. With the exception of two zero-recovery cores, all remaining cores recovered between 11% and 102% (Table 1).

Coring was terminated after Core 986D-60R at a depth of 3027.6 m (964.6 mbsf). The termination depth was in excess of the original scientific target depth of 900 mbsf, but did not reach the desired 1000 mbsf. Coring was halted because several low-recovery cores were recovered and bit plugging occurred on three successive core barrels. In addition, due primarily to the bit plugging problems, the rate of forward progress had decreased substantially. Several deployments of the bit deplugger were made during the coring process when dropstones were suspected of plugging the bit throat. One final run with the bit deplugger was made after recovering Core 986D-60R and pump pressures were once again restored to normal.

Hydrocarbons in small quantities were present throughout the drilling of the hole just as in the other holes drilled at this site. Headspace data were monitored closely throughout the drilling process (see "Organic Geochemistry" section, this chapter).

Upon completion of the coring program the hole was swept with two mud sweeps of 60 barrels each. A wiper trip with the drill string was then made to 2163.0 m (100.0 mbsf). While running back in the hole a hard bridge (45,000 lb of bit weight) was tagged at a depth of 2557.0 m (494.0 mbsf). The top drive was picked up and a center bit was dropped at that point. The hole continued to give problems from that point on and required a total of 6.5 hr of reaming to get back to the original hole total depth. Several additional gel mud sweeps were pumped during the reaming operation.

After again sweeping the hole with two gel mud pills, the center bit was recovered and two additional wireline runs were made to release the bit and reverse-shift the mechanical-bit-release sleeve back down again. Because of the difficulty in reaching bottom with the top drive and a working drill bit, it was considered unlikely that the feat could be duplicated upon completion of logging with open-ended pipe. The hole was therefore displaced with heavy mud to avoid the need to get back to bottom and to enhance the chances of conducting a logging program in the quickly deteriorating hole.

After filling the hole with mud the pipe was tripped to a logging depth of 2385.7 m (322.7 mbsf). A maximum of 15,000 lb of overpull was experienced throughout the trip. The logging equipment was rigged and the first run, with the Quad combo suite of tools, was deployed to a depth of 2468.0 m (405.0 mbsf). This was only 82.3 m below the open-ended pipe. The logging tools were removed and the pipe was lowered to a depth of 2501.1 m (438.1 mbsf). A second run with the Quad combo tools reached an initial depth of 2514 m and was eventually worked to a depth of 2550 m (487.0 mbsf), or 48.9 m below open-ended pipe. Further logging attempts were considered futile and subsequent logging was abandoned. The tools were recovered, the logging sheaves rigged down, and the pipe tripped back to the surface. The beacon was recovered while a BHA inspection was taking place and the ship departed the site at 2100 hr on 20 August 1995.

## COMPOSITE DEPTHS

The sediments drilled at Site 986 were marked by numerous intervals of gas expansion, dropstones, disturbance, and nonrecovery (see "Lithostratigraphy" section, this chapter). However, relative continuity of the sedimentary sequence was documented for approximately the upper 200 mbsf of the drilled section. Sufficient overlap between the first six cores drilled in Holes 986A, 986B, and 986C allowed both a composite section and a splice to be developed over this interval, as described in the "Composite Depths" section, "Explanatory Notes" chapter (this volume). The depth offsets that comprise the composite depth section at Site 986 are given in Table 2.

Multisensor-track data used in the correlations are displayed on the composite depth scale in Figure 4. Magnetic susceptibility was the primary parameter used to develop the composite section. Gamma-ray attenuation porosity (GRAPE) density was used to confirm the hole-to-hole correlations. Due to numerous disturbed intervals, however, these data were not always reliable and exact measurement values should be viewed with caution.

Although a composite section was developed for the upper 210 mcd of Site 986, providing relative alignments between adjacent holes, confirmed overlap was maintained only through the top 60 mcd. Because of the pervasive disturbance and expansion, it was not possible to align every sedimentary feature using only the composite depth scale adjustments.

From the Site 986 composite depth section, a single spliced record was developed, as described in the "Explanatory Notes" section (this volume). The tie points between the cores used to construct the splice are given in Table 3. It was not possible to omit disturbed and anomalous intervals from the splice, as most cores showed some evidence of disturbance. Below the base of the composite section at 220 mcd, the remainder of the Hole 986C and 986D cores were appended to the composite with no adjustment of their relative depths. The spliced GRAPE density, natural gamma radiation, and magnetic susceptibility data are shown in Figure 5.

## LITHOSTRATIGRAPHY

Four holes were drilled at Site 986, with a maximum penetration of 964.6 mbsf. The sediments recovered are predominantly fine- to medium-grained siliciclastics with varying amounts of gravel. The dominant lithologies include silty clays, clays with silt, clayey silts with sand, and silty clays with sand. Dropstones (>1.0 cm in size) are abundant in most cores of the upper sedimentary sequence (0–561.8 mbsf). Sedimentary rocks are common throughout this sequence, whereas igneous and/or metamorphic rock fragments are more common in the interval from 380 to 550 mbsf. In all, over 500 dropstones greater than 1.0 cm in size were recovered at Site 986. Biocarbonates in amounts >10% are restricted to the upper 98.0 m of the sedimentary sequence and to the interval between 687 and 746 mbsf and mostly occur as clayey silt with nannofossils. Biosilica is encountered only in trace amounts.

Authigenic iron sulfides, primarily in the form of disseminated pyrite, are commonly present in minor amounts. Disseminated volcanic ash is also present throughout, while discrete ash layers were not observed. Laminated beds dipping at varying angles (5°–70°) and contorted beds are common features toward the base of the sedimentary sequence.

The lithostratigraphic units and subunits at Site 986 are defined on the basis of data obtained from seven sources: (1) visual core descriptions, (2) smear slide examination, (3) bulk calcium carbonate measurements, (4) spectral reflectance measurements, (5) magnetic susceptibility measurements, (6) natural gamma-ray measurements, and (7) X-ray diffraction (XRD) analysis of bulk sediments. However, multisensor track (MST) and spectral reflectance measurements are only of limited use at this site because of coring disturbance created in XCB and RCB cores and generally poor recovery. To create a continuous record of the uppermost sediment sequence, MST results are combined with wireline logging results from Hole 986C (see "Wireline Logging" section, this chapter). Despite these limitations, four lithostratigraphic units are defined. Lithostratigraphic unit boundaries occur at 98.0, 561.8, and 820.3 mbsf. A subunit boundary within Unit IV occurs at 897.3 mbsf. All unit and subunit boundary depths are given for Holes 986C and 986D. The lithologic descriptions of these units follow and a summary of each lithostratigraphic unit is presented in Table 4.

**Table 2. Site 986 composite depths.**

| Core, section | Length (cm) | Depth (mbsf) | Depth (mcd) | Offset (mcd – mbsf) |
|---|---|---|---|---|
| 162-986A- | | | | |
| 1H-1 | 150 | 0.00 | 0.00 | 0.00 |
| 1H-2 | 150 | 1.50 | 1.50 | 0.00 |
| 1H-3 | 150 | 3.00 | 3.00 | 0.00 |
| 1H-CC | 9 | 4.50 | 4.50 | 0.00 |
| 2H-1 | 150 | 4.60 | 5.96 | 1.36 |
| 2H-2 | 150 | 6.10 | 7.46 | 1.36 |
| 2H-3 | 150 | 7.60 | 8.96 | 1.36 |
| 2H-4 | 150 | 9.10 | 10.46 | 1.36 |
| 2H-5 | 150 | 10.60 | 11.96 | 1.36 |
| 2H-6 | 150 | 12.10 | 13.46 | 1.36 |
| 2H-7 | 68 | 13.60 | 14.96 | 1.36 |
| 2H-CC | 24 | 14.28 | 15.64 | 1.36 |
| 3H-1 | 150 | 14.10 | 16.16 | 2.06 |
| 3H-2 | 150 | 15.60 | 17.66 | 2.06 |
| 3H-3 | 150 | 17.10 | 19.16 | 2.06 |
| 3H-4 | 150 | 18.60 | 20.66 | 2.06 |
| 3H-5 | 150 | 20.10 | 22.16 | 2.06 |
| 3H-6 | 150 | 21.60 | 23.66 | 2.06 |
| 3H-7 | 66 | 23.10 | 25.16 | 2.06 |
| 3H-CC | 22 | 23.76 | 25.82 | 2.06 |
| 4H-1 | 150 | 23.60 | 26.54 | 2.94 |
| 4H-2 | 150 | 25.10 | 28.04 | 2.94 |
| 4H-3 | 150 | 26.60 | 29.54 | 2.94 |
| 4H-4 | 150 | 28.10 | 31.04 | 2.94 |
| 4H-5 | 150 | 29.60 | 32.54 | 2.94 |
| 4H-6 | 150 | 31.10 | 34.04 | 2.94 |
| 4H-7 | 56 | 32.60 | 35.54 | 2.94 |
| 4H-CC | 30 | 33.16 | 36.10 | 2.94 |
| 5H-1 | 150 | 33.10 | 36.36 | 3.26 |
| 5H-2 | 150 | 34.60 | 37.86 | 3.26 |
| 5H-3 | 150 | 36.10 | 39.36 | 3.26 |
| 5H-4 | 150 | 37.60 | 40.86 | 3.26 |
| 5H-5 | 150 | 39.10 | 42.36 | 3.26 |
| 5H-6 | 150 | 40.60 | 43.86 | 3.26 |
| 5H-7 | 59 | 42.10 | 45.36 | 3.26 |
| 5H-CC | 27 | 42.69 | 45.95 | 3.26 |
| 6H-1 | 150 | 42.60 | 46.40 | 3.80 |
| 6H-2 | 150 | 44.10 | 47.90 | 3.80 |
| 6H-3 | 150 | 45.60 | 49.40 | 3.80 |
| 6H-4 | 140 | 47.10 | 50.90 | 3.80 |
| 6H-5 | 133 | 48.50 | 52.30 | 3.80 |
| 6H-6 | 150 | 49.83 | 53.63 | 3.80 |
| 6H-7 | 117 | 51.33 | 55.13 | 3.80 |
| 6H-CC | 29 | 52.50 | 56.30 | 3.80 |
| 7H-1 | 56 | 52.10 | 51.50 | –0.60 |
| 7H-2 | 150 | 52.66 | 52.06 | –0.60 |
| 7H-3 | 150 | 54.16 | 53.56 | –0.60 |
| 7H-4 | 150 | 55.66 | 55.06 | –0.60 |
| 7H-5 | 150 | 57.16 | 56.56 | –0.60 |
| 7H-6 | 150 | 58.66 | 58.06 | –0.60 |
| 7H-7 | 150 | 60.16 | 59.56 | –0.60 |
| 7H-8 | 88 | 61.66 | 61.06 | –0.60 |
| 7H-CC | 24 | 62.54 | 61.94 | –0.60 |
| 8H-1 | 145 | 61.60 | 61.00 | –0.60 |
| 8H-2 | 150 | 63.05 | 62.45 | –0.60 |
| 8H-3 | 150 | 64.55 | 63.95 | –0.60 |
| 8H-4 | 150 | 66.05 | 65.45 | –0.60 |
| 8H-5 | 150 | 67.55 | 66.95 | –0.60 |
| 8H-6 | 150 | 69.05 | 68.45 | –0.60 |
| 8H-7 | 86 | 70.55 | 69.95 | –0.60 |
| 8H-CC | 48 | 71.41 | 70.81 | –0.60 |
| 9H-1 | 150 | 71.10 | 70.50 | –0.60 |
| 9H-2 | 150 | 72.60 | 72.00 | –0.60 |
| 9H-3 | 150 | 74.10 | 73.50 | –0.60 |
| 9H-4 | 150 | 75.60 | 75.00 | –0.60 |
| 9H-5 | 128 | 77.10 | 76.50 | –0.60 |
| 9H-CC | 37 | 78.38 | 77.78 | –0.60 |
| 10H-1 | 149 | 78.60 | 78.00 | –0.60 |
| 10H-2 | 150 | 80.09 | 79.49 | –0.60 |
| 10H-3 | 150 | 81.59 | 80.99 | –0.60 |
| 10H-4 | 150 | 83.09 | 82.49 | –0.60 |
| 10H-5 | 150 | 84.59 | 83.99 | –0.60 |
| 10H-6 | 150 | 86.09 | 85.49 | –0.60 |
| 10H-7 | 110 | 87.59 | 86.99 | –0.60 |
| 10H-CC | 48 | 88.69 | 88.09 | –0.60 |
| 11H-1 | 150 | 88.10 | 87.50 | –0.60 |
| 11H-2 | 150 | 89.60 | 89.00 | –0.60 |
| 11H-3 | 150 | 91.10 | 90.50 | –0.60 |
| 11H-4 | 150 | 92.60 | 92.00 | –0.60 |
| 11H-5 | 141 | 94.10 | 93.50 | –0.60 |
| 11H-CC | 63 | 95.51 | 94.91 | –0.60 |
| 12H-1 | 150 | 95.60 | 98.04 | 2.44 |
| 12H-2 | 150 | 97.10 | 99.54 | 2.44 |
| 12H-3 | 150 | 98.60 | 101.04 | 2.44 |
| 12H-4 | 150 | 100.10 | 102.54 | 2.44 |
| 12H-5 | 93 | 101.60 | 104.04 | 2.44 |
| 12H-CC | 25 | 102.53 | 104.97 | 2.44 |
| 13H-1 | 150 | 101.60 | 106.24 | 4.64 |
| 13H-2 | 150 | 103.10 | 107.74 | 4.64 |
| 13H-3 | 69 | 104.60 | 109.24 | 4.64 |
| 13H-CC | 34 | 105.29 | 109.93 | 4.64 |
| 14H-1 | 150 | 105.60 | 110.24 | 4.64 |
| 14H-2 | 150 | 107.10 | 111.74 | 4.64 |
| 14H-3 | 150 | 108.60 | 113.24 | 4.64 |
| 14H-4 | 150 | 110.10 | 114.74 | 4.64 |
| 14H-5 | 150 | 111.60 | 116.24 | 4.64 |
| 14H-6 | 98 | 113.10 | 117.74 | 4.64 |
| 14H-CC | 26 | 114.08 | 118.72 | 4.64 |
| 15X-1 | 150 | 113.90 | 119.90 | 6.00 |
| 15X-2 | 150 | 115.40 | 121.40 | 6.00 |
| 15X-3 | 150 | 116.90 | 122.90 | 6.00 |
| 15X-4 | 126 | 118.40 | 124.40 | 6.00 |
| 15X-CC | 20 | 119.66 | 125.66 | 6.00 |
| 16X-1 | 150 | 119.30 | 126.03 | 6.73 |
| 16X-2 | 150 | 120.80 | 127.53 | 6.73 |
| 16X-3 | 150 | 122.30 | 129.03 | 6.73 |
| 16X-4 | 90 | 123.80 | 130.53 | 6.73 |
| 16X-CC | 29 | 124.70 | 131.43 | 6.73 |
| 17X-1 | 150 | 128.90 | 135.90 | 7.00 |
| 17X-2 | 150 | 130.40 | 137.40 | 7.00 |
| 17X-3 | 150 | 131.90 | 138.90 | 7.00 |
| 17X-4 | 150 | 133.40 | 140.40 | 7.00 |
| 17X-5 | 150 | 134.90 | 141.90 | 7.00 |
| 17X-6 | 74 | 136.40 | 143.40 | 7.00 |
| 17X-CC | 62 | 137.14 | 144.14 | 7.00 |
| 19X-1 | 150 | 148.10 | 155.34 | 7.24 |
| 19X-2 | 150 | 149.60 | 156.84 | 7.24 |
| 19X-3 | 150 | 151.10 | 158.34 | 7.24 |
| 19X-4 | 150 | 152.60 | 159.84 | 7.24 |
| 19X-5 | 71 | 154.10 | 161.34 | 7.24 |
| 19X-CC | 24 | 154.81 | 162.05 | 7.24 |
| 20X-1 | 150 | 157.80 | 165.04 | 7.24 |
| 20X-2 | 150 | 159.30 | 166.54 | 7.24 |
| 20X-3 | 150 | 160.80 | 168.04 | 7.24 |
| 20X-4 | 150 | 162.30 | 169.54 | 7.24 |
| 20X-5 | 64 | 163.80 | 171.04 | 7.24 |
| 20X-CC | 25 | 164.44 | 171.68 | 7.24 |
| 21X-1 | 90 | 167.50 | 174.74 | 7.24 |
| 21X-2 | 62 | 168.40 | 175.64 | 7.24 |
| 21X-3 | 150 | 169.02 | 176.26 | 7.24 |
| 21X-4 | 150 | 170.52 | 177.76 | 7.24 |
| 21X-5 | 150 | 172.02 | 179.26 | 7.24 |
| 21X-6 | 150 | 173.52 | 180.76 | 7.24 |
| 21X-7 | 150 | 175.02 | 182.26 | 7.24 |
| 21X-CC | 40 | 176.52 | 183.76 | 7.24 |
| 22X-1 | 75 | 177.20 | 184.44 | 7.24 |
| 23X-1 | 150 | 186.80 | 190.83 | 4.03 |
| 23X-2 | 150 | 188.30 | 192.33 | 4.03 |
| 23X-3 | 150 | 189.80 | 193.83 | 4.03 |
| 23X-4 | 137 | 191.30 | 195.33 | 4.03 |
| 23X-CC | 38 | 192.67 | 196.70 | 4.03 |
| 24X-1 | 150 | 196.40 | 200.43 | 4.03 |
| 24X-2 | 150 | 197.90 | 201.93 | 4.03 |
| 24X-3 | 150 | 199.40 | 203.43 | 4.03 |
| 24X-4 | 150 | 200.90 | 204.93 | 4.03 |
| 24X-5 | 150 | 202.40 | 206.43 | 4.03 |
| 24X-6 | 67 | 203.90 | 207.93 | 4.03 |
| 24X-7 | 82 | 204.57 | 208.60 | 4.03 |
| 24X-CC | 31 | 205.39 | 209.42 | 4.03 |
| 162-986B- | | | | |
| 1H-1 | 150 | 0.00 | 0.12 | 0.12 |
| 1H-2 | 150 | 1.50 | 1.62 | 0.12 |
| 1H-3 | 150 | 3.00 | 3.12 | 0.12 |
| 1H-4 | 111 | 4.50 | 4.62 | 0.12 |
| 1H-CC | 34 | 5.61 | 5.73 | 0.12 |
| 2H-1 | 150 | 6.00 | 8.65 | 2.65 |
| 2H-2 | 150 | 7.50 | 10.15 | 2.65 |
| 2H-3 | 150 | 9.00 | 11.65 | 2.65 |
| 2H-4 | 150 | 10.50 | 13.15 | 2.65 |
| 2H-5 | 150 | 12.00 | 14.65 | 2.65 |
| 2H-6 | 129 | 13.50 | 16.15 | 2.65 |
| 2H-CC | 36 | 14.79 | 17.44 | 2.65 |
| 162-986C- | | | | |
| 1H-1 | 150 | 0.00 | 0.11 | 0.11 |
| 1H-2 | 150 | 1.50 | 1.61 | 0.11 |
| 1H-3 | 150 | 3.00 | 3.11 | 0.11 |
| 1H-4 | 150 | 4.50 | 4.61 | 0.11 |
| 1H-5 | 137 | 6.00 | 6.11 | 0.11 |
| 1H-CC | 18 | 7.37 | 7.48 | 0.11 |
| 2H-1 | 150 | 7.50 | 8.35 | 0.85 |
| 2H-2 | 150 | 9.00 | 9.85 | 0.85 |
| 2H-3 | 150 | 10.50 | 11.35 | 0.85 |
| 2H-4 | 150 | 12.00 | 12.85 | 0.85 |
| 2H-5 | 105 | 13.50 | 14.35 | 0.85 |
| 2H-CC | 26 | 14.55 | 15.40 | 0.85 |
| 3H-1 | 150 | 17.00 | 18.95 | 1.95 |

**Table 2 (continued).**

| Core, section | Length (cm) | Depth (mbsf) | Depth (mcd) | Offset (mcd – mbsf) |
|---|---|---|---|---|
| 3H-2 | 150 | 18.50 | 20.45 | 1.95 |
| 3H-3 | 150 | 20.00 | 21.95 | 1.95 |
| 3H-4 | 150 | 21.50 | 23.45 | 1.95 |
| 3H-5 | 150 | 23.00 | 24.95 | 1.95 |
| 3H-6 | 128 | 24.50 | 26.45 | 1.95 |
| 3H-CC | 57 | 25.78 | 27.73 | 1.95 |
| 4H-1 | 150 | 26.50 | 29.30 | 2.80 |
| 4H-2 | 150 | 28.00 | 30.80 | 2.80 |
| 4H-3 | 150 | 29.50 | 32.30 | 2.80 |
| 4H-4 | 150 | 31.00 | 33.80 | 2.80 |
| 4H-5 | 150 | 32.50 | 35.30 | 2.80 |
| 4H-6 | 132 | 34.00 | 36.80 | 2.80 |
| 4H-CC | 27 | 35.32 | 38.12 | 2.80 |
| 5H-1 | 130 | 36.00 | 39.61 | 3.61 |
| 5H-2 | 38 | 37.30 | 40.91 | 3.61 |
| 5H-3 | 150 | 37.68 | 41.29 | 3.61 |
| 5H-4 | 150 | 39.18 | 42.79 | 3.61 |
| 5H-5 | 150 | 40.68 | 44.29 | 3.61 |
| 5H-6 | 150 | 42.18 | 45.79 | 3.61 |
| 5H-7 | 150 | 43.68 | 47.29 | 3.61 |
| 5H-CC | 10 | 45.18 | 48.79 | 3.61 |
| 6H-1 | 150 | 45.50 | 50.53 | 5.03 |
| 6H-2 | 150 | 47.00 | 52.03 | 5.03 |
| 6H-3 | 150 | 48.50 | 53.53 | 5.03 |
| 6H-4 | 150 | 50.00 | 55.03 | 5.03 |
| 6H-5 | 150 | 51.50 | 56.53 | 5.03 |
| 6H-6 | 140 | 53.00 | 58.03 | 5.03 |
| 6H-CC | 15 | 54.40 | 59.43 | 5.03 |
| 7H-1 | 150 | 54.30 | 59.33 | 5.03 |
| 7H-2 | 150 | 55.80 | 60.83 | 5.03 |
| 7H-3 | 150 | 57.30 | 62.33 | 5.03 |
| 7H-4 | 150 | 58.80 | 63.83 | 5.03 |
| 7H-5 | 150 | 60.30 | 65.33 | 5.03 |
| 7H-CC | 59 | 61.80 | 66.83 | 5.03 |
| 8H-1 | 150 | 62.30 | 67.69 | 5.39 |
| 8H-2 | 150 | 63.80 | 69.19 | 5.39 |
| 8H-3 | 104 | 65.30 | 70.69 | 5.39 |
| 8H-4 | 63 | 66.34 | 71.73 | 5.39 |
| 8H-5 | 98 | 66.97 | 72.36 | 5.39 |
| 8H-6 | 150 | 67.95 | 73.34 | 5.39 |
| 8H-7 | 80 | 69.45 | 74.84 | 5.39 |
| 8H-CC | 16 | 70.25 | 75.64 | 5.39 |
| 10X-1 | 150 | 80.60 | 82.07 | 1.47 |
| 10X-2 | 150 | 82.10 | 83.57 | 1.47 |
| 10X-3 | 150 | 83.60 | 85.07 | 1.47 |
| 10X-4 | 150 | 85.10 | 86.57 | 1.47 |
| 10X-5 | 150 | 86.60 | 88.07 | 1.47 |
| 10X-6 | 21 | 88.10 | 89.57 | 1.47 |
| 10X-CC | 20 | 88.31 | 89.78 | 1.47 |
| 11X-1 | 150 | 90.20 | 91.67 | 1.47 |
| 11X-2 | 150 | 91.70 | 93.17 | 1.47 |
| 11X-3 | 150 | 93.20 | 94.67 | 1.47 |
| 11X-4 | 150 | 94.70 | 96.17 | 1.47 |
| 11X-5 | 150 | 96.20 | 97.67 | 1.47 |
| 11X-CC | 40 | 97.70 | 99.17 | 1.47 |
| 12X-1 | 150 | 99.80 | 104.81 | 5.01 |
| 12X-2 | 98 | 101.30 | 106.31 | 5.01 |
| 12X-3 | 111 | 102.28 | 107.29 | 5.01 |
| 12X-CC | 18 | 103.39 | 108.40 | 5.01 |
| 13X-1 | 150 | 109.50 | 115.13 | 5.63 |
| 13X-2 | 150 | 111.00 | 116.63 | 5.63 |
| 13X-3 | 150 | 112.50 | 118.13 | 5.63 |
| 13X-4 | 147 | 114.00 | 119.63 | 5.63 |
| 13X-CC | 38 | 115.47 | 121.10 | 5.63 |
| 14X-1 | 74 | 119.20 | 124.86 | 5.66 |
| 14X-2 | 150 | 119.94 | 125.60 | 5.66 |
| 14X-3 | 150 | 121.44 | 127.10 | 5.66 |
| 14X-4 | 150 | 122.94 | 128.60 | 5.66 |
| 14X-5 | 150 | 124.44 | 130.10 | 5.66 |
| 14X-6 | 126 | 125.94 | 131.60 | 5.66 |
| 14X-7 | 104 | 127.20 | 132.86 | 5.66 |
| 14X-CC | 57 | 128.24 | 133.90 | 5.66 |
| 15X-1 | 99 | 128.80 | 134.46 | 5.66 |
| 15X-2 | 150 | 129.79 | 135.45 | 5.66 |
| 15X-3 | 150 | 131.29 | 136.95 | 5.66 |
| 15X-4 | 150 | 132.79 | 138.45 | 5.66 |
| 15X-5 | 105 | 134.29 | 139.95 | 5.66 |
| 15X-CC | 50 | 135.34 | 141.00 | 5.66 |
| 16X-1 | 115 | 138.50 | 142.86 | 4.36 |
| 16X-2 | 150 | 139.65 | 144.01 | 4.36 |
| 16X-3 | 150 | 141.15 | 145.51 | 4.36 |
| 16X-4 | 150 | 142.65 | 147.01 | 4.36 |
| 16X-5 | 150 | 144.15 | 148.51 | 4.36 |
| 16X-6 | 102 | 145.65 | 150.01 | 4.36 |
| 16X-CC | 37 | 146.67 | 151.03 | 4.36 |
| 17X-1 | 150 | 148.10 | 152.46 | 4.36 |
| 17X-2 | 150 | 149.60 | 153.96 | 4.36 |
| 17X-3 | 150 | 151.10 | 155.46 | 4.36 |
| 17X-4 | 150 | 152.60 | 156.96 | 4.36 |
| 17X-5 | 134 | 154.10 | 158.46 | 4.36 |
| 17X-6 | 100 | 155.44 | 159.80 | 4.36 |
| 17X-CC | 26 | 156.44 | 160.80 | 4.36 |
| 18X-CC | 22 | 157.80 | 162.16 | 4.36 |
| 19X-1 | 150 | 167.40 | 171.76 | 4.36 |
| 19X-2 | 131 | 168.90 | 173.26 | 4.36 |
| 19X-CC | 18 | 170.21 | 174.57 | 4.36 |
| 20X-1 | 150 | 177.10 | 181.46 | 4.36 |
| 20X-2 | 99 | 178.60 | 182.96 | 4.36 |
| 20X-CC | 101 | 79.59 | 183.95 | 4.36 |
| 21X-1 | 150 | 186.70 | 191.06 | 4.36 |
| 21X-2 | 150 | 188.20 | 192.56 | 4.36 |
| 21X-3 | 150 | 189.70 | 194.06 | 4.36 |
| 21X-4 | 150 | 191.20 | 195.56 | 4.36 |
| 21X-5 | 52 | 192.70 | 197.06 | 4.36 |
| 21X-CC | 24 | 193.22 | 197.58 | 4.36 |
| 22X-1 | 150 | 196.30 | 202.45 | 6.15 |
| 22X-2 | 150 | 197.80 | 203.95 | 6.15 |
| 22X-3 | 150 | 199.30 | 205.45 | 6.15 |
| 22X-CC | 52 | 200.80 | 206.95 | 6.15 |
| 23X-1 | 50 | 205.90 | 212.05 | 6.15 |
| 24X-1 | 93 | 215.50 | 221.65 | 6.15 |
| 26X-1 | 84 | 234.70 | 240.85 | 6.15 |
| 27X-1 | 135 | 244.30 | 250.45 | 6.15 |
| 27X-CC | 18 | 245.65 | 251.80 | 6.15 |
| 28X-1 | 150 | 254.00 | 260.15 | 6.15 |
| 28X-2 | 74 | 255.50 | 261.65 | 6.15 |
| 28X-CC | 23 | 256.24 | 262.39 | 6.15 |
| 29X-1 | 150 | 259.00 | 265.15 | 6.15 |
| 29X-2 | 150 | 260.50 | 266.65 | 6.15 |
| 29X-3 | 150 | 262.00 | 268.15 | 6.15 |
| 29X-4 | 135 | 263.50 | 269.65 | 6.15 |
| 29X-CC | 26 | 264.85 | 271.00 | 6.15 |
| 30X-1 | 150 | 263.60 | 269.75 | 6.15 |
| 30X-2 | 150 | 265.10 | 271.25 | 6.15 |
| 30X-3 | 130 | 266.60 | 272.75 | 6.15 |
| 30X-4 | 34 | 267.90 | 274.05 | 6.15 |
| 31X-1 | 150 | 273.20 | 279.35 | 6.15 |
| 31X-2 | 150 | 274.70 | 280.85 | 6.15 |
| 31X-3 | 150 | 276.20 | 282.35 | 6.15 |
| 31X-4 | 150 | 277.70 | 283.85 | 6.15 |
| 31X-5 | 88 | 279.20 | 285.35 | 6.15 |
| 31X-CC | 35 | 280.08 | 286.23 | 6.15 |
| 32X-CC | 3 | 282.80 | 288.95 | 6.15 |
| 33X-CC | 9 | 292.40 | 298.55 | 6.15 |
| 34X-1 | 150 | 302.10 | 308.25 | 6.15 |
| 34X-2 | 71 | 303.60 | 309.75 | 6.15 |
| 34X-CC | 27 | 304.31 | 310.46 | 6.15 |
| 35X-1 | 150 | 311.70 | 317.85 | 6.15 |
| 35X-2 | 75 | 313.20 | 319.35 | 6.15 |
| 35X-CC | 38 | 313.95 | 320.10 | 6.15 |
| 36X-1 | 63 | 321.30 | 327.45 | 6.15 |
| 36X-CC | 36 | 321.93 | 328.08 | 6.15 |
| 37X-1 | 39 | 330.90 | 337.05 | 6.15 |
| 37X-2 | 150 | 331.29 | 337.44 | 6.15 |
| 37X-3 | 150 | 332.79 | 338.94 | 6.15 |
| 37X-4 | 150 | 334.29 | 340.44 | 6.15 |
| 37X-5 | 150 | 335.79 | 341.94 | 6.15 |
| 37X-6 | 150 | 337.29 | 343.44 | 6.15 |
| 37X-7 | 46 | 338.79 | 344.94 | 6.15 |
| 37X-8 | 66 | 339.25 | 345.40 | 6.15 |
| 37X-CC | 101 | 339.91 | 346.06 | 6.15 |
| 38X-1 | 150 | 340.60 | 346.75 | 6.15 |
| 38X-2 | 150 | 342.10 | 348.25 | 6.15 |
| 38X-3 | 150 | 343.60 | 349.75 | 6.15 |
| 38X-4 | 41 | 345.10 | 351.25 | 6.15 |
| 38X-CC | 28 | 345.51 | 351.66 | 6.15 |
| 39X-1 | 150 | 350.20 | 356.35 | 6.15 |
| 39X-2 | 150 | 351.70 | 357.85 | 6.15 |
| 39X-3 | 150 | 353.20 | 359.35 | 6.15 |
| 39X-4 | 150 | 354.70 | 360.85 | 6.15 |
| 39X-5 | 24 | 356.20 | 362.35 | 6.15 |
| 39X-CC | 119 | 356.44 | 362.59 | 6.15 |
| 40X-1 | 150 | 359.80 | 365.95 | 6.15 |
| 40X-2 | 150 | 361.30 | 367.45 | 6.15 |
| 40X-3 | 150 | 362.80 | 368.95 | 6.15 |
| 40X-4 | 150 | 364.30 | 370.45 | 6.15 |
| 40X-5 | 108 | 365.80 | 371.95 | 6.15 |
| 40X-CC | 34 | 366.88 | 373.03 | 6.15 |
| 41X-1 | 150 | 369.40 | 375.55 | 6.15 |
| 41X-2 | 150 | 370.90 | 377.05 | 6.15 |
| 41X-3 | 150 | 372.40 | 378.55 | 6.15 |
| 41X-4 | 150 | 373.90 | 380.05 | 6.15 |
| 41X-5 | 48 | 375.40 | 381.55 | 6.15 |
| 41X-CC | 41 | 375.88 | 382.03 | 6.15 |
| 42X-1 | 150 | 379.10 | 385.25 | 6.15 |
| 42X-2 | 150 | 380.60 | 386.75 | 6.15 |
| 42X-3 | 150 | 382.10 | 388.25 | 6.15 |
| 42X-4 | 118 | 383.60 | 389.75 | 6.15 |

**Table 2 (continued).**

| Core, section | Length (cm) | Depth (mbsf) | Depth (mcd) | Offset (mcd – mbsf) |
|---|---|---|---|---|
| 42X-CC | 37 | 384.78 | 390.93 | 6.15 |
| 43X-1 | 150 | 388.70 | 394.85 | 6.15 |
| 43X-2 | 150 | 390.20 | 396.35 | 6.15 |
| 43X-3 | 136 | 391.70 | 397.85 | 6.15 |
| 43X-CC | 37 | 393.06 | 399.21 | 6.15 |
| 44X-1 | 150 | 398.30 | 404.45 | 6.15 |
| 44X-2 | 150 | 399.80 | 405.95 | 6.15 |
| 44X-3 | 137 | 401.30 | 407.45 | 6.15 |
| 44X-CC | 24 | 402.67 | 408.82 | 6.15 |
| 162-986D- | | | | |
| 1R-1 | 10 | 387.80 | 387.80 | 0.00 |
| 2R-1 | 150 | 397.40 | 397.40 | 0.00 |
| 2R-2 | 150 | 398.90 | 398.90 | 0.00 |
| 2R-3 | 150 | 400.40 | 400.40 | 0.00 |
| 2R-4 | 99 | 401.90 | 401.90 | 0.00 |
| 2R-CC | 9 | 402.89 | 402.89 | 0.00 |
| 3R-17 | 2 | 407.10 | 407.10 | 0.00 |
| 3R-CC | 30 | 407.82 | 407.82 | 0.00 |
| 5R-CC | 30 | 426.30 | 426.30 | 0.00 |
| 6R-1 | 150 | 435.90 | 435.90 | 0.00 |
| 6R-CC | 18 | 437.40 | 437.40 | 0.00 |
| 7R-CC | 7 | 445.50 | 445.50 | 0.00 |
| 8R-1 | 150 | 455.10 | 455.10 | 0.00 |
| 8R-2 | 34 | 456.60 | 456.60 | 0.00 |
| 8R-CC | 11 | 456.94 | 456.94 | 0.00 |
| 9R-1 | 42 | 464.70 | 464.70 | 0.00 |
| 10R-CC | 16 | 474.30 | 474.30 | 0.00 |
| 11R-1 | 41 | 483.90 | 483.90 | 0.00 |
| 14R-1 | 150 | 512.70 | 512.70 | 0.00 |
| 14R-2 | 150 | 514.20 | 514.20 | 0.00 |
| 14R-3 | 150 | 515.70 | 515.70 | 0.00 |
| 14R-4 | 117 | 517.20 | 517.20 | 0.00 |
| 14R-CC | 25 | 518.37 | 518.37 | 0.00 |
| 15R-1 | 150 | 522.30 | 522.30 | 0.00 |
| 15R-2 | 150 | 523.80 | 523.80 | 0.00 |
| 15R-3 | 150 | 525.30 | 525.30 | 0.00 |
| 15R-4 | 150 | 526.80 | 526.80 | 0.00 |
| 15R-5 | 150 | 528.30 | 528.30 | 0.00 |
| 15R-6 | 150 | 529.80 | 529.80 | 0.00 |
| 15R-7 | 22 | 531.30 | 531.30 | 0.00 |
| 15R-CC | 22 | 531.52 | 531.52 | 0.00 |
| 16R-1 | 150 | 531.90 | 531.90 | 0.00 |
| 16R-2 | 150 | 533.40 | 533.40 | 0.00 |
| 16R-3 | 150 | 534.90 | 534.90 | 0.00 |
| 16R-4 | 150 | 536.40 | 536.40 | 0.00 |
| 16R-5 | 150 | 537.90 | 537.90 | 0.00 |
| 16R-6 | 150 | 539.40 | 539.40 | 0.00 |
| 16R-7 | 49 | 540.90 | 540.90 | 0.00 |
| 16R-CC | 12 | 541.39 | 541.39 | 0.00 |
| 17R-1 | 150 | 541.50 | 541.50 | 0.00 |
| 17R-2 | 150 | 543.00 | 543.00 | 0.00 |
| 17R-3 | 150 | 544.50 | 544.50 | 0.00 |
| 17R-4 | 42 | 546.00 | 546.00 | 0.00 |
| 17R-CC | 18 | 546.42 | 546.42 | 0.00 |
| 18R-1 | 150 | 551.10 | 551.10 | 0.00 |
| 18R-2 | 150 | 552.60 | 552.60 | 0.00 |
| 18R-3 | 150 | 554.10 | 554.10 | 0.00 |
| 18R-4 | 150 | 555.60 | 555.60 | 0.00 |
| 18R-5 | 150 | 557.10 | 557.10 | 0.00 |
| 18R-6 | 20 | 558.60 | 558.60 | 0.00 |
| 18R-CC | 15 | 558.80 | 558.80 | 0.00 |
| 19R-1 | 150 | 560.70 | 560.70 | 0.00 |
| 19R-2 | 150 | 562.20 | 562.20 | 0.00 |
| 19R-3 | 104 | 563.70 | 563.70 | 0.00 |
| 19R-CC | 14 | 564.74 | 564.74 | 0.00 |
| 20R-CC | 1 | 570.30 | 570.30 | 0.00 |
| 21R-1 | 150 | 580.00 | 580.00 | 0.00 |
| 21R-2 | 150 | 581.50 | 581.50 | 0.00 |
| 21R-3 | 150 | 583.00 | 583.00 | 0.00 |
| 21R-4 | 14 | 584.50 | 584.50 | 0.00 |
| 21R-CC | 4 | 584.64 | 584.64 | 0.00 |
| 27R-1 | 36 | 637.70 | 637.70 | 0.00 |
| 28R-1 | 150 | 647.40 | 647.40 | 0.00 |
| 28R-2 | 150 | 648.90 | 648.90 | 0.00 |
| 28R-3 | 150 | 650.40 | 650.40 | 0.00 |
| 28R-4 | 150 | 651.90 | 651.90 | 0.00 |
| 28R-5 | 150 | 653.40 | 653.40 | 0.00 |
| 28R-6 | 94 | 654.90 | 654.90 | 0.00 |
| 29R-1 | 150 | 656.90 | 656.90 | 0.00 |
| 29R-2 | 150 | 658.40 | 658.40 | 0.00 |
| 29R-3 | 150 | 659.90 | 659.90 | 0.00 |
| 29R-4 | 105 | 661.40 | 661.40 | 0.00 |
| 29R-CC | 16 | 662.45 | 662.45 | 0.00 |
| 30R-1 | 150 | 666.60 | 666.60 | 0.00 |
| 30R-2 | 150 | 668.10 | 668.10 | 0.00 |
| 30R-3 | 150 | 669.60 | 669.60 | 0.00 |
| 30R-4 | 93 | 671.10 | 671.10 | 0.00 |
| 30R-CC | 22 | 672.03 | 672.03 | 0.00 |
| 31R-1 | 150 | 676.20 | 676.20 | 0.00 |
| 31R-2 | 150 | 677.70 | 677.70 | 0.00 |
| 31R-3 | 150 | 679.20 | 679.20 | 0.00 |
| 31R-4 | 150 | 680.70 | 680.70 | 0.00 |
| 31R-5 | 45 | 682.20 | 682.20 | 0.00 |
| 31R-CC | 13 | 682.65 | 682.65 | 0.00 |
| 32R-1 | 150 | 685.80 | 685.80 | 0.00 |
| 32R-2 | 150 | 687.30 | 687.30 | 0.00 |
| 32R-3 | 150 | 688.80 | 688.80 | 0.00 |
| 32R-4 | 150 | 690.30 | 690.30 | 0.00 |
| 32R-5 | 150 | 691.80 | 691.80 | 0.00 |
| 32R-6 | 77 | 693.30 | 693.30 | 0.00 |
| 32R-CC | 13 | 694.07 | 694.07 | 0.00 |
| 33R-1 | 136 | 695.40 | 695.40 | 0.00 |
| 33R-CC | 12 | 696.76 | 696.76 | 0.00 |
| 34R-1 | 150 | 705.00 | 705.00 | 0.00 |
| 34R-2 | 80 | 706.50 | 706.50 | 0.00 |
| 34R-CC | 2 | 707.30 | 707.30 | 0.00 |
| 35R-1 | 150 | 714.60 | 714.60 | 0.00 |
| 35R-2 | 150 | 716.10 | 716.10 | 0.00 |
| 35R-3 | 150 | 717.60 | 717.60 | 0.00 |
| 35R-4 | 150 | 719.10 | 719.10 | 0.00 |
| 35R-5 | 150 | 720.60 | 720.60 | 0.00 |
| 35R-6 | 150 | 722.10 | 722.10 | 0.00 |
| 35R-7 | 64 | 723.60 | 723.60 | 0.00 |
| 35R-CC | 17 | 724.24 | 724.24 | 0.00 |
| 36R-CC | 1 | 724.20 | 724.20 | 0.00 |
| 37R-1 | 150 | 733.80 | 733.80 | 0.00 |
| 37R-2 | 150 | 735.30 | 735.30 | 0.00 |
| 37R-3 | 150 | 736.80 | 736.80 | 0.00 |
| 37R-4 | 150 | 738.30 | 738.30 | 0.00 |
| 37R-5 | 150 | 739.80 | 739.80 | 0.00 |
| 37R-6 | 150 | 741.30 | 741.30 | 0.00 |
| 37R-7 | 44 | 742.80 | 742.80 | 0.00 |
| 37R-CC | 10 | 743.24 | 743.24 | 0.00 |
| 38R-1 | 150 | 743.40 | 743.40 | 0.00 |
| 38R-2 | 150 | 744.90 | 744.90 | 0.00 |
| 38R-3 | 150 | 746.40 | 746.40 | 0.00 |
| 38R-4 | 150 | 747.90 | 747.90 | 0.00 |
| 38R-5 | 37 | 749.40 | 749.40 | 0.00 |
| 38R-CC | 11 | 749.77 | 749.77 | 0.00 |
| 39R-1 | 150 | 753.00 | 753.00 | 0.00 |
| 39R-2 | 150 | 754.50 | 754.50 | 0.00 |
| 39R-3 | 150 | 756.00 | 756.00 | 0.00 |
| 39R-4 | 150 | 757.50 | 757.50 | 0.00 |
| 39R-5 | 150 | 759.00 | 759.00 | 0.00 |
| 39R-6 | 129 | 760.50 | 760.50 | 0.00 |
| 39R-CC | 15 | 761.79 | 761.79 | 0.00 |
| 40R-1 | 150 | 762.60 | 762.60 | 0.00 |
| 40R-2 | 150 | 764.10 | 764.10 | 0.00 |
| 40R-3 | 150 | 765.60 | 765.60 | 0.00 |
| 40R-4 | 150 | 767.10 | 767.10 | 0.00 |
| 40R-5 | 150 | 768.60 | 768.60 | 0.00 |
| 40R-6 | 112 | 770.10 | 770.10 | 0.00 |
| 40R-7 | 29 | 771.22 | 771.22 | 0.00 |
| 41R-1 | 150 | 772.20 | 772.20 | 0.00 |
| 41R-2 | 150 | 773.70 | 773.70 | 0.00 |
| 41R-3 | 150 | 775.20 | 775.20 | 0.00 |
| 41R-4 | 150 | 776.70 | 776.70 | 0.00 |
| 41R-5 | 143 | 778.20 | 778.20 | 0.00 |
| 41R-6 | 19 | 779.63 | 779.63 | 0.00 |
| 42R-1 | 150 | 781.80 | 781.80 | 0.00 |
| 42R-2 | 150 | 783.30 | 783.30 | 0.00 |
| 42R-3 | 150 | 784.80 | 784.80 | 0.00 |
| 42R-4 | 150 | 786.30 | 786.30 | 0.00 |
| 42R-5 | 150 | 787.80 | 787.80 | 0.00 |
| 42R-6 | 141 | 789.30 | 789.30 | 0.00 |
| 42R-CC | 15 | 790.71 | 790.71 | 0.00 |
| 43R-1 | 150 | 791.40 | 791.40 | 0.00 |
| 43R-2 | 150 | 792.90 | 792.90 | 0.00 |
| 43R-3 | 74 | 794.40 | 794.40 | 0.00 |
| 43R-CC | 18 | 795.14 | 795.14 | 0.00 |
| 44R-1 | 150 | 801.10 | 801.10 | 0.00 |
| 44R-2 | 150 | 802.60 | 802.60 | 0.00 |
| 44R-3 | 150 | 804.10 | 804.10 | 0.00 |
| 44R-4 | 108 | 805.60 | 805.60 | 0.00 |
| 44R-CC | 20 | 806.68 | 806.68 | 0.00 |
| 45R-1 | 150 | 810.70 | 810.70 | 0.00 |
| 45R-2 | 150 | 812.20 | 812.20 | 0.00 |
| 45R-3 | 150 | 813.70 | 813.70 | 0.00 |
| 45R-4 | 150 | 815.20 | 815.20 | 0.00 |
| 45R-5 | 150 | 816.70 | 816.70 | 0.00 |
| 45R-6 | 150 | 818.20 | 818.20 | 0.00 |
| 45R-7 | 64 | 819.70 | 819.70 | 0.00 |
| 45R-CC | 10 | 820.34 | 820.34 | 0.00 |
| 46R-1 | 150 | 820.30 | 820.30 | 0.00 |
| 46R-2 | 150 | 821.80 | 821.80 | 0.00 |
| 46R-3 | 150 | 823.30 | 823.30 | 0.00 |
| 46R-4 | 96 | 824.80 | 824.80 | 0.00 |
| 47R-1 | 150 | 829.90 | 829.90 | 0.00 |

Table 2 (continued).

| Core, section | Length (cm) | Depth (mbsf) | Depth (mcd) | Offset (mcd – mbsf) |
|---|---|---|---|---|
| 47R-2 | 150 | 831.40 | 831.40 | 0.00 |
| 47R-3 | 36 | 832.90 | 832.90 | 0.00 |
| 47R-CC | 27 | 833.26 | 833.26 | 0.00 |
| 48R-1 | 150 | 839.50 | 839.50 | 0.00 |
| 48R-2 | 99 | 841.00 | 841.00 | 0.00 |
| 48R-CC | 23 | 841.99 | 841.99 | 0.00 |
| 49R-1 | 122 | 849.20 | 849.20 | 0.00 |
| 49R-2 | 52 | 850.42 | 850.42 | 0.00 |
| 50R-1 | 150 | 858.80 | 858.80 | 0.00 |
| 50R-2 | 150 | 860.30 | 860.30 | 0.00 |
| 50R-3 | 150 | 861.80 | 861.80 | 0.00 |
| 50R-4 | 150 | 863.30 | 863.30 | 0.00 |
| 50R-5 | 112 | 864.80 | 864.80 | 0.00 |
| 50R-CC | 3 | 865.92 | 865.92 | 0.00 |
| 51R-1 | 132 | 868.40 | 868.40 | 0.00 |
| 51R-2 | 150 | 869.72 | 869.72 | 0.00 |
| 51R-3 | 150 | 871.22 | 871.22 | 0.00 |
| 51R-4 | 150 | 872.72 | 872.72 | 0.00 |
| 51R-5 | 130 | 874.22 | 874.22 | 0.00 |
| 51R-6 | 150 | 875.52 | 875.52 | 0.00 |
| 51R-7 | 80 | 877.02 | 877.02 | 0.00 |
| 51R-CC | 18 | 877.82 | 877.82 | 0.00 |
| 52R-1 | 150 | 878.10 | 878.10 | 0.00 |
| 52R-2 | 150 | 879.60 | 879.60 | 0.00 |
| 52R-3 | 150 | 881.10 | 881.10 | 0.00 |
| 52R-4 | 150 | 882.60 | 882.60 | 0.00 |
| 52R-5 | 150 | 884.10 | 884.10 | 0.00 |
| 52R-6 | 150 | 885.60 | 885.60 | 0.00 |
| 52R-7 | 65 | 887.10 | 887.10 | 0.00 |
| 52R-CC | 2 | 887.75 | 887.75 | 0.00 |
| 53R-1 | 150 | 887.60 | 887.60 | 0.00 |
| 53R-2 | 150 | 889.10 | 889.10 | 0.00 |
| 53R-3 | 150 | 890.60 | 890.60 | 0.00 |
| 53R-4 | 150 | 892.10 | 892.10 | 0.00 |
| 53R-5 | 150 | 893.60 | 893.60 | 0.00 |
| 53R-6 | 150 | 895.10 | 895.10 | 0.00 |
| 53R-7 | 22 | 896.60 | 896.60 | 0.00 |
| 53R-CC | 17 | 896.82 | 896.82 | 0.00 |
| 54R-1 | 86 | 897.30 | 897.30 | 0.00 |
| 54R-CC | 18 | 898.16 | 898.16 | 0.00 |
| 55R-1 | 150 | 906.90 | 906.90 | 0.00 |
| 55R-2 | 112 | 908.40 | 908.40 | 0.00 |
| 55R-CC | 23 | 909.52 | 909.52 | 0.00 |
| 57R-1 | 150 | 926.10 | 926.10 | 0.00 |
| 57R-2 | 108 | 927.60 | 927.60 | 0.00 |
| 57R-CC | 27 | 928.68 | 928.68 | 0.00 |
| 58R-1 | 150 | 935.70 | 935.70 | 0.00 |
| 58R-2 | 39 | 937.20 | 937.20 | 0.00 |
| 58R-CC | 2 | 937.59 | 937.59 | 0.00 |
| 59R-1 | 150 | 945.30 | 945.30 | 0.00 |
| 59R-2 | 150 | 946.80 | 946.80 | 0.00 |
| 59R-3 | 150 | 948.30 | 948.30 | 0.00 |
| 59R-4 | 26 | 949.80 | 949.80 | 0.00 |
| 59R-CC | 24 | 950.06 | 950.06 | 0.00 |
| 60R-1 | 147 | 955.00 | 955.00 | 0.00 |
| 60R-CC | 26 | 956.47 | 956.47 | 0.00 |

Note: Depths are from the top of each section.

## Description of Lithostratigraphic Units

### *Unit I*

Interval:
Sections 162-986A-1H through 12H-2
Cores 162-986B-1H through 2H (base of hole)
Cores 162-986C-1H through 11X
Age: Holocene to late Pleistocene
Depth: 0 to 98.0 mbsf

Lithostratigraphic Unit I is primarily defined by the presence of relatively common calcareous nannofossils and spectral reflectance values which, in general, vary between 5% and 15% within the red band (650–700-nm) (Fig. 6). High amplitude fluctuations and a downcore decrease in average spectral reflectance values are also observed in Unit I. In addition, the lower boundary of this unit is marked by a decrease in the silt content (Fig. 7). The sediments contain up to 30% carbonate, but average only 6.4% (see "Organic Geochemistry" section, this chapter). The sediments of Unit I are predominantly dark gray to very dark greenish gray silty clay and clay with silt. In addition, interbedded layers of dark greenish gray clayey nannofossil mixed sediment, brown nannofossil silty clay, very dark greenish gray silty clay with nannofossils, and dark gray nannofossil clay with silt are present in minor amounts. Most color changes are gradational. Magnetic susceptibility and natural gamma radiation values exhibit no systematic trends within Unit I.

Numerous dropstones, some as large as 7.9 cm, were identified throughout this Unit I (Table 4; Fig. 7). Sedimentary rocks are the predominant rock type among the dropstones in this sequence. Also, several silty to sandy, millimeter- to decimeter-thick layers appear (Fig. 8). Smear slide analysis indicates that quartz, feldspar, and inorganic calcite are the most common terrigenous silt- and sand-sized particles. XRD analysis also reveals that quartz, plagioclase, pyroxene, and clay minerals are common components of the bulk sediments in this interval. Sulfides are found throughout the unit, predominantly as disseminated pyrite with a few pyrite concretions. Finally, disseminated volcanic ash is also present throughout, while discrete ash layers were not observed. Slight to moderate bioturbation is common at all depths.

### *Unit II*

Interval:
Section 162-986A-12H-2 through Core 24X (base of hole)
Cores 162-986C-12X through Core 44X (base of hole)
Core 162-986D-1R through Section 19R-1
Age: early Pleistocene to late Pleistocene
Depth: 98.0 to 561.8 mbsf

The sediments of Unit II comprise the bulk of the sedimentary sequence at Site 986. The unit is composed exclusively of dark to very dark greenish gray and dark to very dark gray silty clay and clay with silt. The upper boundary of Unit II is defined, in part, by the diminished presence of biocarbonate which is limited to the uppermost part of Unit II. The most significant change is the increase in the amount of dropstones within this unit. Up to 30 dropstones per core as large as 16.5 cm were found throughout this unit (Figs. 9, 10). Sedimentary rocks are common among the dropstones of this Unit. The number of igneous and/or metamorphic rock fragments increase in the interval 380–550 mbsf (Table 5; Fig. 7). However, terrigenous silt- and sand-sized components such as quartz and feldspar are relatively invariant across the boundary of Units I and II, in contrast to the disappearance of biogenic material. The few scattered measurements of spectral reflectance values in Unit II are generally lower than in Unit I. A small downcore increase in natural gamma emissions marks the top of Unit II, followed by highly variable wireline log natural gamma counts throughout most of this unit (Fig. 6). Magnetic susceptibility exhibits considerable scatter within Unit II.

Unit II sediments are predominantly composed of clay, quartz, feldspar, mica, and accessory minerals. Smear slide analysis reveals that Unit II, along with Unit I, contains relatively constant amounts of quartz, feldspar, and mica throughout the sequence. XRD analysis also demonstrates that the abundance of quartz, plagioclase, and pyroxene within Unit II is relatively stable and changes only slightly in relation to the overlying sediments. Other sediment characteristics include isolated spikes of high inorganic carbonate content superimposed on a carbonate-poor background and numerous well defined millimeter- to decimeter-scale sandy to silty layers and reworked shell fragments that occur in the uppermost part of this unit. Finally,

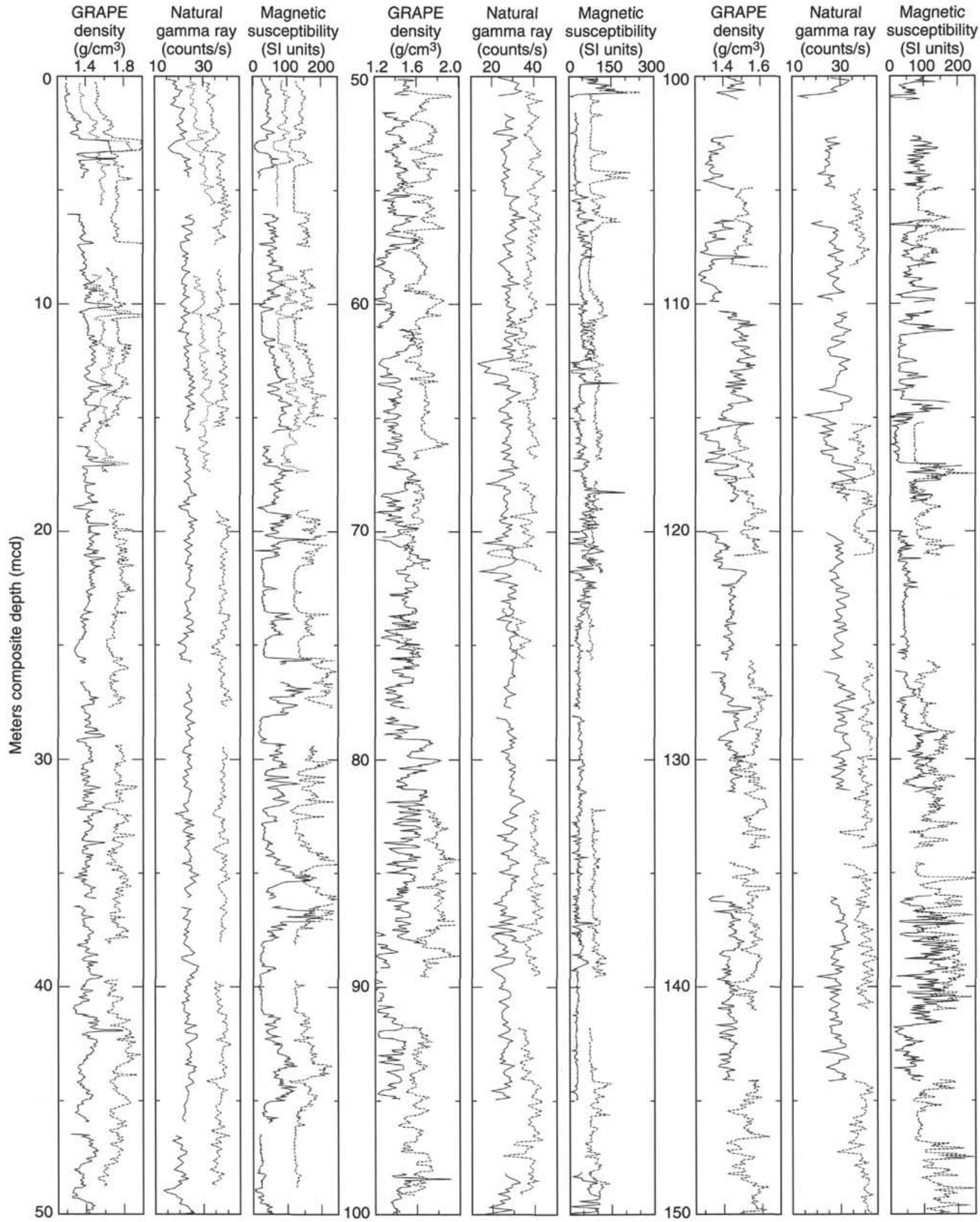


Figure 4. GRAPE density, natural gamma radiation, and magnetic susceptibility data from Site 986 on the mcd (meters composite depth) scale. Lines for Holes 986B (dotted) and 986C (dashed) have been horizontally offset from line for Hole 986A (solid) for better display; therefore, values given on horizontal scale are the true values only for Hole 986A. (See also back pocket.)

**Table 3. Site 986 splice tie points.**

| Hole, core, section (cm) | Depth (mbsf) | Depth (mcd) | | Hole, core, section (cm) | Depth (mbsf) | Depth (mcd) |
|---|---|---|---|---|---|---|
| 162-986- | | | | 162-986- | | |
| A-1H-2, 95 | 2.44 | 2.44 | tie to | C-1H-2, 83 | 2.33 | 2.44 |
| C-1H-5, 121 | 7.21 | 7.32 | tie to | A-2H-1, 136 | 5.96 | 7.32 |
| A-2H-6, 38 | 12.47 | 13.83 | tie to | B-2H-4, 68 | 11.18 | 13.83 |
| B-2H-6, 113 | 14.63 | 17.28 | tie to | A-3H-1, 113 | 15.22 | 17.28 |
| A-3H-6, 83 | 22.42 | 24.48 | tie to | C-3H-4, 103 | 22.53 | 24.48 |
| C-3H-6, 86 | 25.35 | 27.30 | tie to | A-4H-1, 77 | 24.36 | 27.30 |
| A-4H-3, 119 | 27.78 | 30.72 | tie to | C-4H-1, 143 | 27.92 | 30.72 |
| C-4H-5, 131 | 33.81 | 36.61 | tie to | A-5H-1, 26 | 33.35 | 36.61 |
| A-5H-4, 74 | 38.34 | 41.60 | tie to | C-5H-3, 32 | 37.99 | 41.60 |
| C-5H-7, 95 | 44.63 | 48.24 | tie to | A-6H-2, 34 | 44.44 | 48.24 |
| A-6H-3, 127 | 46.87 | 50.67 | tie to | C-6H-1, 14 | 45.64 | 50.67 |
| C-44X-3, 131 | 402.61 | 408.76 | tie to | D-6R-1, 0 | 435.90 | 435.90 |
| D-60R-1, 140 | 956.40 | 956.40 | | | | |

wireline logging results show an increased number of larger than 10-m-thick intervals of increased resistivity within the interval between 235 and 550 mbsf, interpreted as debris-flow deposits (see "Wireline Logging" section this chapter).

### *Unit III*

Interval: Sections 162-986D-19R-1 through 45R-CC
Age: early Pliocene(?)
Depth: 561.8 to 820.3 mbsf

Unit III is primarily characterized by relatively high sand content and the absence of dropstones (Fig. 7). Recovery is generally good within the lower two-thirds of this unit and poor in the upper third (564.9 to 647.4 mbsf). The primary lithologies of Unit III are very dark gray to very dark greenish gray silty clay with sand, clayey silt with sand, silty clay, and sandy silty clay. Unit III is characterized by the re-occurrence of biogenic calcareous sediment, which is present in trace to minors amounts throughout the unit. This biocarbonate, predominantly calcareous nannofossils in amounts of up to 20%, shows a slight increase downcore. However, as in Unit I, a few spikes of high carbonate content are superimposed on a carbonate-poor background with values never exceeding 6.0% (see "Organic Geochemistry" section, this chapter). The upper boundary of Unit III is marked by a sharp downcore increase in siliciclastic silt and sand (Fig. 7). XRD analysis of the bulk sediments reveals that feldspar, quartz, illite, and pyroxene are, on average, present to a much higher extent than in Units I and II, although relatively variable throughout this unit.

Authigenic iron sulfides, primarily in the form of disseminated pyrite, are commonly present in minor amounts. Thin layers (1 mm) of silty sediments in some of the fine-grained intervals and beds dipping at varying angles (5°–70°), most probably due to natural sedimentary processes, are common toward the base of this unit (Fig. 11).

### *Unit IV*

Interval: Cores 162-986D-46R through 60R (base of hole)
Age: early Pliocene
Depth: 820.3 to 964.6 mbsf

The silty clays of Unit IV comprise the deepest sediments recovered at this site (Hole 986D). The transition from Unit III to Unit IV is marked by a decrease in sand- and silt-sized sediment components (Fig. 7). Two subunits have been defined on the basis of shipboard XRD analysis, biocarbonate content, variations in the amount and composition of sand-sized particles, and degree of consolidation (Table 4; Fig. 7)

Subunit IVA (820.3–897.3 mbsf) is distinguished from the underlying sediments by higher magnetic susceptibility values and higher sand content. The sediments are predominantly composed of dark gray to black silty clay. with minor amounts of dark gray to black silty clay with sand. Biocarbonate is present in minor amounts within this subunit, averaging 2.8% (see "Organic Geochemistry" section, this chapter). Also, agglutinated benthic foraminifers were observed in moderate amounts on the surfaces of some split cores.

Color bands are observed throughout Subunit IVA. Although the color bands are primarily horizontal, some beds dip at varying angles mostly between 15° and 45° (Fig. 12). There is evidence of sediment disturbance (contorted beds) due to natural processes towards the base of this subunit. Multiple mud-filled veins are present (Fig. 13) that are similar to veins reported at active margins (Lindsley-Griffin et al., 1990).

Subunit IVB (820.3–897.3 mbsf) is distinguished from the overlying sediments by very low magnetic susceptibility values, a further decrease in sand content and by the absence of biocarbonates (Fig. 7). Also, XRD analyses indicate marked decreases in quartz, feldspar, and pyroxene at this sub-boundary. Despite the poor recovery, available natural gamma counts seem to exhibit higher amplitude variations in Subunit IVB compared to Subunit IVA.

Subunit IVB is entirely composed of very dark gray to black silty clay. Silt- and sand-sized terrigenous components are less abundant than in Subunit IVA. In addition, bulk mineral XRD analyses reveal that the amount of smectite and chlorite is slightly higher in Subunit IVB than in Subunit IVA above. As in shallower units, carbonate content remains very low. Inorganic carbonate, which occurs sporadically throughout the whole subunit, accounts for the carbonate content in these lowermost sediments (see "Organic Geochemistry" section, this chapter). Other lithologic differences between Subunit IVB and the sediments above are a marked decrease in bulk density and *P*-wave velocity, and a corresponding increase in water content and porosity (see "Physical Properties" section, this chapter).

## Interpretation

Although age constraints are relatively weak throughout the whole sedimentary sequence, sedimentation rates at Site 986 appear to have remained between 160 and 360 m/m.y. from Pliocene to Holocene (see "Sedimentation Rates" section, this chapter). These sedimentation rates are higher than at any other site drilled during Leg 162.

Given an age estimate of <3.6 Ma for the lowermost sediments of Site 986 (see "Biostratigraphy" section, this chapter), the whole sediment sequence probably reflects changes in glacial regimes in the Svalbard–Barents Sea area. Fram Strait seems to have been influenced by small-scale continental ice sheets since at least 7.5 Ma (Wolf-Welling et al., in press). The fine-grained sediments of Unit IV together with the low but significant biocarbonate content of Subunit IVA may reflect climatically driven productivity changes during the early Pliocene at Site 986. The increase in sand content from Subunit IVA to Unit III sediments, therefore, probably indicates the transition into the period of Northern Hemisphere glaciation, and overall climatic cooling. The observed change in texture and composition of the sediment resulted from increased continental erosion, and thus greater delivery of coarse-fraction (silt and sand) sediments to the Fram Strait. This is consistent with the first massive input of ice-rafted debris to the Norwegian Sea at approximately 2.6 Ma (Jansen et al., 1988). The increase in sand content within this site may be related to enhanced mass-wasting activity during this time interval. Although only few distinct silty to sandy layers have been observed within this sequence, possible mass-wasting activity is indicated by a number of sediment structures, such as inclined beds, contorted beds, and other slumping features. Slumping and sliding also can contribute to vein formation by producing sudden loading and by producing microstructures that localize veins (Lindsley-Griffin et al., 1990). The conspicuous lack of gravel within Unit III may be related to the size of

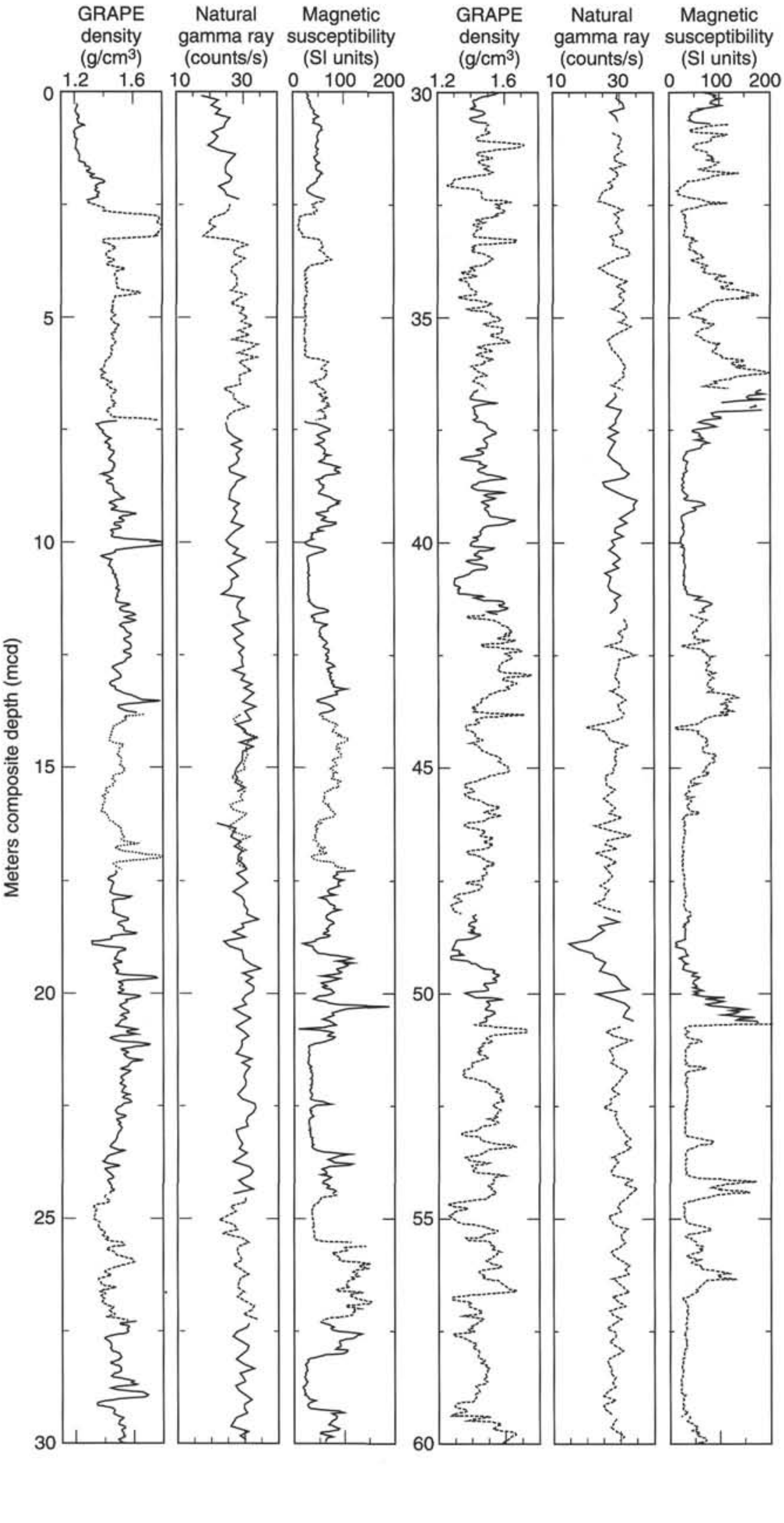


Figure 5. Spliced records of GRAPE density, natural gamma radiation, and magnetic susceptibility from Site 986. Tie points for forming the splice are given in Table 3. Holes are: 986A (solid), 986B (dotted), and 986C (dashed).

**Table 4. Description of the lithostratigraphic units at Site 986.**

| Unit | Subunit | Depth (mbsf) | Thickness (m) | Age | Lithology and characteristic features |
|---|---|---|---|---|---|
| I | | 0–98.0 | 98.0 | Holocene–"late" Pleist. | Silty clay and clay with silt interbedded with nannofossil mixed sediment and silty clay with nannofossils. Moderate amounts of dropstones, reflectance decrease at base. |
| II | | 98.0–561.8 | 463.8 | "late"–"early" Pleist. | Silty clay with minor occurrence of clay with silt. Few silty clay with inorganic calcite and/or sand. Dominant dropstones, at the most no biogenics. Highly variable natural gamma radiation and magnetic susceptibility throughout the unit. |
| III | | 561.8–820.3 | 258.5 | "late" Pleist.–early Plio. (?) | Clayey silt with sand, silty clay with sand, and clayey silt with nannofossils. Sediment is hard and fractured throughout the interval. High sand content although dropstones nearly absent. |
| IV | | 820.3–964.6 | 144.3 | early Pliocene (?) | |
| | IVA | 820.3–897.3 | 77.0 | early Pliocene (?) | Silty clay, with minor occurrence of clay with silt. Nearly barren in dropstones, few nannofossils. Common sand content; visible dipped beds and slump structures. |
| | IVB | 897.3–964.6 | 67.3 | early Pliocene (?) | Silty clay, nearly barren in dropstones and no biogenics. Very low sand content, and decrease in quartz, pyroxene and feldspar. |

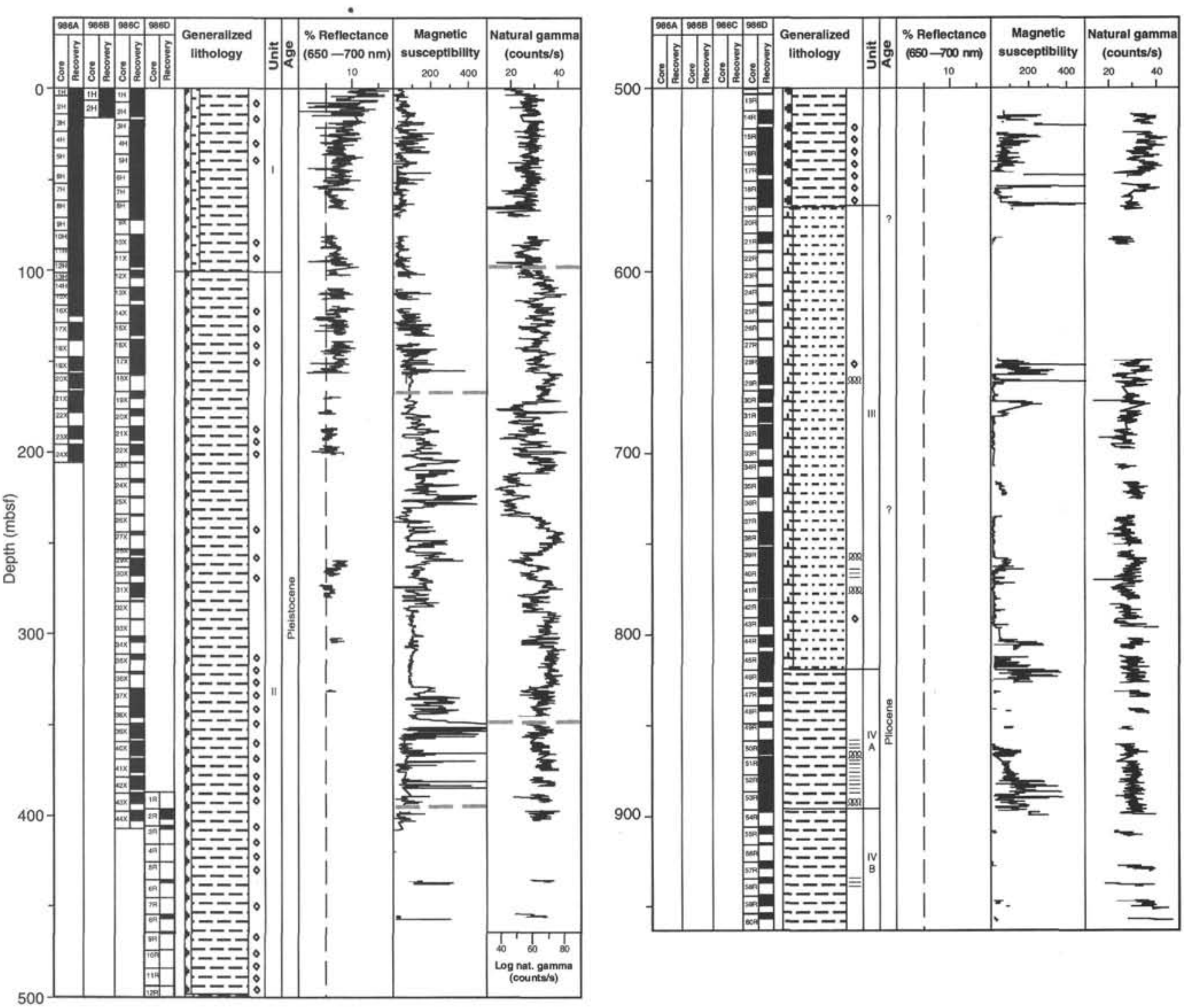


Figure 6. Core recovery, lithostratigraphy, age, spectral reflectance (red band), magnetic susceptibility, and natural gamma radiation of sediments recovered in Holes 986A, 986B, 986C, and 986D. Cores containing dropstones (diamonds) are shown in column adjacent to the lithostratigraphy. Spectral reflectance, magnetic susceptibility, and natural gamma radiation records are from Holes 986C and 986D. Magnetic susceptibility data and natural gamma radiation plotted between dashed lines originate from measurements made during the wireline logging of Hole 986C. (Key to symbols used in the "Generalized Lithology" column can be found in fig. 4, "Explanatory Notes" chapter, this volume.)

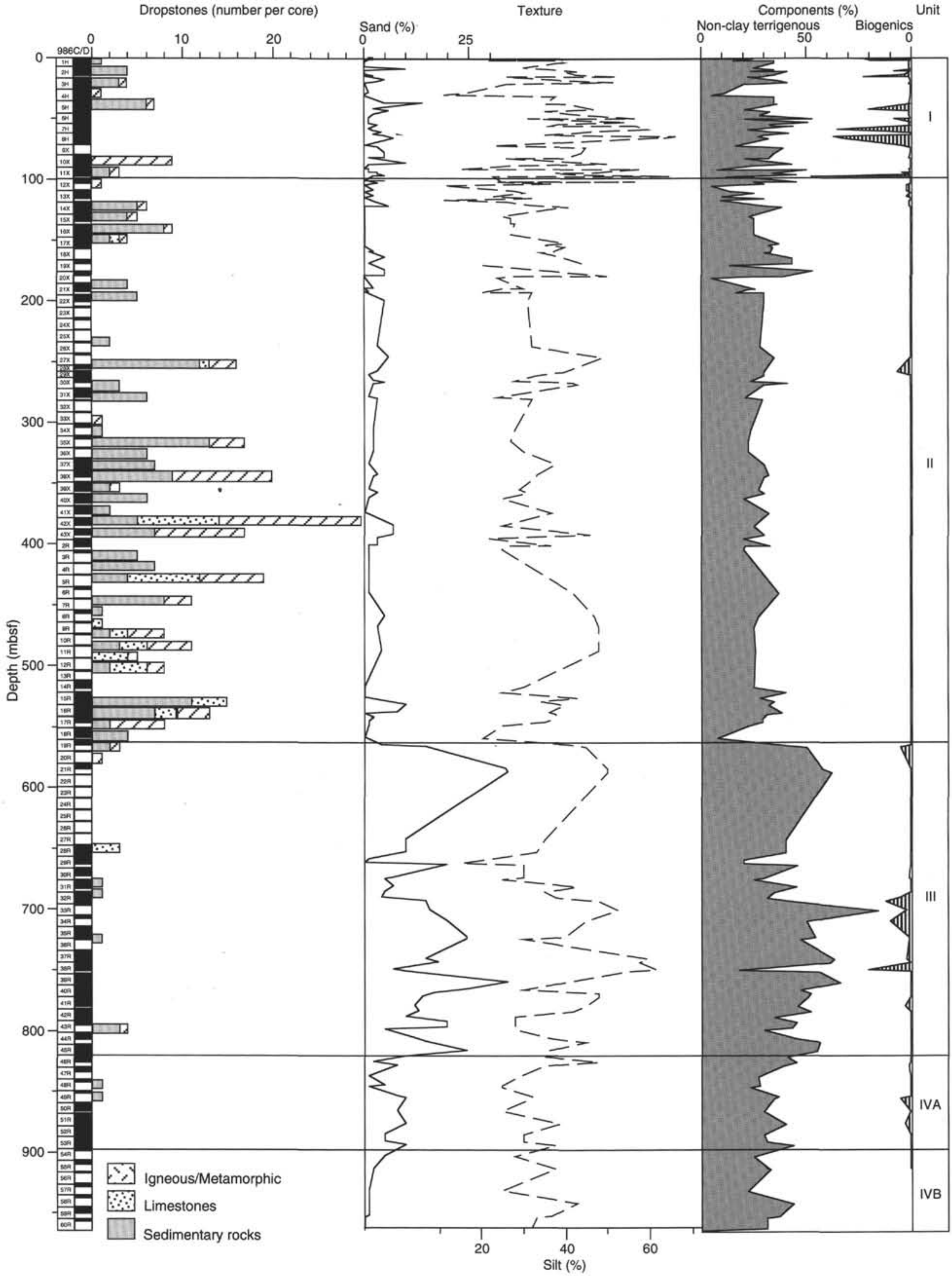


Figure 7. Core recovery, amount and composition of dropstones, content of sand- and silt-sized grains derived from smear slide analysis, and major sediment components of sediments recovered in Holes 986C and 986D. Solid line = percentage of sand; dashed line = percentage of silt. Shaded area is nonclay terrigenous component and hatched area is biogenic component.

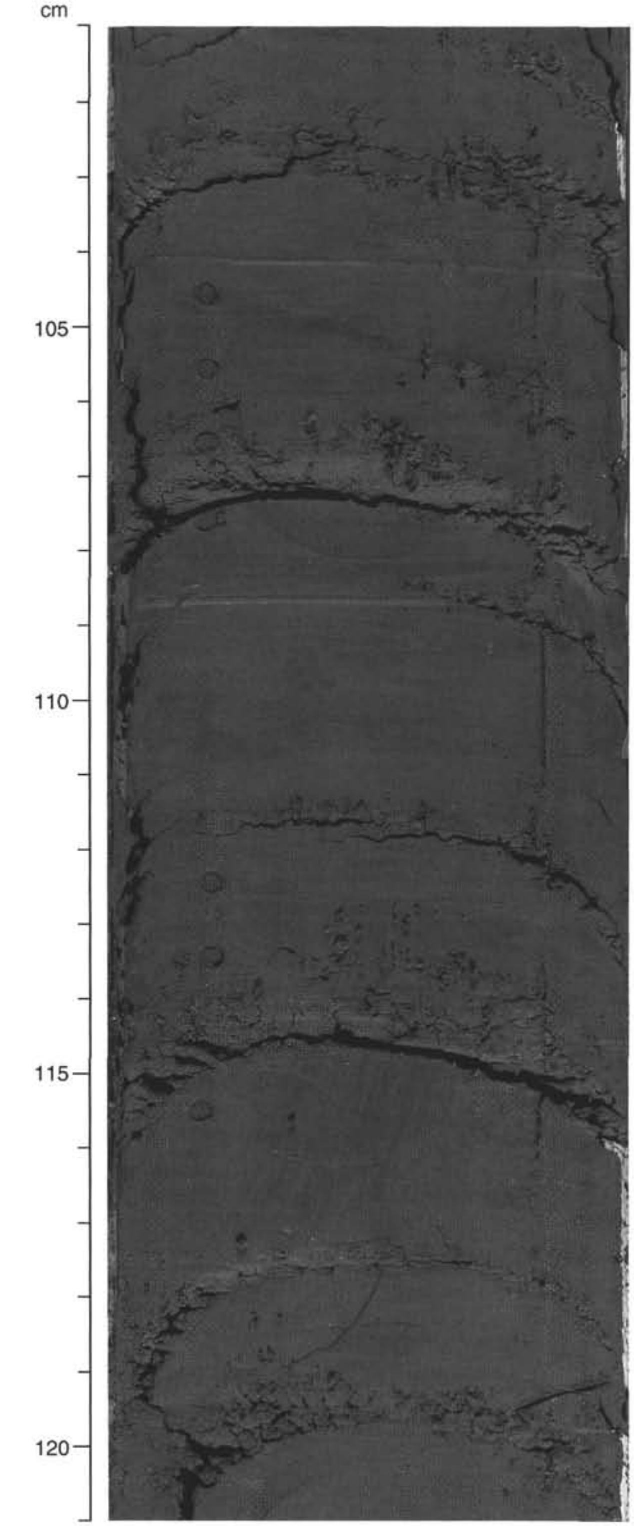


Figure 8. Photograph showing fine-scaled interbedded silty and clayey layers found in Section 162-986A-5H-3, 101–121 cm (36.91–37.11 mbsf).

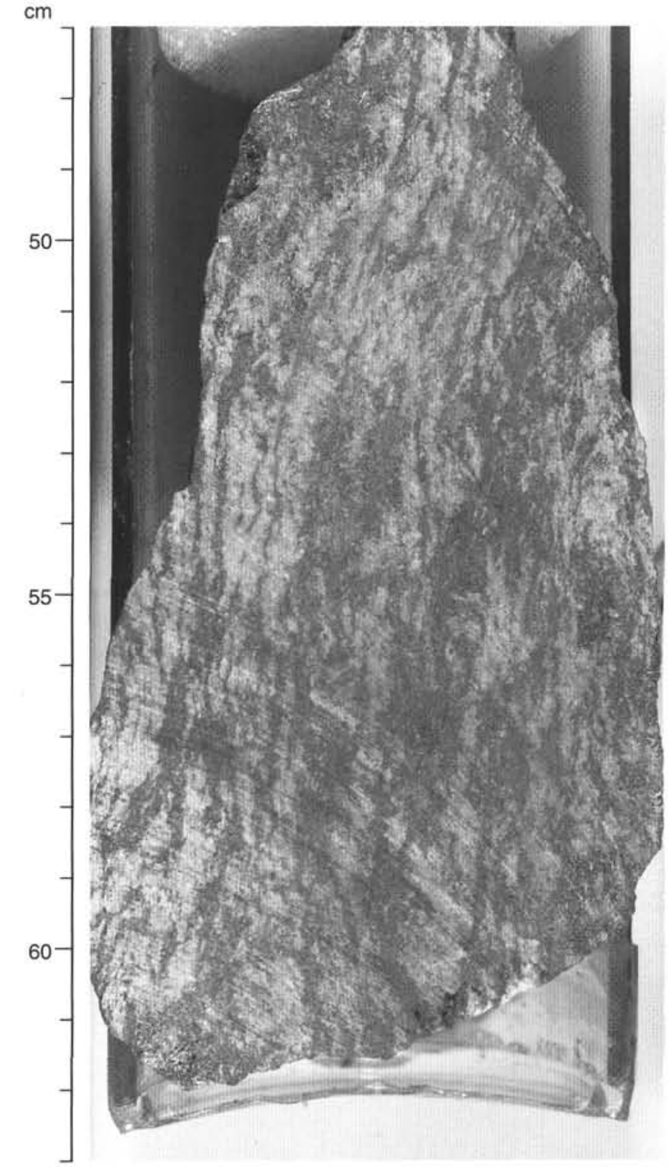


Figure 9. Photograph showing a large 16.5-cm-sized dropstone (amphibolite schist?) found in the core-catcher Section 162-986A-11H-CC, 47–63 cm (95.51 mbsf).

the ice sheets, which probably did not reach the shelf break during this period. In addition, the occurrence of calcareous nannofossils in Unit III suggests at least seasonal ice-free conditions in this area during this interval. Similar short-term improvements of relatively cold, severe surface-water conditions have been previously reported for the Norwegian-Greenland Sea as early as 2.1 Ma (Jansen et al., 1988; Henrich and Baumann, 1994).

A dramatic change in terrigenous sediment input is evident between the lower (Units III and IV) and upper (Units I and II) portions of the site 986 sediment sequence. Increases in centimeter-sized dropstones in the upper part of the record suggest increased glaciation during the Pleistocene. The presence of biocarbonate in Unit III suggests at least seasonal intrusions of temperate Atlantic water to the Fram Strait, which may have served as a local moisture source. The ice sheets thus could increase significantly in size and advance onto the shelf, generating the shift in the sedimentation process. Large

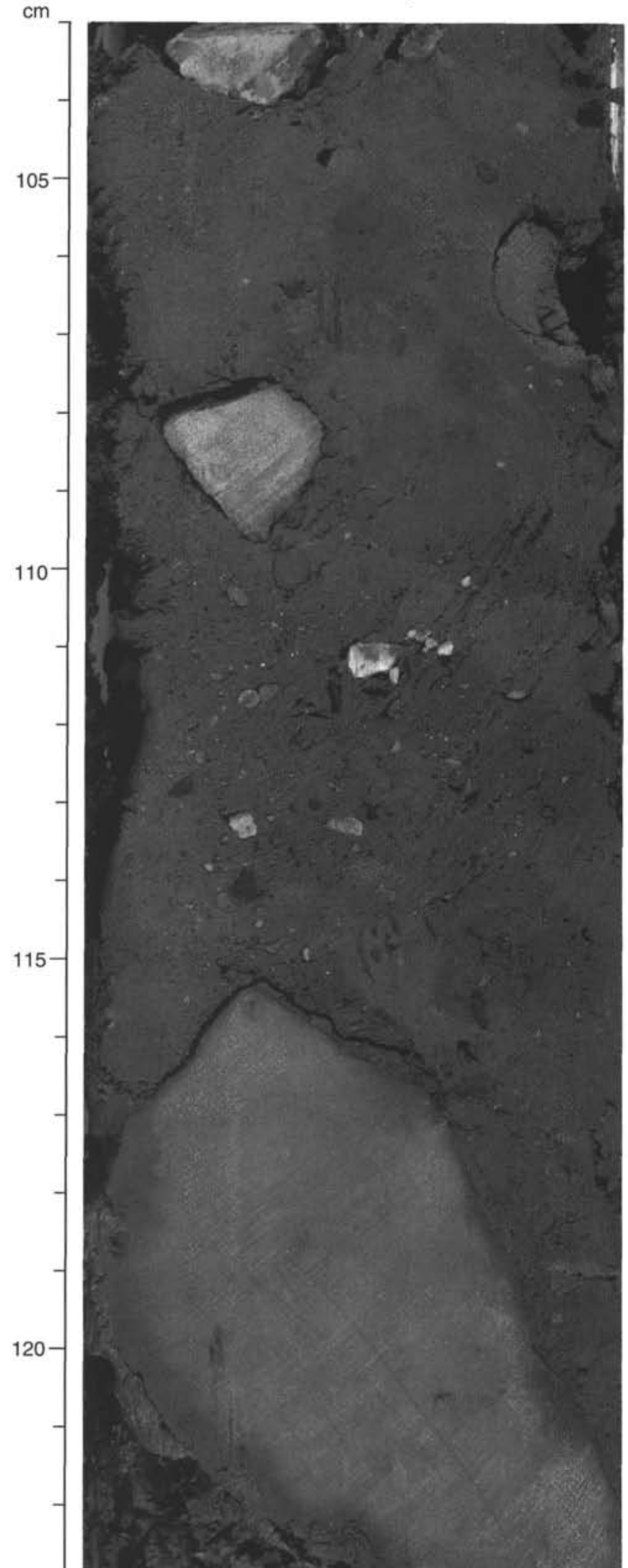


Figure 10. Photograph showing a typical part of a debris-flow deposit with several centimeter-sized dropstones found in Section 162-986C-28X-1, 103–123 cm (255.03–255.23 mbsf).

amounts of coarse material could be released at the shelf break and on the shelf during such advances and/or the subsequent retreat. In addition, increased calving at the shelf break would increase the delivery of coarse material to the deep sea. Therefore, dropstone fluctuations may possibly reflect oscillations of the ice-sheet front (Baumann et al., 1995). However, most of the sediments of Unit II are likely the result of gravity-driven debris flows possibly initiated by an active ice margin on the outer shelf. This interpretation is supported by the presence of reworked shell fragments in these deposits, combined with reduced core recovery, physical properties data, and logging results (see "Physical Properties" and "Wireline Logging" sections, this chapter). The dominant sedimentation process in the younger, uppermost 230 mbsf is likely turbiditic downslope sediment transport. Numerous silty to sandy, millimeter- to decimeter-sized layers commonly appear, whereas the number and thickness of larger scale debris-flow deposits decrease. This is also indicated in the seismic record (see "Seismic Stratigraphy" section, this chapter). In general, the presence of large debris-flow deposits would also help inflate the sedimentation rates at this site (see "Sedimentation Rates" section, this chapter).

The upsection increase in calcareous nannofossils at the base of Unit I (98 mbsf; >0.5 Ma) most probably marks the first recorded major intrusion of temperate Atlantic water far northward since deposition of Unit III sediments. Variations in the biocarbonate record of Unit I may therefore indicate glacial/interglacial oscillations. The more scattered occurrences of dropstones in the uppermost 230 mbsf compared to the lowermost part of Unit II could also imply increased ice-rafted deposition due to iceberg trajectories and/or increased melting over the site.

## BIOSTRATIGRAPHY

Microfossils are generally rare to few at Site 986; they are absent in many cores (Fig. 14). Siliceous microfossils were observed in only two samples. Of the calcareous microfossil groups, nannofossils have slightly broader stratigraphic distribution in the sequence than planktonic foraminifers. Apparently, many of the calcareous microfossils have been dissolved. Only a few biostratigraphic datums could be used to provide age constraints for the sequence (see "Sedimentation Rates" section, this chapter). In particular, biostratigraphy suggests that Core 162-986D-54X, which is just above seismic Reflector 7, has an age between 2.4 and 3.6 Ma. The lowermost six cores from this site are barren of microfossils.

### Calcareous Nannofossils

About 230 samples from this site were examined for nannofossils, which fluctuate considerably in abundance. Much of the interval between 150 and 540 mbsf and the interval below 910 mbsf is barren of nannofossils (Fig. 14). Age-diagnostic species are few, and they occur very sporadically in the sequence, resulting in low biostratigraphic resolution.

The lowest occurrence of *Emiliania huxleyi* is recorded in Sample 162-986A-8H-CC. This would suggest an age younger than oxygen isotope Stage 8 (~0.26 Ma). This age appears to be in conflict with the diatom data for Sample 162-986A-7H-CC, which is estimated as older than 0.3 Ma. As *E. huxleyi* is generally the smallest nannofossil species (~3 μm) and is difficult to identify on a light microscope with complete certainty and shore-based SEM examination is needed to resolve the problem.

The highest occurrence of *Pseudoemiliania lacunosa* is in Sample 162-986A-15X-CC; this suggests that the sample is older than 0.46 Ma. Below this level samples generally contain a few non-age-diagnostic species (e.g., *Coccolithus pelagicus, Reticulofenestra productus,* and *R. minuta*) or are barren of nannofossils. However, two

**Table 5. Summary table of dropstones greater than 2 cm in size found at Site 986.**

| Core, section, interval top (cm) | Depth (mbsf) | Size (cm) | Composition | Sediment color | Shape |
|---|---|---|---|---|---|
| 162-986A- | | | | | |
| 1H-2, 108 | 2.58 | 2.0 | Syenite | Pink | Subangular |
| 3H-6, 15 | 21.75 | 4.5 | Granite | | Angular |
| 4H-3, 14 | 26.74 | 3.3 | Schist | Black | Subangular |
| 4H-5, 146 | 31.06 | 3.7 | Layered sandstone | | |
| 5H-4, 72 | 38.32 | 5.8 | Quartz-rich sandstone | | Subrounded |
| 5H-4, 98 | 38.58 | 7.9 | Quartz-rich sandstone | | Subrounded |
| 5H-5, 9 | 39.19 | 2.2 | Highly weathered sandstone | Brown | |
| 5H-5, 18 | 39.28 | 2.0 | Siltstone | Black | Subrounded |
| 5H-5, 56 | 39.66 | 2.4 | Siltstone | Black | Subrounded |

**Only a part of this table is reproduced here. The entire table appears on the CD-ROM (back pocket).**

specimens of *P. lacunosa* were found in Sample 162-986D-55R-CC, suggesting an age younger than 3.6 Ma. The last sample with nannofossils present (Sample 162-986D-54R-CC) contains abundant *R. producta* and common *C. pelagicus* with the absence of *Reticulofenestra pseudoumbilicus,* and thus is most likely younger than 3.6 Ma (late Pliocene).

### Planktonic Foraminifers

Site 986 planktonic foraminifers are generally rare to few from the top of the sequence to Sample 162-986C-16X-CC, and preservation is good. Samples are often barren from Sample 162-986C-17X-CC to the bottom of the sequence (Sample 162-986D-60R-CC), except for certain intervals (Fig. 14). In particular, rare *Neogloboquadrina pachyderma* (sinistrally coiling) are observed in Samples 162-986D-14R-CC through 17R-CC, and rare *Neogloboquadrina atlantica* (sinistrally coiling) are observed in Samples 162-986D-34R-CC through 38R-CC, and 43R-CC through 48R-CC. Most specimens are well preserved and show no signs of being reworked. These occurrences provide limited age control for the sequence (see "Sedimentation Rates" section, this chapter). Neither the start of the acme zone of *N. pachyderma* (sinistrally coiling), nor the last occurrence (LO) of *N. atlantica* (sinistrally coiling) are well defined, because of barren samples and poor core recovery from Samples 162-986D-18R-CC to 33R-CC (Fig. 14). Significantly however, the *N. atlantica* (sinistrally coiling) Zone below ~707 mbsf suggests an age >2.4 Ma for the lower part of the sequence. Subpolar to polar paleoenvironmental conditions are indicated throughout.

### Benthic Foraminifers

Benthic foraminifers are generally rare at Site 986, with the exception of the mudline samples (162-986A-1H-1, 0–1 cm, and 162-986C-1H-1, 0–1 cm), which contain a diverse assemblage dominated by *Cassidulina reniforme, Cibicidoides wuellerstorfi, Epistominella* cf. *exigua, Reophax* sp., and other agglutinated species. Preservation and abundance vary greatly downhole. The most common taxa are *Cassidulina teretis, Elphidium asklundi, Elphidium excavatum,* and *Cibicidoides* spp. The last occurrence of abraded and broken specimens of *Cibicides grossus* are recorded in Sample 162-986C-26X-CC. However, this last occurrence is not considered a reliable indicator of Pliocene age given that upper slope and shelf species such as *Elphidium excavatum* appear to coincide with it, suggesting sediment reworking and downslope transport. Rare and highly deformed agglutinated benthic foraminifers were observed in the following samples: 162-986D-16R-CC, 17R-CC, 47R-CC, 48R-CC, and 57R-CC.

### Diatoms

With the exception of Sample 162-986A-7H-CC, all samples at this site are barren of diatoms. Sample 162-986A-7H-CC contains an assemblage dominated by non-age-diagnostic species of *Melosira, Rhaphoneis,* and *Navicula.* However, the occurrence of *Rhizosolenia curvirostris* suggests this sample has an age greater than 0.3 Ma.

### Siliceous Flagellates

Only Samples 162-986A-7H-CC and 8H-CC contained biosiliceous particles, including skeletons of *Actiniscus pentasterias.* The abundance of *A. pentasterias* is low and the preservation is moderate. No age information can be given from the occurrence of this species.

### Radiolarians

To obtain age data, Sample 162-986A-7H-CC was processed for radiolarians. The radiolarian assemblage contains only a few species which are poorly preserved. Most abundant is *Cromechinus borealis,* probably because of its heavily silicified skeleton. No age information can be given from the composition of the assemblage.

## PALEOMAGNETISM

At Site 986, archive halves of all cores that were not highly deformed were measured using the pass-through cryogenic magnetometer with a 5-cm measurement interval. Ubiquitous core deformation was exacerbated by entrained clasts and dropstones. In addition, long intervals of poor or negligible recovery compromised the continuity of the records.

Demagnetization was carried out at peak alternating fields of 25 mT for all core sections. The natural remanent magnetization (NRM) of some cores was measured in order to establish the direction of the viscous drill-string overprint. Additional demagnetization steps at 15 and 30 mT were carried out on some core sections, as time allowed (Table 6). The ubiquitous drilling-induced remanence is steeply inclined downward. At Site 986, the paleomagnetic inclination data are highly scattered and generally incoherent, apart from the 700–900-mbsf interval at the base of Hole 986D.

In Hole 986A, the inclinations are generally positive but highly scattered, particularly in the 86–106-mbsf interval. Core 986A-23X has predominantly negative inclinations after demagnetization at 25 mT; however, the next core (986A-24X) is the final core in this hole and has predominantly normal inclinations. We therefore have no basis for placing the Brunhes/Matuyama boundary in this hole.

At Hole 986C, the inclination record is very discontinuous due to the combination of poor recovery and core deformation. The magnetic stratigraphy cannot be resolved.

At Hole 986D, most of the RCB cores are highly deformed and recovery is very discontinuous. From 700 mbsf to the base of the hole (964 mbsf), the sediments are sufficiently lithified that some cores withstood the ravages of rotary coring. Core 986D-35R (714–724 mbsf) is at the top of this interval of improved core recovery and core

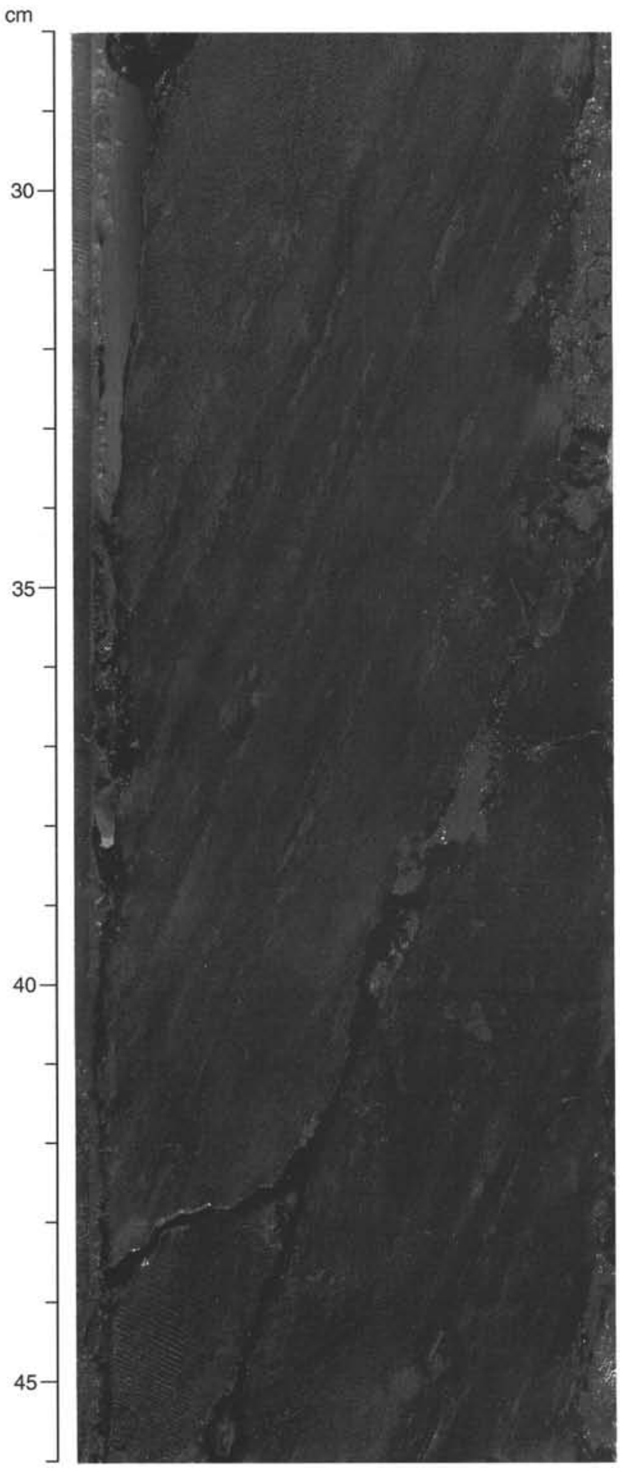


Figure 11. Photograph showing beds dipping at high angle (about 70°) found in the lower part of Unit III in Section 162-986D-29R-2, 28–46 cm (658.68–658.86 mbsf).

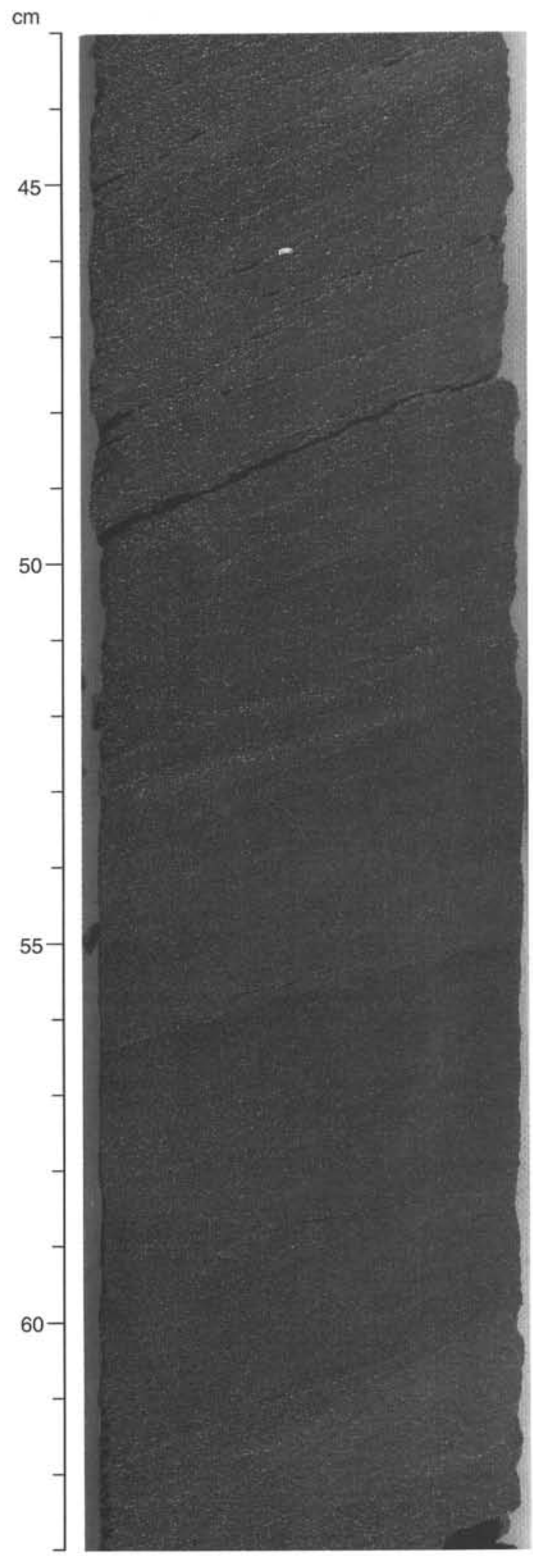


Figure 12. Photograph showing beds dipping at low angle (about 10°) found in Subunit IVA in Section 162-986D-49R-1, 43–63 cm (845.63–845.83 mbsf).

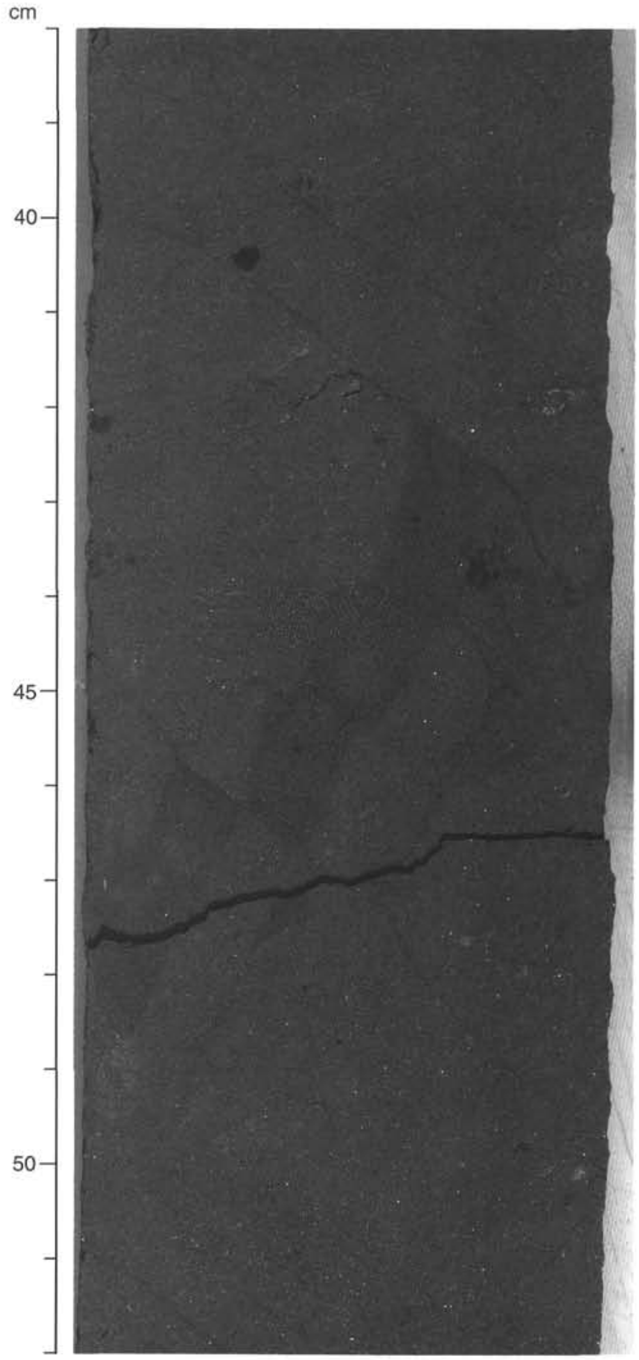


Figure 13. Photograph showing multiple mud-filled veins found in Section 162-986D-52R-3, 38–52 cm (877.48–877.62 mbsf).

integrity. The NRM inclinations (prior to demagnetization) are positive, indicating the orientation of the viscous magnetization imposed by the drill string (Fig. 15). On demagnetization, the inclinations of magnetization become negative throughout most of the 700–950-mbsf interval, with an interval of positive inclinations in the 735–756-mbsf interval (Fig. 15).

The inclination data from the 700–950-mbsf interval in Hole 986D indicate that the sediments were deposited during a reversed-polarity chron. As the top of the Gilbert Chron is at 3.58 Ma, and biostratigraphic data (see "Biostratigraphy" section, this chapter) indicate an age for the base of Hole 986D of less than 3.6 Ma, this reversed-polarity chron should be the Matuyama Chron. This implies an age of less than 2.6 Ma for the base of Hole 986D.

## SEDIMENTATION RATES

A sedimentary section 956 m thick was recovered at Site 986. Sedimentation rate estimates for Site 986 are based solely on biostratigraphic information from Holes 986A, 986C, and 986D (Table 7; Fig. 16). However, since biostratigraphic datums could not be located precisely because of numerous barren intervals, age control is limited (see "Biostratigraphy" section, this chapter). Paleomagnetic data were unreliable in the XCB- and RCB-cored intervals of Site 986, except for a few intervals, including a thick interval of dominantly reversed polarity from ~720 mbsf to the base of the hole (see "Paleomagnetism" section, this chapter). This was originally correlated to the Matuyama Chron, but the presence of the *Neogloboquadrina atlantica* (sinistrally coiling) planktonic foraminifer zone indicates an older age for this interval. Our decision to use only the biostratigraphic information for age control assumes the microfossil marker species are not reworked (see "Biostratigraphy" section, this chapter).

The Site 986 composite depth section (see "Composite Depths" section, this chapter) was used to relate events recorded in Holes 986A and 986C to a common depth scale. Sedimentation rates are calculated for both the meters below seafloor (mbsf) depth scale and the meters composite depth (mcd) depth scale. Table 7 and Figure 17 present minimum and maximum sedimentation rates as a function of age and composite depth for Site 986. Rates for this site are the highest observed on Leg 162. Sedimentation rates are less than ~273 mcd/m.y. from 0 to 0.46 Ma, greater than ~314 mcd/m.y. from 0.46 to 1.8 Ma and less than ~264 mcd/m.y. below 1.8 Ma. Below 2.4 Ma, rates must be greater than ~160 mcd/m.y.

## ORGANIC GEOCHEMISTRY

The shipboard organic geochemistry program at Site 986 consisted of analyses of volatile hydrocarbons, determinations of inorganic carbon, total nitrogen, total carbon, and total sulfur, and pyrolysis measurements (for methods, see "Explanatory Notes" chapter, this volume).

### Volatile Hydrocarbons

As part of the shipboard safety and pollution monitoring program, concentrations of methane ($C_1$), ethane ($C_2$), and propane ($C_3$) gases were measured in every core using standard ODP headspace and vacutainer sampling techniques. These routine measurements were performed on the Hewlett Packard 5980 Series II gas chromatograph. Due to the occurrence of significant amounts of higher-molecular-weight gases ($C_{2+}$) in the lower part of the sedimentary sequence at Site 986, monitoring of the hydrocarbon gases methane through hexane ($C_6$) was performed using the natural gas analyzer (NGA).

Except for the uppermost 20 mbsf, concentrations of headspace methane are high throughout the sedimentary section, varying between about 5000 and 58,000 ppm (Table 8; Fig. 18). No distinct long-term change is obvious; however, minima in methane concentrations (~600–4000 ppm) occur between 840 and 870 mbsf. These minima are paralleled by minima in ethane and propane (Fig. 18). According to the pressure-temperature stability field of gas hydrates (cf. Kvenvolden and Barnard, 1983), and assuming a geothermal temperature gradient of about 152°C/km (see "Physical Properties" section, this chapter), a water depth of 2063 m, and a bottom-water

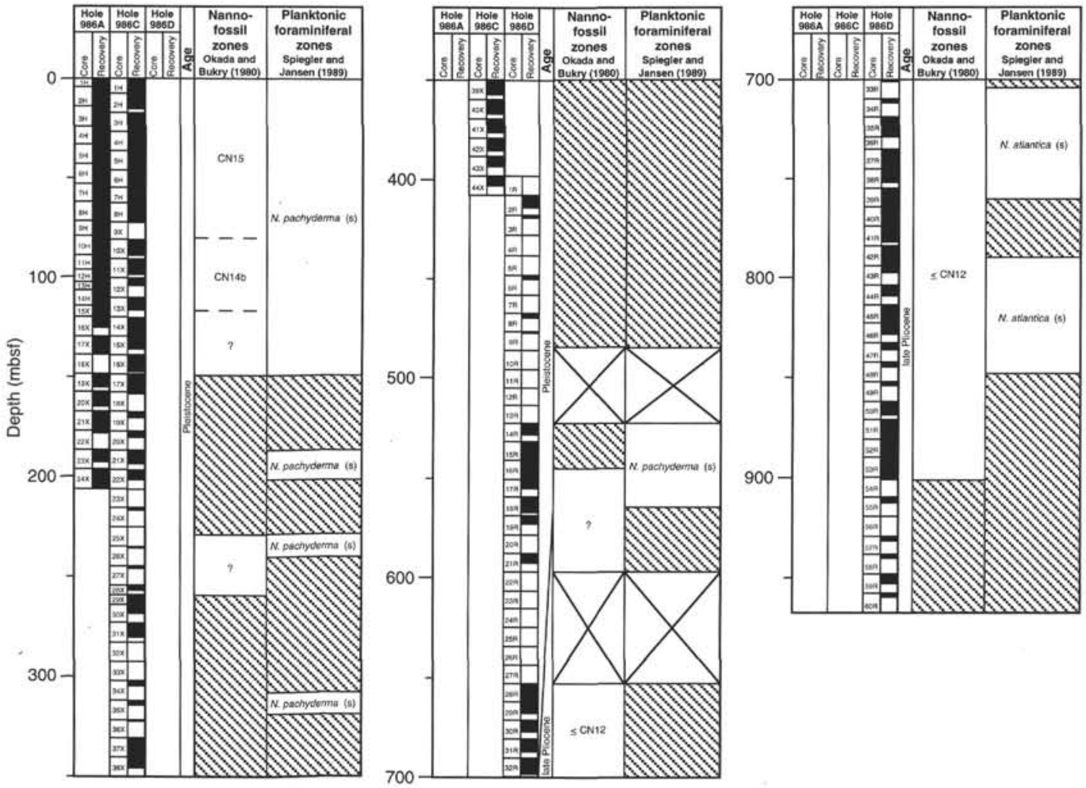


Figure 14. Biostratigraphic summary, Site 986. Hatched intervals indicate absence of fossils. An "X" indicates interval with no recovery. Diagonal line in "Age" column indicates uncertainty in placement of the Pliocene/Pleistocene boundary. Boundary is based on planktonic foraminifer biostratigraphy.

temperature of –0.95°C (see "Physical Properties" section, this chapter), gas hydrates should be stable down to about 150 mbsf at Site 986. (Fig. 18). Therefore, the high concentration of methane between 20 and 150 mbsf may possibly be related to the presence of methane hydrates. This estimated depth of hydrate zone corresponds to the occurrence of gas voids in recovered cores, which suggests degassing sediments in the core liner. However, no obvious gas hydrates were observed at Site 986. Ethane started to be detected below 20 mbsf, and generally increased with burial depth at Site 986 (Fig. 18). Propane was first detected below 100 mbsf, having low levels in the upper 455 mbsf (<10 ppm) and increasing from 515 mbsf to the bottom of Hole 986D (Fig. 18). Ethylene ($C_{2=}$) occurs in detectable amounts from 100 to 135 mbsf and from 374 to 543 mbsf (Table 8). Propylene ($C_{3=}$) was detected from 436 to 538 mbsf (Table 8).

The vacutainer gas concentrations are generally higher than the headspace concentrations; however, they show similar trends (Table 9; Fig. 18). The difference between headspace and vacutainer data, which decrease from methane through ethane to propane (Fig. 18), might be explained by the different sampling techniques, causing a loss of the more mobile methane before sealing the headspace sediment sample in the glass vial (Stein et al., 1995).

Below 543 mbsf, higher-molecular-weight hydrocarbons occurred in detectable amounts: iso-butane ($IC_4$), *n*-butane ($NC_4$), and iso-pentane ($IC_5$) first occurred at 543 mbsf (Core 162-986D-17R), *n*-pentane ($NC_5$) first occurred at 557 mbsf (Core 162-986D-18R), and iso-hexane ($IC_6$) and *n*-hexane ($NC_6$) first occurred below 652 mbsf (Core 162-986D-28R; Table 8; Fig. 18).

## Hydrocarbon Formation, Source Rock Potential, and Safety Considerations

For safety considerations, the $C_1/C_2$ (methane/ethane) ratio is generally used to get quick information about the origin of the hydrocarbons. At Site 986, the headspace $C_1/C_2$ ratios show the normal general decrease with depth and temperature, from values of >10,000 in shallow depth to values of about 50 at the bottom of Hole 986D (Table 8; Fig. 18). The vacutainer data, although based on limited data points, show a parallel trend with headspace $C_1/C_2$ ratios. High $C_1/C_2$ ratios above 100 mbsf suggest in situ microbial production of methane from marine organic material, which is present in major amounts throughout the entire sedimentary sequence. At Site 986, methanogenesis has begun at depths shallower than 20 mbsf, as clearly indicated by the sharp increase in methane concentrations and the contemporaneous and sharp disappearance of sulfate (see "Inorganic Geochemistry" section, this chapter).

The first occurrence of heavier hydrocarbons (such as hexane at about 650 mbsf or 98°C) indicate the beginning of detectable thermogenic hydrocarbon formation increasing further downhole. When temperature increased above 90°C, the occurrence of $C_5$–$C_6$ hydrocarbons and their smooth increase with depth is expected and has been reported at other ODP sites (e.g., Site 909; Myhre, Thiede, Firth, et al., 1995) where drilling was continued without incident. Thus, at Site 986 drilling was continued below 650 mbsf despite the occurrence of heavier hydrocarbons.

Rock-Eval data are summarized in Table 10 and displayed in Figure 19. $S_1$ values, a measure of the quantity of free hydrocarbons (i.e., gas and/or oil) in the sediment, were generally low throughout at Site 986 (Fig. 19). $S_2$ values, an indicator for the quantity of hydrocarbons that could be produced in these sediments by cracking of kerogen, increased with burial depth (Fig. 19). The $S_2/S_3$ ratio, which is a means of determining the type of organic matter, shows low values (<2.5) throughout (Fig. 19). The hydrogen index/oxygen index ("van Krevelen-type") diagram gives important information about the chemical characteristics of organic matter in sediments, as well as about the origin of organic matter, maturity, and type of hydrocarbon produced (e.g., Peters, 1986; Fig. 20). These two parameters suggest that the organic matter in the sediment sequence at Site 986 is characterized by gas-prone kerogen Type III (terrestrial origin and lignin-rich). The conclusions about migration and/or in situ formation of hydrocarbons should be supported by other more precise geochemical methods, such as vitrinite reflectance, gas chromatography studies, and isotopic measurement of methane.

### Carbon, Nitrogen, and Sulfur Concentrations

Determinations of inorganic carbon, total carbon, total nitrogen, and total sulfur are summarized in Table 11 and presented in Figure 21. Carbonate content values in the dominant lithologies (i.e., clayey silt, silty clay, and sandy silt) vary between 0.7% and 10% in the sedimentary sequence at Site 986. In the light-colored layers and other rare intervals, carbonate contents reach values as high as 20% to 40% (Fig. 21). Total organic carbon (TOC) content varies between 0.18% and 1.88% (Table 11; Fig. 21). Based on the TOC data, the sedimentary sequence of Site 986 can be divided into four intervals. The upper 215 mbsf (late Quaternary in age) is characterized by high amplitude variations in TOC contents between 0.18% and 1.88%. Between 215 and 655 mbsf (early Pleistocene to late Pliocene), TOC values are slightly higher, ranging from 0.45% to 1.87%. In the interval from 655 to 900 mbsf, the TOC content varies mostly between 0.5% and 0.8%. The lowermost interval of the sedimentary sequence in Hole 986D (900–955 mbsf) is characterized by a short distinct increase in TOC content ranging from 0.82% to 1.22% (Fig. 21). Total nitrogen content ranges from 0.01% to 0.17%, with an average value of 0.10% (Fig. 21). Most of the total sulfur values vary between 0% and 1.0% (Fig. 21). A single peak of high sulfur content of 2.16% occurs in the upper part at Site 986. In the lowermost interval (900 to 955 mbsf), total sulfur values are very high, ranging from 0.75% to 2.66% (Fig. 21), probably reflecting disseminated pyrite and pyrite nodules (see "Lithostratigraphy" section, this chapter). These high total organic carbon and total sulfur values may suggest that the environment of deposition was oxygen-depleted anoxic, due to increased productivity and/or restricted deep-water ventilation when the lowermost interval at Site 986 was deposited.

### Composition of Organic Matter

Total organic carbon/total nitrogen (C/N) ratios and hydrogen index (HI) values from Rock-Eval pyrolysis have been used to characterize the type of the organic matter. C/N ratios vary between 2.6 and 18.3 at Site 986, and most values range from 5 to 10 (Fig. 21), suggesting that major amounts of marine organic matter are preserved in the sediments (Fig. 22). C/N ratios of >10 occur in the uppermost section, above 90 mbsf (late Quaternary), which corresponds to lithostratigraphic Unit I (see "Lithostratigraphy" section, this chapter), and from 705 to 750 mbsf (latest Pliocene?), probably reflecting the presence of small amounts of terrigenous organic material (see above). The limited amount of Rock-Eval data does not support the C/N results in general. Hydrogen index (HI) values, which is a parameter used to characterize organic matter origin, are generally low (20 to 100 mg HC/g C; Table 10; Fig. 19). These data suggest the presence of a high proportion of terrigenous organic material in the sediments at Site 986. Two high HI values occur in the Samples 162-986C-43X-3, 94–95 cm (392.64 mbsf; 173 mg HC/g TOC), and 60R-1, 67–68 cm (955.67 mbsf; 154 mg HC/g TOC), and indicate that increased amounts of marine organic matter were preserved at these intervals. These first rough estimates of the composition of the organic matter, however, have to be checked by more detailed shore-based organic geochemical investigations.

## INORGANIC GEOCHEMISTRY

Site 986 is characterized by extremely high sedimentation rates (as high as 316 m/m.y.) and by very high heat flow (152°C/km) mea-

**Table 6. Summary of pass-through cryogenic magnetometer measurements at Site 986.**

| Measurement | Core sections |
|---|---|
| | 162-986A- |
| NRM | 1H-1 |
| 25 mT | 1H-1 through 23X-4, 24X-1, 24X-5 |
| 30 mT | 8H-5, 11H-4 |
| 25 mT | 986B-1H-1 through 2H-6 |
| | 162-986C- |
| 25 mT | 1H-1 through 22X-3, 24X-1, 26X-1, 28X-2, 29X-1 through 30X-3, 31X-1 through 34X-2, 37X-2 through 38X-4, 39X-1, 39X-3, 40X-2 through 41X-5 |
| 30 mT | 6H-2, 11X-3, 26X-1, 30X-3 |
| | 162-986D- |
| NRM | 19R-2, 19R-3, 21R-1, 35R-2 through 35R-7, 37R-1 through 37R-6, 38R-3, 39R-5 through 42R-4, 42R-6, 43R-2, 44R-2, 44R-3, 44R-4, 45R-1, 46R-1, 47R-1, 48R-1, 49R-1, 50R-2 through 53R-5, 57R-1, 59R-1 through 60R-1 |
| 15 mT | 53R-2, 53R-4, 53R-5 |
| 25 mT | 2R-1 through 2R-4, 6R-1, 8R-1, 14R-2 through 19R-3, 21R-1, 21R-2, 21R-3, 28R-2, 29R-1 through 31R-4, 33R-1, 34R-1, 35R-1 through 35R-7, 37R-1 through 42R-6, 43R-2, 44R-2 through 46R-3, 47R-1, 48R-1, 49R-1, 50R-2 through 53R-5, 57R-1, 59R-1 through 60R-1 |
| 30 mT | 15R-6, 18R-5, 21R-2, 21R-3, 29R-2, 39R-4, 39R-5, 40R-2, 53R-2, 53R-3, 53R-4 |

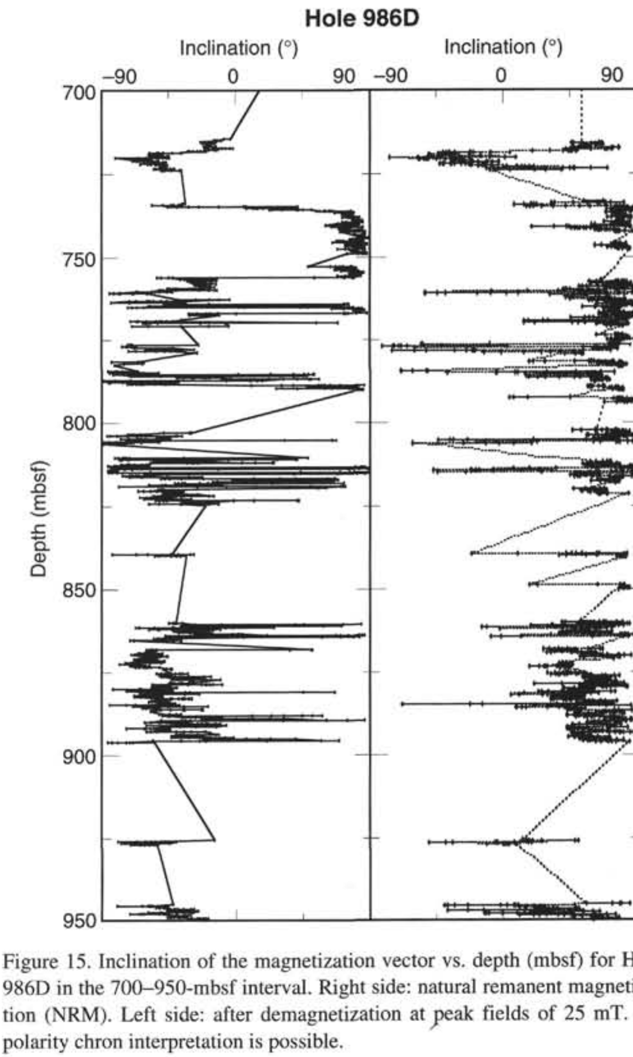


Figure 15. Inclination of the magnetization vector vs. depth (mbsf) for Hole 986D in the 700–950-mbsf interval. Right side: natural remanent magnetization (NRM). Left side: after demagnetization at peak fields of 25 mT. No polarity chron interpretation is possible.

**Table 7. Age control points, Site 986.**

| Biostratigraphic datums | Age (Ma) | Hole | Depth (mbsf) | Depth (mcd) | Rate (mbsf/m.y.) | Rate (mcd/m.y.) |
|---|---|---|---|---|---|---|
| Top of section | 0.00 | | 0.00 | 0.00 | | |
| | | | | | <260.50 | <273.54 |
| LO *P. lacunosa* (N) | 0.46 | 986A | <119.83 | <125.83 | | |
| | | | | | >318.04 | >313.56 |
| S, acme *N. pachyderma* s. (F) | 1.80 | 986D | >546.00 | >546.00 | | |
| | | | | | <263.93 | <263.93 |
| LO *N. atlantica* (F) | 2.41 | 986D | <707.00 | <707.00 | | |
| | | | | | >160.50 | >160.50 |
| FO *P. lacunosa* (N) | 3.60 | 986D | >898.00 | >898.00 | | |

Notes: Ages are from Berggren et al. (1995). N = calcareous nannofossil; F = foraminifer.

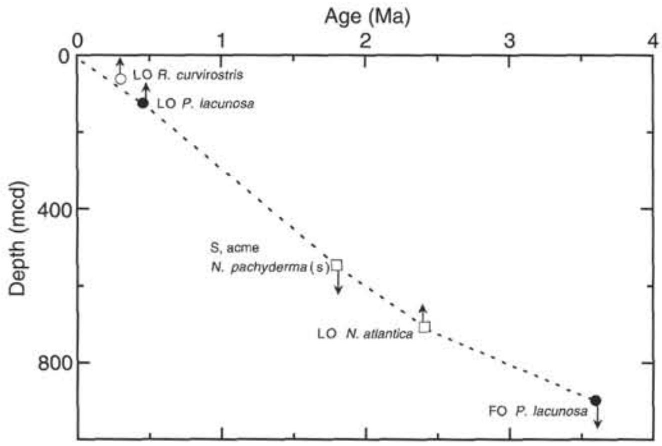


Figure 16. Site 986 age vs. depth (mcd) curve based on biostratigraphic datums. Solid circles = nannofossils; open circle = diatom; open squares = foraminifers.

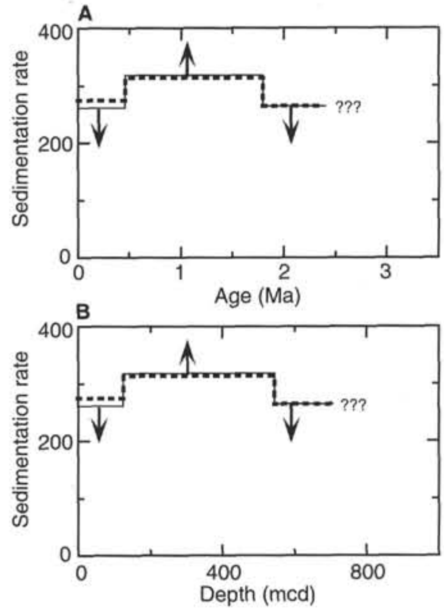


Figure 17. Site 986 sedimentation rates vs. age (**A**) and vs. composite depth (**B**). Solid lines indicate rates in mbsf/m.y.; dashed lines indicate rates in mcd/m.y.

sured in the uppermost 62 m. Interstitial water samples were collected in Hole 986C from the surface to approximately 400 mbsf, and in Hole 986D from about 435 mbsf to the base of the hole. The interstitial water profiles at this site are controlled by three dominant processes: (1) sulfate reduction and methanogenesis, (2) alteration of volcanic matter in the sediments and interaction with basement, and (3) breakdown and dehydration of clay minerals under conditions of high heat flow. The outstanding features of the interstitial water profiles include (1) sharp changes in the upper 20 mbsf related to the shallow zone of sulfate reduction and methanogenesis, and (2) large decreases in chloride, sodium, and salinity, and an increase in alkalinity below 400 mbsf related to the thermal transformation of smectite to illite.

Sulfate is rapidly consumed in the top 20 m of Site 986 (Table 12; Fig. 23A), and the transition to methanogenesis is recorded by the abrupt increase in methane in headspace samples across this interval (see "Organic Geochemistry" section, this chapter). Sulfate concentrations remain very low until about 550 mbsf, where they increase slightly, suggesting a source of sulfate to the pore waters. As a result of both sulfate reduction and methanogenesis, ammonia increases downhole from 87 μM near the surface to a maximum of 5084 μM at 267 mbsf (Table 12; Fig. 23B). Ammonia concentrations remain high to the base of Hole 986D, but show a slight decrease below 270 mbsf.

Alkalinity exhibits anomalous behavior such that two peaks are apparent at 23 and 740 mbsf (Table 12; Fig. 23C). The upper peak reflects bicarbonate released during rapid sulfate reduction and the lower peak is probably related to clay mineral transformations under conditions of high heat flow (see discussion below). Alkalinity measurements were not made below 740 mbsf because of the small volume of interstitial water obtained from squeezing sediments below this level. Phosphate concentrations also show a sharp peak at 23 mbsf (Table 12; Fig. 23D), probably reflecting the rapid release of phosphate from organic matter in the zone of sulfate reduction.

Magnesium concentrations progressively decrease downhole from near seawater values at the top (50.4 mM) to a minimum of about 5 mM near the bottom of the hole (Table 12; Fig. 23E). Calcium concentrations generally increase downhole at Site 986, except for the top 20 mbsf when calcium values decrease slightly (Table 12; Fig. 23E). As a result, the slope of $\Delta Ca/\Delta Mg$ is positive above 20 mbsf and negative below (Fig. 23F). Calcium decreases in the upper 20 mbsf, which is most likely due to calcite precipitation in the zone of sulfate reduction. Below this level, calcium increases and magnesium decreases downhole due to the alteration of volcanic material in the sediment and interaction with oceanic basement below.

The profile of dissolved potassium decreases rapidly from near seawater values at the surface (11.6 mM) to about 2 mM at 400 mbsf (Table 12; Fig. 23G). Below this level, potassium concentrations continue to decline, but at a slower rate, reaching minimum values of 1.3 mM near the bottom of Hole 986D. The downhole decrease in potassium reflects uptake during the alteration of oceanic basement and volcanic material in the sediment. Lithium generally increases downhole except for a small decrease in the upper 20 mbsf and an interval of near constant values between 450 and 600 mbsf (Table 12; Fig. 23H). The decrease in the upper 20 mbsf may reflect removal of lith-

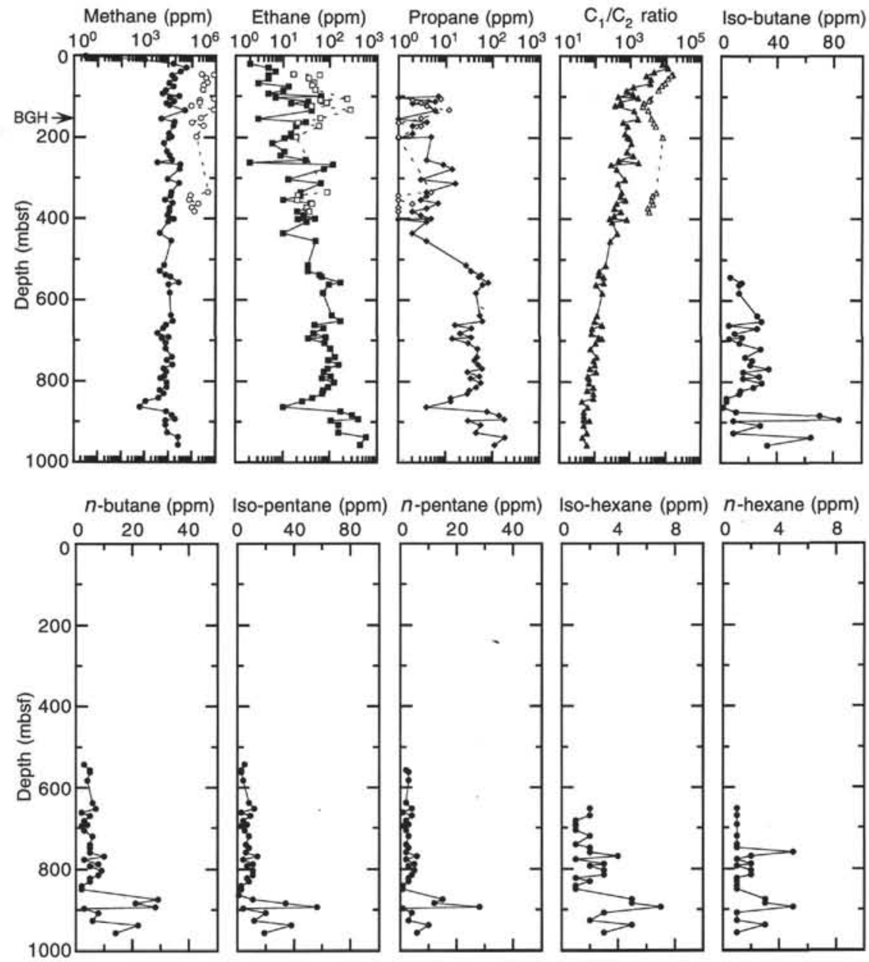


Figure 18. Profiles of headspace and vacutainer methane ($C_1$), ethane ($C_2$), and propane ($C_3$) concentrations, $C_1/C_2$ ratio, and concentrations of higher-molecular-weight hydrocarbons at Site 986. Solid symbols = headspace data; open symbols = vacutainer data. "BGH" on methane plot indicates the base of gas hydrate at Site 986, which is estimated based on the pressure-temperature stability field of gas hydrates (cf. Kvenvolden and Barnard, 1983).

ium during authigenic carbonate precipitation. Below 20 mbsf, the increase in lithium is due to alteration of volcanic material in the sediments and/or oceanic basement below.

The profiles of dissolved chloride and sodium show pronounced decreases downhole at Site 986 (Table 12; Fig. 23I). We suggest that two processes control the behavior of these elements: (1) decomposition of methane hydrates in the upper part of the hole, and (2) breakdown and dehydration of smectite to illite below 400 mbsf, which is driven by the high geothermal gradient at this site. Chloride and sodium concentrations are near seawater values at the top of Hole 986C (557 and 476 mM, respectively) and decrease to minimum values of 540 and 448 mM, respectively, at about 150 mbsf. We suggest this decrease is due to the decomposition of methane hydrates as the sediments are buried below the hydrate stability zone and as the cores are brought to the surface and heated. On the basis of a geothermal gradient of 152°C/km, methane hydrates are predicted to be stable at Site 986 between the surface and about 150 mbsf (see "Organic Geochemistry" section, this chapter). As hydrates are buried below this depth, they would decompose, resulting in the decreasing chloride and sodium concentrations observed in the upper part of Hole 986C.

The greatest changes in chloride and sodium occur below 400 mbsf, and represent a 30% to 40% dilution of seawater (Fig. 23I, -J). These decreases cannot be explained by clathrate decomposition because they occur far below the field of hydrate stability. We suggest this decrease is due to the transformation of smectite to illite, which is accompanied by the release of water (Kastner et al., 1993, and references therein). Empirical studies suggest that the optimal temperature range for initiation and completion of this reaction is from 60° to 150°C for young sedimentary systems (<2 Ma) and from 60° to 120°C for old sedimentary systems (>5 to 10 Ma) (Kastner et al., 1993, and references therein). Since the age of crust at Site 986 is intermediate between these end-members, we assume the transformation of smectite to illite should begin at 60°C and be completed by about 135°C. By extrapolation of the geothermal gradient measured in the upper 62 mbsf of Hole 986C (see "Physical Properties" section, this chapter), we predict these isotherms should occur between about 400 and 900 m. This interval coincides remarkably well with the downhole decrease in chloride, sodium, and salinity (Fig. 24). The ratio of Na/Cl increases below 400 mbsf because the decrease in chloride is greater than the decrease in sodium (Fig. 23K). This suggests a source of sodium to the pore waters, because dilution alone would decrease sodium and chloride equally. A plausible explanation for this observation is transformation of a Na-bearing smectite to Na-free illite, releasing dissolved sodium to pore waters. Shore-based XRD studies should be able to confirm or refute this hypothesis.

The profile of salinity is similar to chloride and sodium in the lower part of the hole, but subtle differences exist near the top (Table 12; Fig. 23L). For example, the rapid decrease from 34 to 32 in the top 20 mbsf is not mirrored in the chloride and sodium profiles, and reflects the loss of sulfate in the zone of sulfate reduction. The reduction in salinity from 34 at the top to a minimum of 23 below 400 mbsf represents a 32% dilution of seawater.

The pH of interstitial waters generally increases downhole from values of 7.8 near the top to a maximum of 8.5 below 400 mbsf (Table 12; Fig. 23M). Silica concentrations are low and show a decreasing trend from the top of the hole to a minimum near 440 mbsf (Table

**Table 8. Results of headspace gas analyses of Hole 986A, 986C, and 986D samples.**

| Core, section, interval (cm) | Depth (mbsf) | Sed. T (°C) | $C_1$ (ppm) | $C_{2=}$ (ppm) | $C_2$ (ppm) | $C_{3=}$ (ppm) | $C_3$ (ppm) | $IC_4$ (ppm) | $NC_4$ (ppm) | $IC_5$ (ppm) | $NC_5$ (ppm) | $IC_6$ (ppm) | $NC_6$ (ppm) | $C_1/C_2$ | $C_1/C_3$ | $C_1/C_{2+}$ |
|---|---|---|---|---|---|---|---|---|---|---|---|---|---|---|---|---|
| 162-986A- | | | | | | | | | | | | | | | | |
| 1H-2, 0–5 | 1.53 | –0.7 | 3 | | | | | | | | | | | | | |
| 2H-5, 0–5 | 10.63 | 0.7 | 955 | | | | | | | | | | | | | |
| 3H-5, 0–5 | 20.13 | 2.1 | 16,230 | | 2 | | | | | | | | | 8,115 | | 8,115 |
| 4H-5, 0–5 | 29.63 | 3.6 | 57,852 | | 5 | | | | | | | | | 11,570 | | 11,570 |
| 5H-5, 0–5 | 39.13 | 5.0 | 32,781 | | 7 | | | | | | | | | 4,683 | | 4,683 |
| 6H-5, 0–5 | 48.53 | 6.4 | 14,031 | | 5 | | | | | | | | | 2,806 | | 2,806 |
| 7H-5, 0–5 | 57.19 | 7.7 | 18,583 | | 5 | | | | | | | | | 3,717 | | 3,717 |
| 8H-5, 0–5 | 67.58 | 9.3 | 10,683 | | 3 | | | | | | | | | 3,561 | | 3,561 |
| 9H-4, 0–5 | 75.63 | 10.5 | 15,868 | | 13 | | | | | | | | | 1,221 | | 1,221 |
| 10H-5, 0–5 | 84.56 | 11.9 | 7,631 | | 10 | | | | | | | | | 763 | | 763 |
| 11H-4, 0–5 | 92.63 | 13.1 | 5,739 | | 5 | | | | | | | | | 1,148 | | 1,148 |
| 12H-4, 0–5 | 100.13 | 14.3 | 29,012 | 0.4 | 65 | | 7 | | | | | | | 446 | 4,145 | 401 |
| 13H-2, 0–5 | 103.13 | 14.7 | 11,469 | 0.2 | 7 | | 1 | | | | | | | 1,638 | 11,469 | 1,399 |
| 14H-5, 0–5 | 111.63 | 16.0 | 18,051 | | 34 | | 6 | | | | | | | 531 | 3,009 | 451 |
| 15X-3, 0–5 | 116.93 | 16.8 | 8,427 | 0.2 | 15 | | 2 | | | | | | | 562 | 4,214 | 490 |
| 16X-3, 0–5 | 122.33 | 17.6 | 11,394 | | 32 | | 4 | | | | | | | 356 | 2,849 | 317 |
| 17X-5, 0–5 | 134.93 | 19.5 | 49,887 | 0.2 | 40 | | 6 | | | | | | | 1,247 | 8,315 | 1,080 |
| 19X-5, 0–5 | 154.13 | 22.5 | 4,944 | | 3 | | 1 | | | | | | | 1,648 | 4,944 | 1,236 |
| 20X-4, 0–5 | 162.33 | 23.7 | 18,829 | | 30 | | 4 | | | | | | | 628 | 4,707 | 554 |
| 21X-5, 0–5 | 172.05 | 25.2 | 15,958 | | 19 | | 2 | | | | | | | 840 | 7,979 | 760 |
| 23X-4, 0–5 | 191.33 | 28.1 | 10,557 | | 15 | | 2 | | | | | | | 704 | 5,279 | 621 |
| 24X-5, 0–5 | 202.43 | 29.8 | 10,333 | | 11 | | 1 | | | | | | | 939 | 10,333 | 861 |
| 162-986C- | | | | | | | | | | | | | | | | |
| 22X-3, 0–5 | 199.33 | 29.3 | 13,475 | | 16 | | 5 | | | | | | | 842 | 2,695 | 642 |
| 24X-1, 0–5 | 215.53 | 31.8 | 6,468 | | 6 | | | | | | | | | 1,078 | | 1,078 |
| 26X-1, 0–5 | 234.73 | 34.7 | 8,944 | | 11 | | | | | | | | | 813 | | 813 |
| 27X-1, 0–5 | 244.33 | 36.2 | 11,046 | | 9 | | | | | | | | | 1,227 | | 1,227 |
| 28X-2, 0–5 | 255.53 | 37.9 | 13,928 | | 30 | | 4 | | | | | | | 464 | 3,482 | 410 |
| 29X-3, 0–5 | 262.03 | 38.9 | 3,344 | | 2 | | | | | | | | | 1,672 | | 1,672 |
| 30X-3, 0–5 | 266.63 | 39.6 | 33,707 | | 117 | | 9 | | | | | | | 288 | 3,745 | 268 |
| 31X-4, 0–5 | 277.73 | 41.2 | 30,445 | | 74 | | 14 | | | | | | | 411 | 2,175 | 346 |
| 34X-2, 0–5 | 303.63 | 45.2 | 9,285 | | 13 | | 3 | | | | | | | 714 | 3,095 | 580 |
| 35X-2, 0–5 | 313.23 | 46.6 | 28,546 | | 64 | | 16 | | | | | | | 446 | 1,784 | 357 |
| 37X-4, 0–5 | 334.32 | 49.8 | 13,708 | | 24 | | 4 | | | | | | | 571 | 3,427 | 490 |
| 38X-3, 0–5 | 343.63 | 51.2 | 12,704 | | 24 | | 4 | | | | | | | 529 | 3,176 | 454 |
| 39X-3, 0–5 | 353.23 | 52.7 | 7,397 | | 10 | | 3 | | | | | | | 740 | 2,466 | 569 |
| 40X-2, 0–5 | 361.33 | 53.9 | 15,789 | | 39 | | 7 | | | | | | | 405 | 2,256 | 343 |
| 41X-4, 0–5 | 373.93 | 55.8 | 11,175 | 0.7 | 32 | | 4 | | | | | | | 349 | 2,794 | 304 |
| 42X-3, 0–5 | 382.13 | 57.1 | 10,985 | 0.5 | 20 | | 2 | | | | | | | 549 | 5,493 | 488 |
| 43X-3, 0–5 | 391.73 | 58.6 | 9,608 | 0.7 | 28 | | 3 | | | | | | | 343 | 3,203 | 303 |
| 44X-2, 0–5 | 399.83 | 59.8 | 12,265 | 0.5 | 48 | | 5 | | | | | | | 256 | 2,453 | 229 |
| 162-986D- | | | | | | | | | | | | | | | | |
| 2R-3, 0–5 | 400.43 | 59.9 | 16,930 | | 21 | | 1 | | | | | | | 806 | 16,930 | 770 |
| 3R-1, 0–5 | 407.13 | 60.9 | 9,730 | | 32 | | 4 | | | | | | | 304 | 2,433 | 270 |
| 6R-1, 0–5 | 435.93 | 65.3 | 4,357 | 2 | 10 | 2 | 2 | | | | | | | 436 | 2,179 | 272 |
| 8R-1, 0–5 | 455.13 | 68.2 | 13,546 | | 50 | | 4 | | | | | | | 271 | 3,387 | 251 |
| 14R-3, 0–5 | 515.73 | 77.4 | 6,895 | 0.5 | 34 | 0.2 | 28 | | | | | | | 203 | 246 | 110 |
| 15R-5, 0–5 | 528.33 | 79.3 | 4,529 | 0.4 | 34 | | 35 | | | | | | | 133 | 129 | 65 |
| 16R-5, 0–5 | 537.93 | 80.8 | 7,653 | 0.5 | 60 | 0.2 | 58 | | | | | | | 128 | 132 | 64 |
| 17R-2, 0–5 | 543.03 | 81.5 | 12,400 | 0.3 | 69 | | 51 | 7 | 3 | 5 | | | | 180 | 243 | 92 |
| 18R-5, 0–5 | 557.13 | 83.7 | 29,242 | | 167 | | 82 | 15 | 5 | 3 | 2 | | | 175 | 357 | 107 |
| 19R-2, 0–5 | 562.23 | 84.5 | 10,796 | | 98 | | 63 | 13 | 5 | 3 | 3 | | | 110 | 171 | 58 |
| 21R-3, 0–5 | 583.03 | 87.6 | 11,804 | | 73 | | 45 | 13 | 4 | 4 | 3 | | | 162 | 262 | 83 |
| 27R-1, 28–33 | 638.01 | 96.0 | 13,263 | | 113 | | 54 | 26 | 6 | 8 | 2 | | | 117 | 246 | 63 |
| 28R-4, 0–5 | 651.93 | 98.1 | 16,797 | | 170 | | 62 | 29 | 7 | 12 | 4 | 2 | 1 | 99 | 271 | 59 |
| 29R-4, 0–5 | 661.43 | 99.5 | 7,946 | | 48 | | 16 | 6 | 2 | 3 | 1 | | | 166 | 497 | 105 |
| 30R-3, 0–5 | 669.63 | 100.8 | 6,369 | | 75 | | 37 | 26 | 5 | 9 | 4 | 2 | 1 | 85 | 172 | 40 |
| 31R-5, 0–5 | 682.23 | 102.7 | 3,707 | | 46 | | 21 | 10 | 3 | 4 | 2 | 1 | | 81 | 177 | 43 |
| 32R-5, 0–5 | 691.83 | 104.1 | 10,530 | | 82 | | 35 | 15 | 4 | 7 | 3 | 1 | 1 | 128 | 301 | 71 |
| 33R-1, 0–5 | 695.43 | 104.7 | 5,438 | | 34 | | 14 | 6 | 2 | 3 | 1 | 1 | | 160 | 388 | 89 |
| 34R-2, 0–5 | 706.53 | 106.4 | 7,932 | | 77 | | 30 | 13 | 3 | 5 | 2 | 1 | | 103 | 264 | 61 |
| 35R-5, 0–5 | 720.63 | 108.5 | 7,782 | | 104 | | 48 | 28 | 6 | 8 | 3 | 2 | 1 | 75 | 162 | 39 |
| 37R-5, 0–5 | 739.83 | 111.4 | 14,239 | | 128 | | 47 | 17 | 5 | 6 | 2 | 1 | 1 | 111 | 303 | 69 |
| 38R-4, 0–5 | 747.93 | 112.7 | 8,558 | | 93 | | 42 | 22 | 5 | 8 | 3 | 2 | 1 | 92 | 204 | 49 |
| 39R-5, 0–5 | 759.03 | 114.3 | 15,502 | | 153 | | 50 | 21 | 5 | 6 | 2 | 2 | 5 | 101 | 310 | 64 |
| 40R-5, 0–5 | 768.63 | 115.8 | 6,423 | | 90 | | 61 | 34 | 10 | 14 | 6 | 4 | 2 | 71 | 105 | 29 |
| 41R-4, 0–5 | 776.73 | 117.0 | 8,144 | | 76 | | 29 | 16 | 3 | 4 | 2 | 1 | 1 | 107 | 281 | 62 |
| 42R-5, 0–5 | 787.83 | 118.7 | 6,634 | | 105 | | 53 | 27 | 8 | 11 | 5 | 3 | 2 | 63 | 125 | 31 |
| 43R-2, 0–5 | 792.93 | 119.5 | 4,624 | | 68 | | 34 | 16 | 5 | 7 | 3 | 2 | 1 | 68 | 136 | 34 |
| 44R-3, 0–5 | 804.13 | 121.2 | 8,485 | | 122 | | 56 | 29 | 9 | 11 | 5 | 3 | 2 | 70 | 152 | 36 |
| 45R-4, 0–5 | 815.23 | 122.9 | 8,604 | | 95 | | 46 | 23 | 8 | 11 | 4 | 3 | 2 | 91 | 187 | 45 |
| 46R-3, 0–5 | 823.33 | 124.1 | 4,278 | | 73 | | 32 | 14 | 5 | 7 | 3 | 1 | 1 | 59 | 134 | 31 |
| 47R-2, 0–5 | 831.43 | 125.3 | 6,442 | | 70 | | 29 | 13 | 5 | 8 | 3 | 2 | 1 | 92 | 222 | 49 |
| 48R-2, 0–5 | 841.03 | 126.8 | 3,947 | | 43 | | 13 | 4 | 2 | 3 | 1 | 1 | 1 | 92 | 304 | 58 |
| 49R-1, 0–5 | 849.23 | 128.0 | 1,111 | | 26 | | 13 | 4 | 2 | 3 | 1 | 1 | 1 | 43 | 85 | 22 |
| 50R-4, 0–5 | 863.33 | 130.2 | 643 | | 10 | | 4 | 2 | | 1 | | | | 64 | 161 | 38 |
| 51R-5, 0–5 | 874.25 | 131.8 | 8,405 | | 170 | | 78 | 11 | 29 | 11 | 15 | 5 | 3 | 49 | 108 | 26 |
| 52R-5, 0–5 | 884.13 | 133.3 | 14,141 | | 296 | | 141 | 70 | 21 | 34 | 12 | 5 | 3 | 48 | 100 | 24 |
| 53R-5, 0–5 | 893.63 | 134.8 | 19,600 | | 409 | | 179 | 84 | 28 | 56 | 28 | 7 | 5 | 48 | 109 | 25 |
| 54R-1, 0–5 | 897.33 | 135.4 | 7,561 | | 105 | | 30 | 9 | 3 | 4 | 1 | | | 72 | 252 | 50 |
| 55R-2, 0–5 | 908.43 | 137.0 | 7,618 | | 155 | | 56 | 28 | 8 | 20 | 4 | 3 | 1 | 49 | 136 | 28 |
| 57R-2, 0–5 | 927.63 | 140.0 | 9,139 | | 153 | | 45 | 9 | 6 | 12 | 3 | 2 | 1 | 60 | 203 | 40 |
| 58R-2, 0–5 | 937.23 | 141.4 | 26,761 | | 592 | | 186 | 64 | 22 | 38 | 10 | 5 | 3 | 45 | 144 | 29 |
| 59R-2, 0–5 | 956.53 | 144.3 | 26,447 | | 449 | | 114 | 33 | 14 | 19 | 6 | 3 | 1 | 59 | 232 | 41 |

Notes: Sed. T = estimated sediment temperature, based on geothermal temperature gradient of 151.9°C/km, $C_1$ = methane, $C_{2=}$ = ethylene, $C_2$ = ethane, $C_{3=}$ = propylene, $C_3$ = propane, $IC_4$ = iso-butane, $NC_4$ = *n*-butane, $IC_5$ = iso-pentane, $NC_5$ = *n*-pentane, $IC_6$ = iso-hexane, $NC_6$ = *n*-hexane, $C_1/C_2$ = methane/ethane ratio, $C_1/C_3$ = methane/propane ratio, $C_1/C_{2+}$ = methane/other hydrocarbon gases ratio.

**Table 9. Results of vacutainer gas analyses of Hole 986A and 986C samples.**

| Core, section, interval (cm) | Depth (mbsf) | $C_1$ (ppm) | $C_2$ (ppm) | $C_3$ (ppm) | $C_1/C_2$ | $C_1/C_3$ | $C_1/C_{2+}$ |
|---|---|---|---|---|---|---|---|
| 160-986A- | | | | | | | |
| 6H-3, 64–65 | 46.25 | 258,447 | 17 | | 15,203 | | 15,203 |
| 6H-3, 145–146 | 47.06 | 861,919 | 61 | | 14,130 | | 14,130 |
| 7H-3, 53–54 | 54.70 | 395,888 | 35 | | 11,311 | | 11,311 |
| 8H-4, 81–82 | 66.87 | 435,072 | 46 | | 9,458 | | 9,458 |
| 9H-2, 13–14 | 72.74 | 314,325 | 41 | | 7,666 | | 7,666 |
| 10H-4, 51–52 | 83.55 | 298,053 | 49 | | 6,083 | | 6,083 |
| 13H-3, 77–78 | 105.38 | 843,412 | 230 | 8 | 3,667 | 105,427 | 3,544 |
| 14H-3, 55–56 | 109.16 | 209,182 | 63 | 2 | 3,320 | 104,591 | 3,218 |
| 15X-1, 68–69 | 114.59 | 207,050 | 86 | 3 | 2,408 | 69,017 | 2,326 |
| 16X-3, 81–82 | 123.12 | 91,275 | 40 | 4 | 2,282 | 22,819 | 2,074 |
| 17X-3, 81–82 | 132.72 | 853,674 | 272 | 12 | 3,139 | 71,140 | 3,006 |
| 19X-4, 34–35 | 152.95 | 246,980 | 63 | 3 | 3,920 | 82,327 | 3,742 |
| 20X-5, 3–4 | 163.84 | 97,428 | 21 | 1 | 4,639 | 97,428 | 4,429 |
| 21X-4, 148–149 | 172.01 | 309,009 | 59 | 3 | 5,237 | 103,003 | 4,984 |
| 24X-2, 68–69 | 198.59 | 155,224 | 19 | 1 | 8,170 | 155,224 | 7,761 |
| 160-986C- | | | | | | | |
| 37X-4, 30–31 | 334.60 | 470,832 | 87 | 5 | 5,412 | 94,166 | 5,118 |
| 38X-2, 30–31 | 342.41 | 89,186 | 21 | 1 | 4,247 | 89,186 | 4,054 |
| 39X-2, 141–142 | 353.12 | 79,703 | 20 | 1 | 3,985 | 79,703 | 3,795 |
| 40X-3, 20–21 | 362.51 | 183,052 | 41 | 2 | 4,465 | 91,526 | 4,257 |
| 41X-3, 81–82 | 373.22 | 99,435 | 32 | 1 | 3,107 | 99,435 | 3,013 |
| 42X-3, 15–16 | 382.26 | 125,124 | 37 | 1 | 3,382 | 125,124 | 3,293 |

Notes: $C_1$ = methane, $C_2$ = ethane, $C_3$ = propane, $C_1/C_2$ = methane/ethane ratio, $C_1/C_3$ = methane/propane ratio, and $C_1/C_{2+}$ = methane/other hydrocarbon gases ratio.

12; Fig. 23N). Values then increase to a peak at about 740 mbsf and then remain low to the bottom of the hole. Strontium concentrations increase from seawater values (87 µM) near the top of Hole 986C to a distinct maximum at 437 mbsf, and then slowly decrease toward the base of the hole (Table 12; Fig. 23O).

## PHYSICAL PROPERTIES

A main objective of the physical properties measurements at Site 986 was to increase our understanding of how physical processes affect high-latitude continental margin sediments. Of particular interest at this site was to relate changes in the sediment physical properties to glacial-interglacial variations and sedimentary processes under various climatic regimes. Since a seismic stratigraphy recently was defined for the entire Svalbard–Barents Sea continental margin (Faleide et al., 1996), an additional objective was to relate the seismic character of regional seismic sequences to sedimentary characteristics, including physical properties.

Physical properties measurements at Site 986 included index properties, bulk density as measured by the GRAPE, *P*-wave velocity using the PWL on whole-round cores and the DSV and Hamilton frame on split cores, undrained shear strength, using both the motorized vane and a fall-cone apparatus, magnetic susceptibility, natural gamma radiation, and thermal conductivity. Downhole temperature measurements were carried out at three depths (26.5, 45.5 and 62.3 mbsf) in Hole 986C, using the APC temperature device.

Laboratory methods and procedures are described in the "Explanatory Notes" chapter (this volume). The index properties, compressional velocities, and shear strength data from Site 986 are presented in Tables 13 to 16, while maximum, minimum, and mean values of the same parameters for each geotechnical unit are presented in Table 17. Thermal conductivities are reported in Table 18.

### Results

In establishing a geotechnical stratigraphy for Site 986, we have used laboratory measurements from Holes 986C and 986D, combined with wireline logging results from Hole 986C and the approximately 100 m logged in Hole 986D (see "Wireline Logging" section, this chapter). In particular the velocity, density, and natural gamma radiation logs are important for characterizing the sediment physical properties in intervals of low or no recovery. The MST measurements have only been of limited use at Site 986 because of the low recovery (56.3% and 41.9% for Holes 986C and 986D, respectively), gas expansion, and effects of drilling disturbance in XCB and RCB cores. Only natural gamma radiation values, uncorrected for volume variability, are discussed in the present report, even though the values must be viewed with caution. The presence of gas in the sediments below approximately 20 mbsf made velocity measurements particularly problematic at this site. Because the cores had to be drained by drilling holes through the liner at ~10-cm intervals, the liner was no longer in fluid contact with the sediment. As a consequence, *P*-wave velocities could not be measured with the PWL sensor on the MST below 20 mbsf. Furthermore, velocity measurements on discrete samples also failed to a large extent between 30 and 350 mbsf (Table 14; Fig. 25) because of high signal attenuation in the samples. The most likely explanation for this is the presence of gas in the pore voids (see "Organic Geochemistry" section, this chapter), and possible microcracks caused by gas expansion. Within these limitations, four geotechnical units, G1 to G4, have been defined, based on the downhole trends in physical properties of the sediments at Site 986.

#### *Geotechnical Unit G1 (0–230 mbsf)*

Based on differences in the rate of downhole change and in the scatter of measured physical properties, geotechnical Unit G1 has been divided in two subunits, G1A and G1B (Fig. 25).

Subunit G1A (0–55 mbsf) is characterized by a relatively rapid decrease in porosity, from average values of 60% to about 50%, and an increase in bulk density from about 1.7 g/cm$^3$ to 1.8 g/cm$^3$. The gradients are steepest in the upper 30 mbsf. Superimposed on these general trends, a wide scatter in measured values is seen. *P*-wave velocities show a slight increase in the upper 20 mbsf, and a more scattered and decreasing trend between 20 and 30 mbsf, probably caused by increasing gas content in the cores, as well as disturbance caused by methane escape. Undrained shear strength ($S_u$) shows a distinctly increasing trend (Fig. 25). Geotechnical Subunit G1A corresponds to the upper half of lithostratigraphic Unit I, which is defined as a silty clay with dropstones (see "Lithostratigraphy" section, this chapter). With regard to the seismic stratigraphy, Subunit G1A corresponds to seismic Unit SV-I and most of SV-II (see "Seismic Stratigraphy" section, this chapter).

The overall downhole trends of geotechnical Subunit G1A continue in Subunit G1B (55–230 mbsf), but with less steep gradients. There is a small, but distinct drop in bulk density, and a corresponding increase in porosity across the subunit boundary. Another significant change is that the scatter in index property values is less in Subunit G1B than in Subunit G1A (Fig. 25). Undrained shear strength values, on the other hand, show a higher scatter in Subunit G1B than in G1A, and the difference between values measured with the motorized vane and the fall-cone penetrometer becomes more pronounced. This indicates a higher content of coarser grains and also that the sediment tends to fracture when using the vane.

Geotechnical Subunit G1B corresponds roughly to seismic sequences SV-III, SV-IV, and Subunit SV-VA, which show similar seismic character as the two sequences above, but with two distinct intervals interpreted to represent debris flows (see "Seismic Stratigraphy" section, this chapter). With respect to lithostratigraphy, geotechnical Subunit G1B corresponds to the lower part of lithostratigraphic Unit I and the upper part of Subunit II, which differ from each other in the relative abundance of dropstones (see "Lithostratigraphy" section, this chapter). The debris-flow deposit identified at approximately 160–173 mbsf is characterized by distinctly increased compressional velocities, bulk densities as well as an increase in natural gamma radiation counts (Fig. 25).

**Table 10. Rock-Eval data for Hole 986C and 986D samples.**

| Core, section, interval (cm) | Depth (mbsf) | TOC (%) | $T_{max}$ (°C) | $S_1$ | $S_2$ | $S_3$ | PI | $S_2/S_3$ | PC | HI | OI |
|---|---|---|---|---|---|---|---|---|---|---|---|
| 162-986C- | | | | | | | | | | | |
| 1H-4, 67–68 | 5.17 | 1.63 | 546 | 0.32 | 0.40 | 1.18 | 0.45 | 0.34 | 0.06 | 25 | 72 |
| 6H-2, 95–96 | 47.95 | 1.17 | 545 | 0.09 | 0.40 | 1.96 | 0.19 | 0.20 | 0.04 | 34 | 167 |
| 10X-2, 50–51 | 82.60 | 1.04 | 441 | 0.17 | 0.33 | 1.28 | 0.35 | 0.25 | 0.04 | 31 | 123 |
| 10X-4, 28–29 | 85.38 | 1.37 | 438 | 0.18 | 0.55 | 1.90 | 0.25 | 0.29 | 0.06 | 40 | 139 |
| 11X-3, 88–89 | 94.08 | 1.00 | 545 | 0.21 | 0.93 | 1.12 | 0.18 | 0.83 | 0.09 | 93 | 112 |
| 12X-1, 33–34 | 100.13 | 1.16 | 545 | 0.11 | 0.45 | 1.77 | 0.20 | 0.26 | 0.05 | 39 | 153 |
| 13X-1, 34–35 | 109.84 | 1.26 | 543 | 0.14 | | 1.99 | | | | | 158 |
| 14X-3, 27–28 | 121.71 | 1.29 | 487 | 0.20 | 0.26 | 1.17 | 0.44 | 0.22 | 0.04 | 20 | 91 |
| 17X-3, 4–5 | 151.14 | 1.27 | 451 | 0.21 | 0.37 | 3.87 | 0.37 | 0.09 | 0.05 | 29 | 305 |
| 17X-6, 37–38 | 155.81 | 1.44 | 544 | 0.33 | | 2.63 | | | | | 182 |
| 19X-2, 86–87 | 169.76 | 1.20 | 451 | 0.12 | 0.36 | 1.19 | 0.25 | 0.30 | 0.04 | 30 | 99 |
| 20X-1, 21–22 | 177.31 | 1.88 | 512 | 0.26 | | 1.02 | | | | | 54 |
| 21X-2, 41–42 | 188.61 | 1.02 | 439 | 0.13 | 0.86 | 0.78 | 0.13 | 1.10 | 0.08 | 85 | 77 |
| 28X-2, 30–31 | 255.80 | 1.06 | 437 | 0.02 | 0.83 | 1.05 | 0.02 | 0.80 | 0.07 | 78 | 99 |
| 29X-1, 30–31 | 259.30 | 1.06 | 431 | 0.03 | 0.89 | 1.29 | 0.03 | 0.69 | 0.08 | 84 | 122 |
| 30X-2, 28–29 | 265.38 | 1.24 | 543 | 0.10 | | 1.55 | | | | | 125 |
| 30X-3, 28–29 | 266.88 | 1.41 | 440 | 0.17 | 0.60 | 0.83 | 0.23 | 0.72 | 0.06 | 42 | 59 |
| 36X-1, 25–26 | 321.55 | 1.13 | 430 | 0.26 | 0.72 | 0.63 | 0.26 | 1.16 | 0.08 | 64 | 55 |
| 40X-2, 29–30 | 361.59 | 1.03 | 440 | 0.14 | 0.51 | 0.75 | 0.22 | 0.68 | 0.05 | 49 | 73 |
| 42X-1, 87–88 | 379.97 | 1.00 | 442 | 0.14 | 0.36 | 0.63 | 0.27 | 0.57 | 0.04 | 36 | 63 |
| 43X-3, 94–95 | 392.64 | 1.14 | 433 | 0.23 | 1.98 | 0.78 | 0.11 | 2.53 | 0.18 | 173 | 68 |
| 162-986D- | | | | | | | | | | | |
| 2R-1, 65–66 | 398.05 | 1.19 | 368 | 0.18 | | 0.90 | | | | | 76 |
| 14R-1, 9–10 | 512.79 | 1.25 | 466 | 0.12 | 0.53 | 2.67 | 0.19 | 0.20 | 0.05 | 42 | 214 |
| 14R-3, 89–90 | 516.59 | 1.15 | 466 | 0.06 | 0.56 | 1.06 | 0.10 | 0.53 | 0.05 | 49 | 92 |
| 15R-1, 44–45 | 522.74 | 1.87 | 434 | 0.07 | 1.00 | 1.13 | 0.06 | 0.89 | 0.09 | 54 | 60 |
| 15R-3, 33–34 | 525.63 | 1.10 | 428 | 0.10 | 0.96 | 0.63 | 0.09 | 1.53 | 0.09 | 88 | 57 |
| 17R-1, 120–121 | 542.70 | 1.35 | 433 | 0.14 | 1.41 | 1.04 | 0.09 | 1.35 | 0.13 | 104 | 77 |
| 18R-1, 93–94 | 552.03 | 1.28 | 419 | 0.09 | | 1.68 | | | | | 131 |
| 19R-1, 12–13 | 560.82 | 1.24 | 434 | 0.05 | 1.00 | 1.65 | 0.05 | 0.61 | 0.09 | 81 | 133 |
| 28R-5, 52–53 | 653.92 | 1.14 | 436 | 0.04 | 0.71 | 0.86 | 0.06 | 0.83 | 0.06 | 62 | 75 |
| 60R-1, 67–68 | 955.67 | 1.22 | 427 | 0.09 | 1.88 | 0.58 | 0.04 | 3.26 | 0.16 | 154 | 47 |

Notes: TOC = total organic carbon obtained by NCHS elemental analysis, $T_{max}$ = temperature (°C) of maximum hydrocarbon generation from kerogen, $S_1$ (mg HC/g rock) = volatile hydrocarbons, $S_2$ (mg HC/g rock) = kerogen-derived hydrocarbons, $S_3$ (mg $CO_2$/g rock) = organic $CO_2$ from kerogen, PI ($S_1 + S_2$) = productivity index, $S_2/S_3$ = kerogen-type index, PC ($0.083 \cdot [S_1 + S_2]$) = petroleum potential, HI ($100 \cdot S_2$/TOC) = hydrogen index, and OI ($100 \cdot S_3$/TOC) = oxygen index.

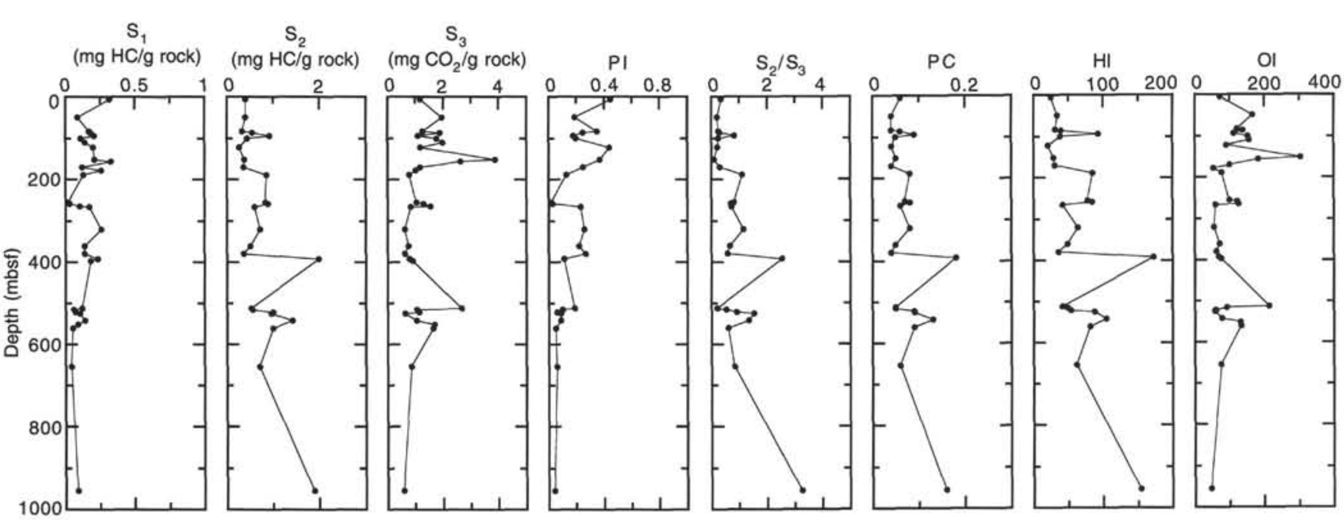


Figure 19. Results of Rock-Eval pyrolysis for Site 986. $S_1$ (mg HC/g rock) = volatile hydrocarbons; $S_2$ (mg HC/g rock) = kerogen-derived hydrocarbons; $S_3$ (mg $CO_2$/g rock) = organic $CO_2$ from kerogen; PI ($S_1 + S_2$) = productivity index; $S_2/S_3$ = kerogen-type index; PC ($0.083 \times [S_1 + S_2]$) = petroleum potential; HI ($100 \times S_2$/TOC) = hydrogen index; and OI ($100 \times S_3$/TOC) = oxygen index.

### *Geotechnical Unit G2 (230–560 mbsf)*

The physical properties of geotechnical Unit G2 are characterized by large-scale variations, which are particularly obvious in the density and velocity logs, but are also distinct in the natural gamma radiation values (Fig. 25). Although distinct intervals within geotechnical Subunit G1B also have a similar character, Unit G2 is dominated by frequent shifts in density and velocity of up to 0.35 g/cm$^3$ and 500 m/s, respectively, over intervals varying from 5 to 20 m. In particular the high-velocity/high-density intervals have poor recovery, and consequently, fewer measurements of physical properties. However, where measured, there is (with a few exceptions) a relatively good correspondence between bulk densities measured in the laboratory and the downhole logging values (Fig. 25). Because of gas, there are few discrete velocity measurements through this interval, and these show values that appear too low, compared to the logging results.

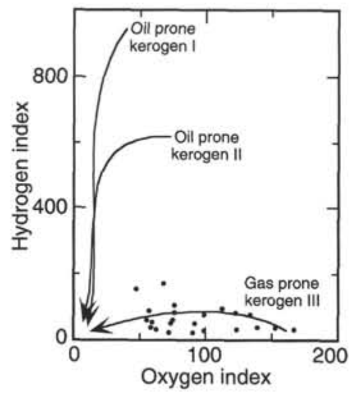


Figure 20. Diagram of hydrogen index vs. oxygen index from Rock-Eval pyrolysis data at Site 986. Three arrows indicate pathways of maturity for kerogen Types I, II, and III.

Two relatively high values of 2000 and 2600 m/s measured toward the lower part of the unit are possible exceptions. The undrained shear strength values show an increased scatter in the upper part of Unit G2, before $S_u$ reaches the measurement limits of the instruments used (Fig. 25).

The low core recovery between 400 and 650 mbsf makes definition of unit boundaries uncertain. The lower boundary of Unit G2 at 560 mbsf is, however, based on a decrease in the natural gamma radiation values and a shift to higher velocities and lower porosities in the next unit, and is therefore relatively well constrained. Additional support for the position of the boundary comes from a close correspondence between the lower boundary of geotechnical Unit G2 and the base of lithostratigraphic Unit II (see "Lithostratigraphy" section, this chapter). With respect to the seismic stratigraphy, Unit G2 corresponds to seismic Subunit SV-VB and seismic Unit SV-VI, dominated by high-amplitude reflectors. The lower boundary of geotechnical Unit G2 coincides with seismic Reflector R6, which has regional significance over the entire Svalbard–Barents Sea continental margin (Faleide et al., 1996).

### *Geotechnical Unit G3 (560–897 mbsf)*

Bulk density and porosity show similar trends of increasing and decreasing values with depth, respectively, as in Unit G2 (Fig. 25; Tables 13, 14, 17). However, assigning the two index properties measurements in Core 162-986D-21R, at approximately 583 mbsf, to Unit G2, there is a parallel shift in the trends across the boundary between the two units (Fig. 25). This is more pronounced in the velocity measurements, which show a scatter around 1900 m/s in Unit G2, while the average velocities increase from 2250 to 2450 m/s in Unit G3. Natural gamma radiation values show a decreasing trend across the unit boundary before they reach a more even level below a nonrecovery interval in geotechnical Unit G3. A small but detectable low in bulk density and corresponding high in porosity around 700 mbsf is probably caused by severe drilling disturbance in Cores 192-986D-32R to 34R. No velocities were measured in this or equally disturbed intervals.

Geotechnical Unit G3 corresponds to seismic Unit SV-VII, defined between the regionally significant seismic Reflectors R6 and R7 (see "Seismic Stratigraphy" section, this chapter). With respect to lithostratigraphy, geotechnical Subunit G3A corresponds to the upper part of lithostratigraphic Unit III, while Subunit G3B corresponds to the remaining part of lithostratigraphic Unit III and Subunit IVA (see "Lithostratigraphy" section, this chapter). Lithostratigraphic Unit III is defined by its increased sand content relative to the units above and below.

### *Geotechnical Unit G4 (900–965 mbsf)*

The boundary between geotechnical Units G3 and G4 is distinctly marked by a decrease in bulk density and velocity, and a corresponding increase in porosity (Fig. 25). This transition is also marked by a change into dark, clay-rich sediments with reduced sand content in lithostratigraphic Subunit IVB (see "Lithostratigraphy" section, this chapter), and is accompanied by a reduced core recovery (see "Operations" section, this chapter). The lithologic change is reflected in an increasing trend in natural gamma-ray counts in geotechnical Unit G4. The boundary corresponds to seismic Reflector R7, and geotechnical Unit G4 corresponds to seismic Unit SV-VIII (see "Seismic Stratigraphy" section, this chapter).

## Discussion

The overall, large-scale trend in physical properties at Site 986, is that of steadily changing values with depth in response to increased overburden (Fig. 25). However, superimposed on this general trend are variations caused by lithology and different sedimentary processes. Correlation with the seismic records is particularly useful when interpreting the physical properties profiles at Site 986.

The gas-bearing sediments at Site 986 were clearly observable upon core retrieval and splitting. With respect to the physical properties, the most clearly observed effect of gas is that it was essentially impossible to measure velocities on sediment samples between 30 and 350 mbsf. One would expect gas to result in anomalous relationships between porosity and water content. However, because the methods for porosity calculations assume water saturated sediment (see "Explanatory Notes" chapter, this volume), gas was not indicated by the index properties.

The variations in bulk density and porosity observed through geotechnical Units G1 and G2, are most likely a result of varying lithology caused by changes between processes of downslope gravity driven mass wasting (turbidites and debris flows) and hemipelagic sedimentation. The presence of debris-flow deposits is supported by lithology showing an increased content of clasts and shell fragments (see "Lithostratigraphy" section, this chapter). Further support is given by the seismic character of these upper units. Seismic lines parallel to the continental slope, that is, normal to the potential flow direction of debris flows and turbidites, show discontinuous weak reflectors with an undulating relief. Lines perpendicular to the slope, on the other hand, show the same reflectors to be continuous and conformable over the length of the survey lines (see "Seismic Stratigraphy" section, this chapter). Sand layers varying in thickness from a few centimeters to 0.5 m are interpreted as turbidites. The thicker sand layers commonly appear nearly fluidized, and therefore, no physical properties measurements were carried out on these. Although there are frequent intervals that represent depositional mechanisms other than mass wasting (e.g., distal glacial marine deposition), debris flows seem to be predominant by volume, and would therefore have a major effect on the high sedimentation rates estimated for the site (see "Sedimentation Rates" section, this chapter).

The relatively distinct change in character seen between geotechnical Units G1 and G2, as well as between seismic Subunits SV-VA and SV-VB (see "Seismic Stratigraphy" section, this chapter), indicates a change in mass-wasting activity at the time corresponding to the Unit G1–G2 transition. Within Unit G2, each individual event appears to be represented by a thicker sediment layer than those of Unit G1, where more frequent small-scale events with apparently less significant effect on the overall physical properties character are observed. Occasional large-scale debris flows, like the one observed between 160 and 173 mbsf, represent events of the same magnitude as the ones in geotechnical Unit G2. Physical property changes characteristic of the debris-flow deposits appear to involve increased levels of compressional velocity and bulk density by 300–500 m/s, and

**Table 11. Summary of organic geochemical analyses of Hole 986C and 986D samples.**

| Core, section, interval (cm) | Depth (mbsf) | IC (%) | $CaCO_3$ (%) | TC (%) | TOC (%) | TN (%) | TS (%) | C/N | C/S |
|---|---|---|---|---|---|---|---|---|---|
| 162-986C- | | | | | | | | | |
| 1H-1, 16–17 | 0.16 | 1.55 | 12.9 | 2.38 | 0.83 | 0.11 | 0.79 | 7.7 | 1.0 |
| 1H-4, 67–68 | 5.17 | 0.63 | 5.2 | 2.26 | 1.63 | 0.13 | 0.51 | 12.5 | 3.2 |
| 2H-1, 35–36 | 7.85 | 0.41 | 3.4 | 0.95 | 0.54 | 0.06 | 0.06 | 8.8 | 9.0 |
| 2H-3, 63–64 | 11.13 | 0.89 | 7.4 | 1.31 | 0.42 | 0.05 | 0.03 | 8.5 | 14.4 |
| 2H-5, 77–78 | 14.27 | 1.19 | 9.9 | | | | | | |
| 3H-1, 25–26 | 17.25 | 0.11 | 0.9 | 0.48 | 0.37 | 0.04 | 0.00 | 9.8 | |
| 3H-4, 31–32 | 21.81 | 0.32 | 2.7 | 1.09 | 0.77 | 0.07 | 0.12 | 11.8 | 6.7 |
| 3H-6, 16–17 | 24.66 | 0.27 | 2.2 | | | | | | |
| 4H-2, 57–58 | 28.57 | 0.66 | 5.5 | 1.11 | 0.45 | 0.07 | 0.00 | 6.1 | |
| 4H-3, 80–81 | 30.30 | 0.72 | 6.0 | | | | | | |
| 4H-5, 67–69 | 33.17 | 0.18 | 1.5 | 0.91 | 0.73 | 0.07 | 0.09 | 10.2 | 8.5 |
| 5H-2, 25–26 | 37.55 | 0.44 | 3.7 | 0.95 | 0.51 | 0.05 | 0.00 | 10.1 | |
| 5H-4, 136–137 | 40.54 | 2.36 | 19.7 | 2.82 | 0.46 | 0.07 | 0.00 | 7.1 | |
| 5H-5, 31–32 | 40.99 | 0.34 | 2.8 | 1.17 | 0.83 | 0.10 | 0.04 | 8.0 | 20.2 |
| 6H-2, 95–96 | 47.95 | 0.54 | 4.5 | 1.71 | 1.17 | 0.07 | 0.13 | 16.1 | 9.4 |
| 6H-4, 92–93 | 50.92 | 0.27 | 2.2 | 0.92 | 0.65 | 0.06 | 2.16 | 10.1 | 0.3 |
| 7H-2, 25–26 | 56.05 | 0.83 | 6.9 | 1.80 | 0.97 | 0.10 | 0.48 | 9.8 | 2.0 |
| 7H-4, 23–24 | 59.03 | 1.06 | 8.8 | 1.97 | 0.91 | 0.13 | 0.10 | 7.0 | 8.8 |
| 7H-5, 25–26 | 60.55 | 0.70 | 5.8 | 1.50 | 0.80 | 0.08 | 0.05 | 9.8 | 15.8 |
| 8H-3, 33–34 | 65.63 | 0.95 | 7.9 | 1.86 | 0.91 | 0.09 | 0.10 | 10.4 | 8.8 |
| 8H-4, 33–34 | 66.67 | 0.63 | 5.2 | 0.81 | 0.18 | 0.01 | 0.25 | 12.0 | 0.7 |
| 10X-2, 50–51 | 82.60 | 0.53 | 4.4 | 1.57 | 1.04 | 0.10 | 0.09 | 10.9 | 11.5 |
| 10X-4, 28–29 | 85.38 | 0.59 | 4.9 | 1.96 | 1.37 | 0.08 | 0.10 | 18.3 | 14.2 |
| 11X-3, 88–89 | 94.08 | 0.30 | 2.5 | 1.30 | 1.00 | 0.11 | 0.05 | 9.0 | 18.6 |
| 11X-5, 95–96 | 97.15 | 0.20 | 1.7 | 0.49 | 0.29 | 0.09 | 0.55 | 3.4 | 0.5 |
| 11X-5, 140–141 | 97.60 | 3.16 | 26.3 | | | | | | |
| 12X-1, 33–34 | 100.13 | 0.35 | 2.9 | 1.51 | 1.16 | 0.12 | 0.22 | 9.8 | 5.3 |
| 12X-3, 34–35 | 102.62 | 0.93 | 7.7 | 1.90 | 0.97 | 0.11 | 0.66 | 8.9 | 1.5 |
| 13X-1, 34–35 | 109.84 | 0.33 | 2.7 | 1.59 | 1.26 | 0.12 | 0.25 | 10.3 | 5.0 |
| 13X-3, 33–34 | 112.83 | 0.20 | 1.7 | 0.46 | 0.26 | 0.08 | 0.13 | 3.3 | 2.0 |
| 14X-1, 46–47 | 119.66 | 0.35 | 2.9 | | | | | | |
| 14X-3, 27–28 | 121.71 | 1.20 | 10.0 | 2.49 | 1.29 | 0.13 | 0.40 | 10.0 | 3.2 |
| 14X-4, 34–35 | 123.28 | 0.19 | 1.6 | 0.93 | 0.74 | 0.12 | 0.17 | 6.4 | 4.4 |
| 15X-2, 34–35 | 130.13 | 0.26 | 2.2 | 0.60 | 0.34 | 0.08 | 0.11 | 4.3 | 3.2 |
| 15X-4, 33–34 | 133.12 | 0.62 | 5.2 | | | | | | |
| 15X-5, 26–27 | 134.55 | 0.56 | 4.7 | 0.81 | 0.25 | 0.09 | 0.16 | 2.8 | 1.6 |
| 16X-2, 83–84 | 140.48 | 2.80 | 23.3 | 2.98 | 0.18 | 0.07 | 0.15 | 2.6 | 1.2 |
| 16X-4, 62–63 | 143.27 | 0.12 | 1.0 | 0.95 | 0.83 | 0.12 | 0.15 | 7.2 | 5.6 |
| 16X-6, 89–90 | 146.54 | 0.21 | 1.7 | | | | | | |
| 17X-3, 4–5 | 151.14 | 3.44 | 28.7 | 4.71 | 1.27 | 0.12 | 0.21 | 10.4 | 6.1 |
| 17X-3, 133–134 | 152.43 | 0.13 | 1.1 | 0.65 | 0.52 | 0.10 | 0.13 | 5.4 | 4.0 |
| 17X-6, 37–38 | 155.81 | 0.72 | 6.0 | 2.16 | 1.44 | 0.13 | 0.24 | 11.3 | 6.1 |
| 18X-CC, 12–13 | 157.92 | 0.32 | 2.7 | 0.73 | 0.41 | 0.09 | 0.14 | 4.3 | 2.8 |
| 19X-2, 11–12 | 169.01 | 0.70 | 5.8 | 0.98 | 0.28 | 0.06 | 0.21 | 5.1 | 1.3 |
| 19X-2, 46–47 | 169.36 | 0.36 | 3.0 | | | | | | |
| 19X-2, 86–87 | 169.76 | 0.87 | 7.2 | 2.07 | 1.20 | 0.12 | 0.51 | 10.0 | 2.3 |
| 20X-1, 21–22 | 177.31 | 0.62 | 5.2 | 2.50 | 1.88 | 0.17 | 0.40 | 10.8 | 4.7 |
| 20X-2, 31–32 | 178.91 | 0.30 | 2.5 | 1.04 | 0.74 | 0.12 | 0.67 | 6.2 | 1.1 |
| 21X-1, 47–48 | 187.17 | 0.19 | 1.6 | | | | | | |
| 21X-1, 77–78 | 187.47 | 0.10 | 0.8 | 0.89 | 0.79 | 0.11 | 0.12 | 7.2 | 6.5 |
| 21X-2, 41–42 | 188.61 | 0.76 | 6.3 | 1.78 | 1.02 | 0.10 | 0.00 | 10.2 | |
| 22X-1, 110–111 | 197.40 | 0.14 | 1.2 | 0.70 | 0.56 | 0.11 | 0.10 | 5.2 | 5.4 |
| 22X-3, 30–31 | 199.60 | 0.19 | 1.6 | 1.12 | 0.93 | 0.13 | 0.40 | 7.0 | 2.3 |
| 24X-1, 30–31 | 215.80 | 0.09 | 0.7 | 0.41 | 0.32 | 0.09 | 0.09 | 3.4 | 3.4 |
| 26X-1, 30–31 | 235.00 | 0.58 | 4.8 | 1.52 | 0.94 | 0.12 | 0.17 | 8.1 | 5.6 |
| 28X-2, 30–31 | 255.80 | 0.59 | 4.9 | 1.65 | 1.06 | 0.15 | 0.16 | 7.2 | 6.5 |
| 29X-1, 30–31 | 259.30 | 0.89 | 7.4 | 1.95 | 1.06 | 0.15 | 0.18 | 6.9 | 5.9 |
| 29X-4, 26–27 | 263.76 | 0.14 | 1.2 | 0.61 | 0.47 | 0.10 | 0.82 | 4.8 | 0.6 |
| 30X-2, 28–29 | 265.38 | 0.54 | 4.5 | 1.78 | 1.24 | 0.14 | 0.14 | 9.0 | 9.0 |
| 30X-3, 28–29 | 266.88 | 0.87 | 7.2 | 2.28 | 1.41 | 0.13 | 0.50 | 11.0 | 2.9 |
| 34X-1, 30–31 | 302.40 | 0.14 | 1.2 | 0.87 | 0.73 | 0.12 | 0.54 | 5.9 | 1.4 |
| 35X-1, 93–94 | 312.63 | 0.69 | 5.7 | 1.62 | 0.93 | 0.10 | 0.20 | 9.4 | 4.6 |
| 36X-1, 25–26 | 321.55 | 0.59 | 4.9 | 1.72 | 1.13 | 0.10 | 0.19 | 11.2 | 5.9 |
| 37X-2, 35–36 | 332.75 | 0.35 | 2.9 | 1.26 | 0.91 | 0.11 | 0.18 | 8.6 | 5.2 |
| 39X-3, 36–37 | 353.56 | 0.27 | 2.2 | 0.96 | 0.69 | 0.11 | 0.29 | 6.4 | 2.4 |
| 40X-2, 29–30 | 361.59 | 0.83 | 6.9 | 1.86 | 1.03 | 0.10 | 0.18 | 10.1 | 5.7 |
| 41X-2, 42–43 | 371.32 | 0.15 | 1.2 | 0.94 | 0.79 | 0.12 | 0.14 | 6.8 | 5.5 |
| 42X-1, 87–88 | 379.97 | 1.64 | 13.7 | 2.64 | 1.00 | 0.09 | 0.41 | 11.3 | 2.5 |
| 42X-3, 117–118 | 383.27 | 0.35 | 2.9 | 1.03 | 0.68 | 0.11 | 0.10 | 6.4 | 6.9 |
| 42X-4, 41–42 | 384.01 | 0.77 | 6.4 | 1.55 | 0.78 | 0.10 | 0.09 | 7.8 | 8.4 |
| 43X-1, 56–57 | 389.26 | 1.25 | 10.4 | 2.14 | 0.89 | 0.09 | 0.15 | 9.6 | 5.8 |
| 43X-2, 106–107 | 391.26 | 0.77 | 6.4 | 1.71 | 0.94 | 0.10 | 0.11 | 9.3 | 8.6 |
| 43X-3, 94–95 | 392.64 | 0.26 | 2.2 | 1.40 | 1.14 | 0.13 | 0.17 | 8.6 | 6.6 |
| 44X-1, 122–123 | 399.52 | 0.19 | 1.6 | 1.08 | 0.89 | 0.12 | 0.11 | 7.6 | 7.9 |
| 44X-2, 101–102 | 400.81 | 0.44 | 3.7 | 1.13 | 0.69 | 0.10 | 0.06 | 6.9 | 12.0 |
| 162-986D- | | | | | | | | | |
| 2R-1, 65–66 | 398.05 | 0.24 | 2.0 | 1.43 | 1.19 | 0.14 | 1.17 | 8.3 | 1.0 |
| 2R-4, 65–66 | 402.55 | 0.38 | 3.2 | 1.14 | 0.76 | 0.10 | 0.22 | 7.3 | 3.5 |
| 6R-1, 69–70 | 436.59 | 0.21 | 1.7 | 1.09 | 0.88 | 0.11 | 0.20 | 8.3 | 4.5 |
| 14R-1, 9–10 | 512.79 | 4.47 | 37.2 | 5.72 | 1.25 | 0.11 | 0.57 | 11.9 | 2.2 |
| 14R-3, 89–90 | 516.59 | 0.21 | 1.7 | 1.36 | 1.15 | 0.13 | 0.09 | 8.9 | 13.2 |
| 14R-4, 93–94 | 518.13 | 0.19 | 1.6 | | | | | | |
| 15R-1, 44–45 | 522.74 | 0.65 | 5.4 | 2.52 | 1.87 | 0.14 | 0.51 | 13.4 | 3.7 |
| 15R-3, 33–34 | 525.63 | 0.13 | 1.1 | 1.23 | 1.10 | 0.13 | 0.12 | 8.3 | 9.2 |
| 15R-4, 108–109 | 527.88 | 0.09 | 0.7 | | | | | | |
| 16R-1, 26–27 | 532.16 | 0.25 | 2.1 | 1.10 | 0.85 | 0.12 | 0.00 | 7.4 | |
| 16R-3, 35–36 | 535.25 | 0.23 | 1.9 | 1.15 | 0.92 | 0.14 | 0.00 | 6.7 | |

**Table 11 (continued).**

| Core, section, interval (cm) | Depth (mbsf) | IC (%) | $CaCO_3$ (%) | TC (%) | TOC (%) | TN (%) | TS (%) | C/N | C/S |
|---|---|---|---|---|---|---|---|---|---|
| 16R-6, 26–27 | 539.66 | 0.57 | 4.7 | | | | | | |
| 17R-1, 120–121 | 542.70 | 0.44 | 3.7 | 1.79 | 1.35 | 0.14 | 0.21 | 9.6 | 6.5 |
| 17R-2, 90–91 | 543.90 | 0.21 | 1.7 | 1.17 | 0.96 | 0.13 | 1.04 | 7.4 | 0.9 |
| 18R-1, 93–94 | 552.03 | 0.29 | 2.4 | 1.53 | 1.24 | 0.14 | 0.62 | 9.0 | 2.0 |
| 18R-3, 93–94 | 555.03 | 0.13 | 1.1 | 0.90 | 0.77 | 0.11 | 0.11 | 7.0 | 6.9 |
| 19R-1, 12–13 | 560.82 | 0.67 | 5.6 | 1.91 | 1.24 | 0.15 | 0.15 | 8.5 | 8.5 |
| 21R-1, 90–91 | 580.90 | 0.18 | 1.5 | 0.68 | 0.50 | 0.06 | 0.19 | 7.8 | 2.7 |
| 21R-3, 90–91 | 583.90 | 0.21 | 1.7 | 0.66 | 0.45 | 0.06 | 0.34 | 7.3 | 1.4 |
| 28R-5, 52–53 | 653.92 | 0.48 | 4.0 | 1.62 | 1.14 | 0.14 | 0.10 | 8.0 | 10.9 |
| 29R-1, 127–128 | 658.17 | 0.36 | 3.0 | 0.77 | 0.41 | 0.05 | 0.40 | 7.6 | 1.0 |
| 29R-2, 47–48 | 658.87 | 0.72 | 6.0 | | | | | | |
| 29R-3, 24–25 | 660.14 | 4.27 | 35.6 | 4.56 | 0.29 | 0.06 | 0.07 | 4.8 | 4.0 |
| 30R-1, 107–108 | 667.67 | 0.40 | 3.3 | 1.16 | 0.76 | 0.09 | 0.70 | 8.5 | 1.1 |
| 30R-2, 108–109 | 669.18 | 0.23 | 1.9 | | | | | | |
| 30R-1, 80–81 | 671.90 | 0.36 | 3.0 | 0.92 | 0.56 | 0.08 | 0.00 | 7.2 | |
| 31R-1, 18–19 | 676.38 | 0.42 | 3.5 | 0.99 | 0.57 | 0.08 | 0.00 | 7.3 | |
| 31R-2, 39–40 | 678.09 | 0.33 | 2.7 | | | | | | |
| 31R-4, 101–102 | 681.71 | 0.22 | 1.8 | 0.78 | 0.56 | 0.07 | 0.32 | 8.0 | 1.8 |
| 32R-1, 47–48 | 686.27 | 2.00 | 16.7 | 2.66 | 0.66 | 0.07 | 0.00 | 9.1 | |
| 32R-2, 132–133 | 688.62 | 0.39 | 3.2 | | | | | | |
| 32R-5, 119–120 | 692.99 | 0.20 | 1.7 | 0.88 | 0.68 | 0.07 | 0.58 | 9.6 | 1.2 |
| 33R-1, 39–40 | 695.79 | 0.45 | 3.7 | 1.08 | 0.63 | 0.07 | 0.48 | 8.6 | 1.3 |
| 34R-1, 122–123 | 706.22 | 0.40 | 3.3 | 1.09 | 0.69 | 0.05 | 0.28 | 13.1 | 2.5 |
| 35R-2, 90–91 | 717.00 | 0.31 | 2.6 | 0.82 | 0.51 | 0.05 | 0.00 | 10.2 | |
| 35R-4, 90–91 | 720.00 | 0.38 | 3.2 | 0.92 | 0.54 | 0.05 | 0.00 | 10.1 | |
| 35R-6, 90–91 | 723.00 | 0.32 | 2.7 | | | | | | |
| 37R-2, 50–51 | 735.80 | 0.35 | 2.9 | 1.03 | 0.68 | 0.05 | 0.50 | 13.2 | 1.4 |
| 37R-5, 50–51 | 740.30 | 0.18 | 1.5 | | | | | | |
| 37R-6, 2–3 | 741.32 | 3.72 | 31.0 | 4.34 | 0.62 | 0.08 | 0.38 | 7.7 | 1.6 |
| 38R-1, 120–121 | 744.60 | 0.78 | 6.5 | 1.35 | 0.57 | 0.07 | 0.42 | 8.3 | 1.3 |
| 38R-4, 120–121 | 749.10 | 0.15 | 1.2 | 0.70 | 0.55 | 0.05 | 0.42 | 12.2 | 1.3 |
| 39R-2, 41–42 | 754.91 | 0.10 | 0.8 | 0.52 | 0.42 | 0.08 | 0.34 | 5.3 | 1.2 |
| 39R-4, 41–42 | 757.91 | 0.40 | 3.3 | 1.21 | 0.81 | 0.14 | 0.00 | 5.8 | |
| 41R-2, 111–112 | 774.81 | 0.09 | 0.7 | 0.63 | 0.54 | 0.11 | 0.35 | 5.1 | 1.6 |
| 41R-4, 111–112 | 777.81 | 0.25 | 2.1 | | | | | | |
| 41R-5, 111–112 | 779.31 | 0.38 | 3.2 | 1.03 | 0.65 | 0.14 | 0.16 | 4.6 | 4.2 |
| 42R-3, 92–93 | 785.72 | 0.41 | 3.4 | 1.07 | 0.66 | 0.12 | 0.53 | 5.4 | 1.3 |
| 42R-5, 109–110 | 788.89 | 0.55 | 4.6 | 0.97 | 0.42 | 0.09 | 0.00 | 4.5 | |
| 43R-2, 26–27 | 793.16 | 0.16 | 1.3 | | | | | | |
| 44R-1, 18–19 | 801.28 | 0.37 | 3.1 | 0.86 | 0.49 | 0.12 | 0.00 | 4.2 | |
| 44R-3, 94–95 | 805.04 | 0.33 | 2.7 | 1.09 | 0.76 | 0.13 | 0.12 | 6.0 | 6.1 |
| 45R-2, 85–86 | 813.05 | 0.18 | 1.5 | 0.71 | 0.53 | 0.10 | 0.11 | 5.1 | 4.9 |
| 45R-5, 86–87 | 817.56 | 0.23 | 1.9 | 0.84 | 0.61 | 0.11 | 0.37 | 5.5 | 1.7 |
| 46R-1, 120–121 | 821.50 | 0.31 | 2.6 | 1.02 | 0.71 | 0.11 | 0.31 | 6.5 | 2.3 |
| 47R-1, 9–10 | 829.99 | 0.28 | 2.3 | 0.87 | 0.59 | 0.10 | 0.00 | 5.9 | |
| 47R-2, 55–56 | 831.95 | 0.12 | 1.0 | | | | | | |
| 47R-2, 148–149 | 832.88 | 0.12 | 1.0 | 0.80 | 0.68 | 0.11 | 0.32 | 6.0 | 2.2 |
| 48R-1, 35–36 | 839.85 | 0.16 | 1.3 | 0.98 | 0.82 | 0.13 | 0.25 | 6.3 | 3.3 |
| 48R-2, 35–36 | 841.35 | 0.25 | 2.1 | 1.07 | 0.82 | 0.15 | 0.00 | 5.6 | |
| 49R-1, 24–25 | 849.44 | 0.33 | 2.7 | | | | | | |
| 49R-1, 80–81 | 850.00 | 0.61 | 5.1 | 1.20 | 0.59 | 0.11 | 0.75 | 5.3 | 0.8 |
| 50R-2, 27–28 | 860.57 | 0.51 | 4.2 | 1.06 | 0.55 | 0.10 | 0.72 | 5.6 | 0.8 |
| 50R-4, 116–117 | 864.46 | 0.57 | 4.7 | 1.21 | 0.64 | 0.10 | 0.67 | 6.2 | 0.9 |
| 51R-1, 22–23 | 868.62 | 0.39 | 3.2 | 1.01 | 0.62 | 0.12 | 0.00 | 5.2 | |
| 51R-5, 21–22 | 874.43 | 0.32 | 2.7 | 0.95 | 0.63 | 0.11 | 0.22 | 5.8 | 2.9 |
| 51R-7, 23–24 | 877.25 | 0.29 | 2.4 | | | | | | |
| 52R-2, 120–121 | 880.80 | 0.31 | 2.6 | 1.00 | 0.69 | 0.12 | 0.26 | 5.9 | 2.6 |
| 52R-4, 113–114 | 883.73 | 0.34 | 2.8 | 1.05 | 0.71 | 0.12 | 0.35 | 6.1 | 2.0 |
| 52R-7, 12–13 | 887.22 | 0.27 | 2.2 | | | | | | |
| 53R-2, 133–134 | 890.43 | 0.30 | 2.5 | 0.99 | 0.69 | 0.12 | 0.33 | 5.9 | 2.1 |
| 53R-5, 38–39 | 893.98 | 0.32 | 2.7 | 1.07 | 0.75 | 0.12 | 0.29 | 6.5 | 2.6 |
| 54R-1, 65–66 | 897.95 | 0.55 | 4.6 | 1.32 | 0.77 | 0.14 | 0.28 | 5.7 | 2.8 |
| 55R-1, 66–67 | 907.56 | 0.10 | 0.8 | 1.01 | 0.91 | 0.14 | 1.27 | 6.5 | 0.7 |
| 57R-1, 66–67 | 926.76 | 0.14 | 1.2 | 1.36 | 1.22 | 0.16 | 2.81 | 7.6 | 0.4 |
| 58R-1, 66–67 | 936.36 | 0.23 | 1.9 | 1.22 | 0.99 | 0.15 | 2.66 | 6.6 | 0.4 |
| 59R-2, 117–118 | 947.97 | 0.26 | 2.2 | 1.30 | 1.04 | 0.16 | 1.23 | 6.5 | 0.8 |
| 59R-3, 25–26 | 948.55 | 2.09 | 17.4 | 2.91 | 0.82 | 0.15 | 0.75 | 5.5 | 1.1 |
| 60R-1, 67–68 | 955.67 | 0.34 | 2.8 | 1.56 | 1.22 | 0.16 | 2.23 | 7.8 | 0.5 |
| | Average: | 0.58 | 4.8 | 1.40 | 0.80 | 0.10 | 0.34 | 7.9 | 4.4 |
| | Maximum: | 4.47 | 37.2 | 5.72 | 1.88 | 0.17 | 2.81 | 18.3 | 20.2 |
| | Minimum: | 0.09 | 0.7 | 0.41 | 0.18 | 0.01 | 0.00 | 2.6 | 0.3 |

Notes: IC = inorganic carbon, $CaCO_3$ = calcium carbonate, TC = total carbon, TOC = total organic carbon, TN = total nitrogen, TS = total sulfur, C/N = total organic carbon/total nitrogen ratio, and C/S = total organic carbon/total sulfur ratio.

0.3–0.4 g/cm$^3$, respectively, and increased natural gamma radiation values. The latter would indicate a higher clay content in the debris-flow deposits relative to other deposits above and below.

The two lowermost geotechnical units indicate a different depositional environment. This is also observed in the change of seismic character across seismic Reflector R6 (see "Seismic Stratigraphy" section, this chapter). The sediments are dominated by a sandy lithology with occasional, thinner more clayey intervals, in particular towards the lower part of geotechnical Unit G3, where these intervals are represented by low velocities (Fig. 25). Most often, however, the less sandy intervals seem to be represented by nonrecovered intervals, or intervals where no physical properties were measured because of sample disturbance. Where measurable, the physical properties of geotechnical Unit G4 show the same characteristics as the more clayey intervals of Unit G3, including poor recovery and increased sample disturbance. As documented by the lithological stud-

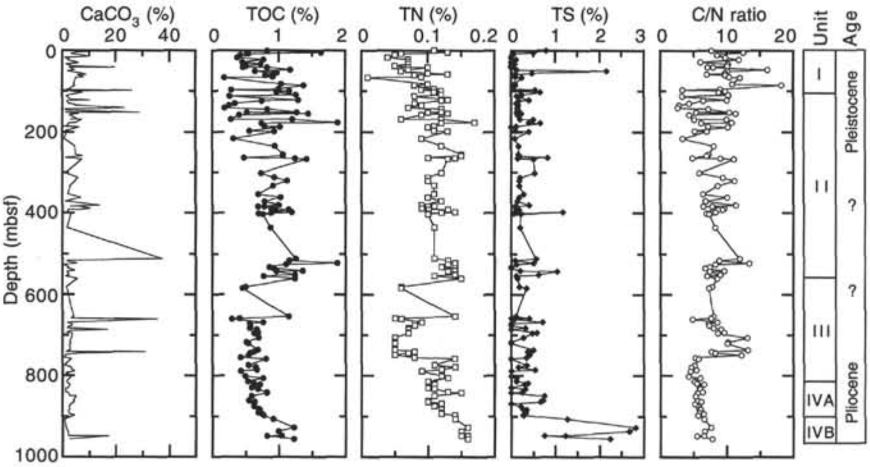


Figure 21. Calcium carbonate ($CaCO_3$), total organic carbon (TOC), total nitrogen (TN), and total sulfur (TS) contents, TOC/TN (C/N) ratio, lithostratigraphic units, and age at Site 986.

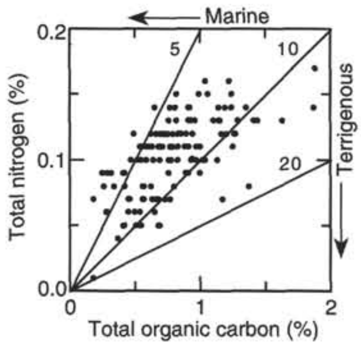


Figure 22. Total organic carbon vs. total nitrogen at Site 986. Lines show C/N ratios of 5, 10, and 20.

ies, the physical properties of this unit reflect a transition from a mud-dominated depositional environment in Unit G4, to an environment with an increased sand component in Unit G3.

In summary, the physical properties measured at Site 986 demonstrate significant variations in depositional processes on the Svalbard Margin. In particular the boundary between geotechnical Units G2 and G3, which correlates with the most distinct change in seismic character, appears as an important shift in depositional environment. Given an age estimate of <3.6 Ma for the lowermost cored sediments (see "Biostratigraphy" section, this chapter), variations in the glacial regime of the adjacent Svalbard archipelago and the Barents Sea continental shelf appear as the most likely driving mechanism. This site has a high potential for additional studies of physical properties.

### Heat Flow

The main objective of the downhole temperature measurements at Site 986 was to add to the heat-flow database of this region, and thereby improve the interpretation of this tectonically complicated and poorly understood region. Due to instrumental problems, thermal conductivity measurements were delayed by 10 days, but were eventually measured on 12-cm whole-round core samples cut from the 50-cm level in the three core sections nearest to the downhole temperature measurements. The thermal conductivity measurements were not normalized for the five different needle probes by the standards for each run.

The measurements were of good quality, with a very low noise level, and yielded a thermal gradient of 151.9°C/km (Figs. 26, 27). Extrapolation of the temperature curve gives a bottom water temperature of –0.93°C, which is in good correspondence with physical oceanographic measurements (CTD-casts) in this area (S. Osterhuis, pers. comm., 1996). Using an average measured thermal conductivity of 1.156 W/(m·K) provides a heat-flow estimate of 175.6 mW/m$^2$ at Site 986. A recently published heat-flow map for the northern Norwegian-Greenland Sea (Crane and Sundvor, 1995) shows the area adjacent to Site 986 to have a heat flow between 100 and 125 mW/m$^2$. The high measured value indicates a relatively young crust at Site 986. This is consistent with middle Pliocene age estimates for the lower part of Hole 986D, approximately 100–150 m above acoustic basement (see "Biostratigraphy" and "Paleomagnetism" sections, this chapter).

## WIRELINE LOGGING

### Operations

At Site 986, Hole 986C and a portion of Hole 986D were logged. In Hole 986C, the Quad combination (Quad combo), Formation MicroScanner (FMS), and the Geological High-resolution Magnetometer (GHMT) tools were deployed (Table 19). Due to difficult borehole conditions encountered in Hole 986D, only the Quad tool string was run (Table 20). Hole 986C was completed at ~408 mbsf (2471 mbrf) and the hole was conditioned by a "wiper trip" to remove drilling debris prior to logging. Hole 986D was drilled to a total depth of ~965 mbsf. The pipe was placed at 325 mbsf to allow for an overlapped section so the logs from Holes 986C and 986D could be combined. The wiper trip for Hole 986D was very difficult and took almost 17 hours to complete. Due to poor hole conditions, only two short sections, 325–408 mbsf and 438–490 mbsf, were logged with the Quad tool string. The second lower section was logged after removing tools and advancing drill pipe to ~438 mbsf to get past a bridge between 410 and 420 mbsf. Logging in Hole 986D was terminated after the tool stopped again at another bridge at 490 mbsf. See the "Explanatory Notes" chapter (this volume) and Borehole Research Group (1994) for complete description of all tool strings and associated acronyms.

Hole conditions during logging were quite variable. Caliper data from both the Quad and FMS tool strings in Hole 986C indicated that hole diameter varied between 20 and 35 cm over some sections of the interval of the hole containing large debris flows. However, several "washed-out" zones in excess of 40–50 cm occurred between the large debris-flow layers. Conditions in Hole 986D appeared to be worse with even more variable hole rugosity and washed-out zones of >45 cm on average. The natural gamma-ray tool (NGT) was used to determine the mudline in Hole 986C through the drill pipe during the last run of the Quad tool string. The mudline was measured at ~2062.5 mbrf by running NGT very slowly near estimated driller's depth and recording where a spike occurred when seawater was encountered. This mudline value was used to depth-shift all raw data from the three tool strings to mbsf from mbrf. The difference between driller's estimated depth (2063 mbrf) and mudline measurement

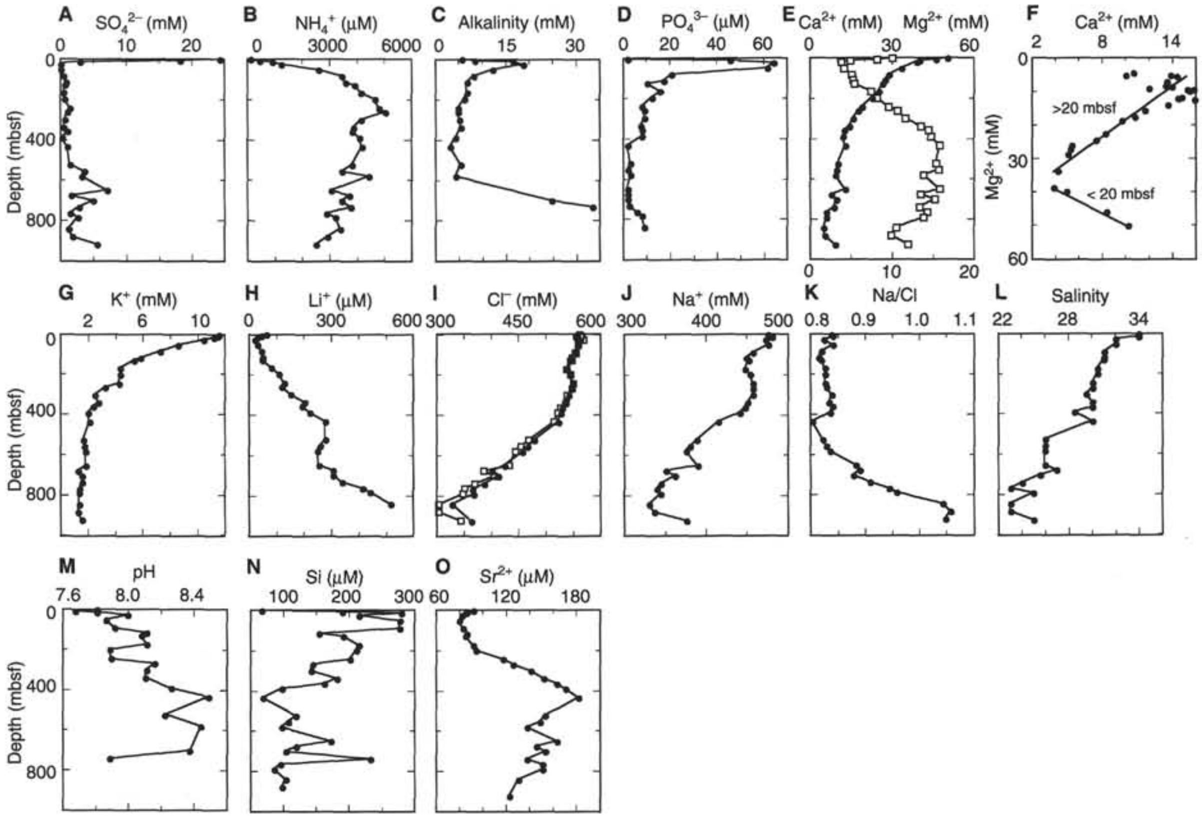


Figure 23. Vertical profiles of sulfate (**A**), ammonium (**B**), alkalinity (**C**), phosphate (**D**), calcium and magnesium (**E**), calcium vs. magnesium (**F**), potassium (**G**), lithium (**H**), chloride determined by titration (solid circles) and ion chromatography (open squares) (**I**), sodium determined by ion chromatography (**J**), Na/Cl (**K**), salinity (**L**), pH (**M**), silica (**N**), and strontium (**O**) at Site 986.

**Table 12. Composition of interstitial waters at Hole 986B, 986C, and 986D.**

| Core, section, interval (cm) | Depth (mbsf) | Na (mM) | K (mM) | Li (µM) | Mg (mM) | Ca (mM) | Sr (µM) | Cl (mM) | $SO_4$ (mM) | $NH_4$ (µM) | Si (µM) | $PO_4$ (µM) | pH | Alkalinity (mM) | Salinity |
|---|---|---|---|---|---|---|---|---|---|---|---|---|---|---|---|
| 162-986B- | | | | | | | | | | | | | | | |
| 1H-2, 145–150 | 2.95 | 476 | 11.6 | 65 | 50.4 | 10.1 | 92 | 557 | 24.4 | 87 | 66 | 2.1 | 7.80 | 5.565 | 34.0 |
| 162-986C- | | | | | | | | | | | | | | | |
| 1H-5, 145–150 | 7.45 | 480 | 11.5 | 42 | 46.3 | 8.2 | 87 | 560 | 18.4 | 424 | 189 | 2.1 | 7.67 | 8.474 | 34.0 |
| 2H-4, 145–150 | 13.45 | 481 | 11.2 | 28 | 40.1 | 4.9 | 85 | 557 | 3.0 | 890 | 281 | 46.0 | 7.80 | 16.755 | 34.0 |
| 3H-4, 145–150 | 22.95 | 474 | 10.6 | 19 | 39.0 | 3.8 | 82 | 565 | 0.0 | 1241 | 215 | 64.8 | 7.99 | 18.890 | 32.0 |
| 6H-4, 145–150 | 51.45 | 477 | 8.7 | 32 | 33.7 | 4.1 | 80 | 560 | 0.0 | 2604 | 278 | 62.0 | 7.86 | 12.310 | 32.0 |
| 10X-4, 145–150 | 86.55 | 458 | 7.3 | 46 | 28.8 | 5.0 | 83 | 556 | 0.4 | 3464 | 278 | 20.6 | 7.91 | 8.105 | 31.0 |
| 13X-3, 145–150 | 113.95 | 450 | 5.9 | 47 | 27.3 | 5.2 | 86 | 546 | 0.8 | 3614 | 155 | 17.5 | 8.11 | 6.600 | 31.0 |
| 15X-2, 145–150 | 131.24 | 453 | 5.4 | 50 | 26.3 | 5.3 | 85 | 546 | 0.6 | 3930 | 192 | 10.3 | 8.08 | | 31.0 |
| 19X-2, 140–150 | 170.30 | 448 | 4.4 | 80 | 24.8 | 7.4 | 92 | 540 | 0.4 | 4159 | 215 | 15.8 | 8.11 | 6.750 | 30.5 |
| 22X-2, 140–150 | 199.20 | 454 | 4.3 | 108 | 22.7 | 8.2 | 94 | 546 | 0.6 | 4704 | 211 | 12.3 | 7.88 | 6.150 | 30.5 |
| 27X-1, 140–150 | 245.70 | 458 | 4.3 | 127 | 19.0 | 9.6 | 117 | 550 | 1.4 | 4819 | 202 | 7.8 | 7.89 | 4.775 | 30.0 |
| 30X-2, 140–150 | 266.50 | 458 | 3.2 | 121 | 17.5 | 10.7 | 126 | 547 | 1.0 | 5084 | 144 | 8.9 | 8.16 | 4.739 | 30.0 |
| 34X-1, 140–150 | 303.50 | 457 | 2.5 | 151 | 15.6 | 11.6 | 142 | 542 | 0.7 | 4181 | 142 | 9.2 | 8.11 | 5.019 | 29.5 |
| 37X-6, 140–150 | 338.69 | 451 | 2.8 | 203 | 14.1 | 13.5 | 153 | 539 | 0.4 | 3880 | 181 | 7.2 | 8.10 | 5.260 | 30.0 |
| 40X-2, 140–150 | 362.70 | 448 | 2.4 | 196 | 12.5 | 14.4 | 164 | 530 | 1.0 | 3844 | 163 | 7.8 | | | 30.0 |
| 43X-2, 140–150 | 391.60 | 442 | 2.0 | 225 | 11.9 | 14.7 | 171 | 528 | 0.3 | 4131 | 98 | 8.1 | 8.26 | 4.188 | 28.5 |
| 162-986D- | | | | | | | | | | | | | | | |
| 6R-1, 135–150 | 437.25 | 415 | 2.1 | 280 | 12.8 | 15.9 | 182 | 523 | 1.1 | 4229 | 68 | 1.9 | 8.49 | 3.195 | 30.0 |
| 15R-4, 135–150 | 528.15 | 389 | 1.6 | 279 | 9.9 | 15.4 | 154 | 480 | 1.5 | 3827 | 119 | 3.1 | 8.22 | 5.248 | 26.0 |
| 18R-4, 135–150 | 556.95 | 381 | 1.7 | 259 | 9.6 | 15.8 | 149 | 468 | 3.7 | 3483 | 108 | 1.6 | | | 26.0 |
| 21R-2, 135–150 | 582.85 | 375 | 1.8 | 253 | 9.0 | 13.9 | 138 | 457 | 3.3 | 4441 | 97 | 2.7 | 8.44 | 4.328 | 26.0 |
| 28R-4, 140–150 | 653.30 | 390 | 1.9 | 255 | 12.9 | 15.9 | 164 | 425 | 7.1 | 3081 | 171 | 1.6 | | | 26.0 |
| 31R-3, 140–150 | 680.60 | 350 | 1.3 | 308 | 7.4 | 13.5 | 146 | 400 | 1.7 | 3725 | 119 | 2.1 | | | 27.0 |
| 34R-1, 135–150 | 706.35 | 362 | 1.6 | 311 | 9.5 | 15.2 | 154 | 413 | 5.0 | 3483 | 104 | 1.6 | 8.37 | 24.932 | 25.5 |
| 37R-5, 135–150 | 741.15 | 344 | 1.6 | 342 | 8.4 | 13.3 | 138 | 386 | 2.9 | 3783 | 232 | 2.5 | 7.88 | 33.809 | 24.0 |
| 40R-4, 135–150 | 768.45 | 340 | 1.4 | 416 | 5.6 | 14.4 | 151 | 366 | 1.5 | 2913 | 95 | 5.6 | | | 23.0 |
| 43R-1, 135–150 | 792.75 | 344 | 1.3 | 444 | 5.6 | 13.8 | 151 | 369 | 2.6 | 3250 | 85 | 7.7 | | | 25.0 |
| 49R-2, 35–50 | 846.77 | 330 | 1.4 | 523 | 4.8 | 10.6 | 130 | 328 | 1.1 | 3425 | 104 | 8.9 | | | 23.0 |
| 52R-4, 135–150 | 883.95 | 336 | 1.3 | | 5.3 | 9.9 | | | 1.9 | 2943 | 97 | | | | 23.0 |
| 57R-1, 130–150 | 927.40 | 375 | 1.6 | | 9.1 | 12.0 | 123 | 363 | 5.6 | 2526 | | | | | 25.0 |

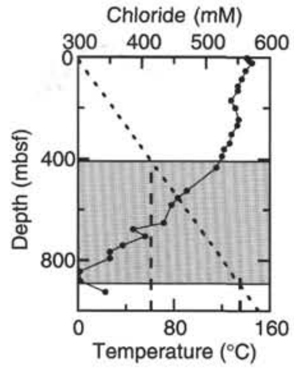


Figure 24. Chloride concentration (line with solid circles) and geothermal gradient (dashed line) extrapolated from temperature measurements between 26 and 63 mbsf (see "Physical Properties" section, this chapter). The shaded area denotes the depth range which encompasses the predicted temperatures between 60° and 135°C. Within this zone, the transformation of smectite to illite is expected to occur with a concomitant release of water, which dilutes interstitial waters, as marked by decreasing chloride concentrations.

(2062.5 mbrf) was only 0.5 m. Tables 19 and 20 provide a complete summary of logging operations conducted at this site.

## Core-to-Log Data Comparisons

### *Magnetic Susceptibility*

The magnetic susceptibility log data obtained by the GHMT at this site correlate well with the magnetic susceptibility measured on the cores (Fig. 28). Although core recovery was only ~55% between 80 and 400 mbsf, intervals with both core and log data from Hole 986C correlate well.

Susceptibility measurements range between 30 and 600 SI units with no obvious cyclical pattern. The overall pattern is fairly random, with abrupt changes in values which may correspond to depositional processes and/or sediment type (i.e., debris flow, turbidite, or hemipelagic sediment).

The sections of core corresponding to inferred debris-flow layers, 155–175, 230–255, and 290–330 mbsf typically show lower magnetic susceptibility. In addition, the magnetic susceptibility readings are uniform across the layers, making it easy to establish the upper and lower boundaries of flows. The reasons for this are not clear but it could be related to (1) sediment source of debris, (2) the loss of fine detrital material containing higher magnetite content, and/or (3) the debris flow's coarser character as shown in FMS imaging may mean that by volume, the magnetic susceptibility values are being diluted by large numbers of clasts and other coarse sediments.

### *Velocity*

Sonic log data were collected in Holes 986C and 986D by the Long-Spaced Sonic (LSS) tool, which was run as part of the standard Quad tool string.

In Hole 986C, sonic log data were collected from the interval 88–359 mbsf, and in Hole 986D from intervals 306–381 and 425–463 mbsf. Compressional-wave transit-time measurements were recorded for source-receiver spacings of 8, 10, and 12 ft (2.438, 3.048, and 3.658 m). Measurements at 10-ft spacing were recorded by two separate source-receiver pairs, resulting in a total of four different transit-time measurements at each depth.

To a greater or lesser extent, the individual data streams from the various source-receiver pairs are all affected by noise spikes. The data from Hole 986D are more severely affected by these problems than the data from Hole 986C. Virtually all the noise spikes affecting the sonic log data from Hole 986C occurred in the lowermost 45 m of the logged interval. Noise spikes were edited out of the data from the 10-ft and 12-ft source-receiver spacings and a depth-derived, borehole-compensated sonic log (DTLF) was recalculated from these data. For the deeper interval logged in Hole 986D, only a small number of data points remain after editing. Figure 29A shows a comparison of the recalculated log with the original DTLF transit times computed during logging.

The recalculated log shows that a steady decrease in interval transit time (increase in velocity) is interrupted by several 10- to 20-m-thick layers with sharp boundaries and anomalous high velocities. The downhole velocities are shown in Figure 29B, together with laboratory measurements from the same holes and an empirical velocity-vs.-depth functions for deep-sea turbidite successions. Velocities on the recalculated sonic log are close to those on the empirical function for turbidites of Hamilton (1979), except in the 10–20-m-thick high-velocity layers. These layers are thought to be large debris flows (see "Lithostratigraphy" section, this chapter). Above 360 mbsf the log velocities are considerably higher than the two laboratory measurements that were made between 30 and 360 mbsf. Laboratory measurements were not possible throughout this interval because of very high acoustic signal attenuation in the core samples, which is thought to be a result of gas expansion during recovery (see "Physical Properties" section, this chapter). It is expected that the seismic velocity measured in situ by logging should be significantly higher than laboratory measurements on the unlithified cores because of core expansion. Below 360 mbsf, there are few depths at which there are both recalculated sonic log data and laboratory measurements, but where they do both exist, the velocities are similar. This may indicate that below this depth the cores were sufficiently lithified not to expand significantly during recovery.

### *Density*

Bulk density data in Holes 986C and 986D were collected by the Hostile-environment Litho-Density Tool (HLDT), which was run as part of the standard Quad tool string. In addition to making the standard bulk density (RHOB) and photoelectric effect measurements (PEF) every 15 cm, the tool was run in high-resolution mode, producing additional bulk density (HRHO) and photoelectric effect (HPEF) data at 2.5-cm spacing. In Hole 986C density log data were collected from the interval 86–374 mbsf, and in Hole 986D from the intervals 305–395 mbsf and 424–477 mbsf. The reliability of the density log data is reduced in the uppermost 5–15 m of each logging run because the caliper was closed before pulling the tool into the drill pipe.

In both Holes 986C and 986D the caliper (Fig. 29C) showed that hole diameter was irregular and many intervals were washed out. In many of the washed-out intervals anomalously low density readings were obtained, indicating that the density tool was probably not in consistent contact with the borehole wall. The wireline log bulk density data are shown with GRAPE and gravimetric wet bulk density data from cores in Figure 29C. Gravimetric wet bulk density measurements are all close to the higher end of the range of values on the density log, which supports the view that the lower values on the log are suspect. The high-velocity layers interpreted as debris flows (see above, and "Lithostratigraphy" section, this chapter) are also observed on the density log as high-density layers. The borehole diameter is almost constant across these layers, typically no larger than the diameter of the drill bit, so the log density measurements are considered to be reliable.

## FMS Imaging

FMS imaging in Holes 986C and 986D revealed a stacked sequence of debris flows, small turbidite layers, and occasional hemipelagic sediments between 80 and 500 mbsf. This whole interval is bounded by seismic Reflectors R2 (70–80 mbsf) and 6 (~560 mbsf)

**Table 13. Index properties of samples from Holes 986C and 986D.**

| Core, section, interval (cm) | Depth (mbsf) | Water content (wet %) | Water content (dry %) | Wet bulk density Method C (g/cm$^3$) | Grain density Method C (g/cm$^3$) | Dry bulk density Method C (g/cm$^3$) | Porosity Method C (%) | Void ratio Method C |
|---|---|---|---|---|---|---|---|---|
| 162-986C- | | | | | | | | |
| 1H-3, 105–107 | 4.05 | 30.9 | 44.7 | 1.76 | 2.61 | 1.22 | 53.3 | 1.1 |
| 1H-4, 65–67 | 5.15 | 37.6 | 60.2 | 1.66 | 2.65 | 1.04 | 60.8 | 1.6 |
| 1H-5, 17–19 | 6.17 | 43.0 | 75.5 | 1.60 | 2.77 | 0.91 | 67.1 | 2.0 |
| 1H-5, 82–84 | 6.82 | 39.0 | 63.9 | 1.64 | 2.65 | 1.00 | 62.4 | 1.7 |
| 2H-1, 34–36 | 7.84 | 42.3 | 73.2 | 1.60 | 2.70 | 0.92 | 65.9 | 1.9 |
| 2H-1, 130–132 | 8.80 | 34.4 | 52.5 | 1.70 | 2.60 | 1.11 | 57.1 | 1.3 |
| 2H-2, 11–13 | 9.11 | 31.4 | 45.8 | 1.78 | 2.67 | 1.22 | 54.5 | 1.2 |
| 2H-2, 115–117 | 10.15 | 37.6 | 60.3 | 1.68 | 2.72 | 1.05 | 61.6 | 1.6 |
| 2H-3, 62–64 | 11.12 | 37.7 | 60.4 | 1.67 | 2.72 | 1.04 | 61.6 | 1.6 |

**Only part of this table is reproduced here. The entire table appears on the CD-ROM (back pocket).**

**Table 14. Compressional-wave velocity measurements from Holes 986C and 986D.**

| Core, section, interval (cm) | Depth (mbsf) | Velocity (m/s) | Temperature (°C) | Direction |
|---|---|---|---|---|
| 162-986C- | | | | |
| 1H-1, 12 | 0.12 | 1528 | 19.6 | z |
| 1H-1, 33 | 0.33 | 1494 | 20.0 | z |
| 1H-1, 89 | 0.89 | 1491 | 20.0 | z |
| 1H-2, 76 | 2.26 | 1503 | 20.0 | z |
| 1H-2, 102 | 2.52 | 1538 | 20.1 | z |
| 1H-3, 47 | 3.47 | 1510 | 20.0 | z |
| 1H-3, 108 | 4.08 | 1548 | 20.0 | z |
| 1H-4, 68 | 5.18 | 1507 | 19.6 | z |
| 1H-5, 16 | 6.16 | 1499 | 19.7 | z |

Note: For explanation of measurement directions, see "Explanatory Notes" chapter (this volume).

**Only part of this table is reproduced here. The entire table appears on the CD-ROM (back pocket).**

**Table 15. Undrained shear strength measurements from Hole 986C.**

| Core, section, interval (cm) | Depth (mbsf) | Undrained shear strength (kPa) | Spring no. | Penetrometer (kPa) |
|---|---|---|---|---|
| 162-986C- | | | | |
| 1H-1, 10 | 0.10 | 14.8 | 1 | |
| 1H-1, 88 | 0.88 | 2.0 | 1 | |
| 1H-2, 74 | 2.24 | 10.0 | 1 | |
| 1H-2, 101 | 2.51 | 3.7 | 1 | |
| 1H-3, 46 | 3.46 | 15.3 | 1 | |
| 1H-3, 107 | 4.07 | 2.6 | 1 | |
| 1H-4, 67 | 5.17 | 3.2 | 1 | |
| 1H-5, 15 | 6.15 | 15.4 | 1 | |
| 1H-5, 81 | 6.81 | 6.0 | 1 | |

**Only part of this table is reproduced here. The entire table appears on the CD-ROM (back pocket).**

and corresponds roughly to lithostratigraphic Unit II (see "Lithostratigraphy" and "Seismic Stratigraphy" sections, this chapter). There are several large debris flows (10–25 m thick) which stand out dramatically on almost all the wireline log responses.

These thick debris-flow layers correspond to small borehole diameters and areas of very good FMS images. They are also fairly homogenous and very coarse, with abundant clasts. There appears to be a coarse internal structure within the largest layers between 230 and 255 mbsf and between 290 and 330 mbsf. This structure is indicated by a sharp base, roughly fining upward and overlain by another clast filled section; this is then repeated. FMS images between layers were often derived from only 1 or 2 of the FMS pads in contact with the hole as the softer sediments were typically washed out. However, there were short intervals of layered sedimentary (i.e., 105–125 mbsf) sequence with interspersed resistive units that might be small turbidites.

**Table 16. Fall-cone penetrometer undrained shear strength measurements from Hole 986C.**

| Core, section, interval (cm) | Depth (mbsf) | Cone type | Penetration (mm) | Undrained shear strength (kPa) |
|---|---|---|---|---|
| 162-986C- | | | | |
| 1H-1, 18 | 0.18 | 60/60 | 9.0 | 1.8 |
| 1H-1, 102 | 1.02 | 60/60 | 6.5 | 3.4 |
| 1H-2, 81 | 2.31 | 60/60 | 8.0 | 2.3 |
| 1H-2, 107 | 2.57 | 60/60 | 5.0 | 5.9 |
| 1H-3, 55 | 3.55 | 60/60 | 5.0 | 5.9 |
| 1H-3, 100 | 4.00 | 60/60 | 6.0 | 4.1 |
| 1H-4, 75 | 5.25 | 60/60 | 6.5 | 3.4 |
| 1H-5, 10 | 6.10 | 60/60 | 4.0 | 9.2 |
| 1H-5, 89 | 6.89 | 60/60 | 4.0 | 9.2 |

**Only part of this table is reproduced here. The entire table appears on the CD-ROM (back pocket).**

The debris-flow layers stood out in both the log velocity and density measurements discussed above. In addition, the natural gamma-ray and especially the resistivity log data depict these layers very clearly (Fig. 30A, -B). The resistivity log responds primarily to the water content of the sediments with higher resistivity corresponding to lower water content. The high resistivity, coarse, poorly sorted sediments, low water content, and little internal structure are all consistent with a debris-flow interpretation.

### Downhole Temperature Measurements

Borehole fluid temperature measurements were recorded in Hole 986C using the Lamont temperature logging tool (TLT). The TLT was run at the base of the Quad tool string, which was the first logging run. A downhole and an uphole profile were acquired. Figure 31 shows temperatures for the downhole and the uphole runs. The maximum recorded temperature at 400 mbsf in Hole 986C was 15.8°C. This value is well below the ~60°C expected from the 150°/km gradient estimated from downhole temperature measurements in the sediments (see "Physical Properties" section, this chapter). The low temperatures are probably due to circulation of cold seawater used to clean drilling debris from the hole prior to logging.

## SEISMIC STRATIGRAPHY

The proposed site SVAL-1 (Site 986) was located on a multichannel seismic (MCS) Line BEL-4 acquired in 1987 by the Norwegian Polar Institute (NPI) and the University of Bergen, using the commercial seismic vessel *Mobil Search*. Additional high-resolution, sin-

Table 17. Summary statistics of the physical properties for the geotechnical units and subunits at Site 986.

| | Water content (%) | | | Porosity (%) | | |
|---|---|---|---|---|---|---|
| Unit | Min. | Max. | Mean | Min. | Max. | Mean |
| G1A | 17.1 | 43.0 | 32.1 | 34.6 | 67.1 | 54.9 |
| G1B | 19.9 | 35.4 | 27.6 | 40.8 | 58.4 | 49.6 |
| G2 | 12.4 | 26.6 | 19.6 | 27.3 | 48.9 | 38.5 |
| G3A | 14.0 | 22.1 | 18.3 | 29.5 | 42.6 | 36.7 |
| G3B | 9.4 | 20.6 | 12.6 | 21.0 | 39.9 | 27.1 |
| G4 | 11.9 | 16.8 | 13.6 | 25.6 | 34.9 | 28.8 |
| | Void ratio | | | Wet bulk density (g/cm$^3$) | | |
| Unit | Min. | Max. | Mean | Min. | Max. | Mean |
| G1A | 0.50 | 2.00 | 1.26 | 1.58 | 2.07 | 1.77 |
| G1B | 0.70 | 1.40 | 1.00 | 1.68 | 2.10 | 1.85 |
| G2 | 0.38 | 1.00 | 0.64 | 1.87 | 2.29 | 2.03 |
| G3A | 0.42 | 0.74 | 0.58 | 1.97 | 2.17 | 2.06 |
| G3B | 0.27 | 0.66 | 0.37 | 1.98 | 2.32 | 2.21 |
| G4 | 0.34 | 0.54 | 0.41 | 2.12 | 2.24 | 2.18 |
| | Dry bulk density (g/cm$^3$) | | | Grain density (g/cm$^3$) | | |
| Unit | Min. | Max. | Mean | Min. | Max. | Mean |
| G1A | 0.91 | 1.72 | 1.21 | 2.60 | 2.79 | 2.68 |
| G1B | 1.09 | 1.68 | 1.34 | 2.53 | 2.84 | 2.67 |
| G2 | 1.38 | 1.97 | 1.63 | 2.57 | 3.41 | 2.65 |
| G3A | 1.54 | 1.86 | 1.68 | 2.56 | 2.82 | 2.66 |
| G3B | 1.57 | 2.09 | 1.93 | 2.55 | 2.73 | 2.64 |
| G4 | 1.78 | 1.96 | 1.88 | 2.58 | 2.73 | 2.64 |
| | Velocity (m/s) | | | Vane strength (kPa) | | |
| Unit | Min. | Max. | Mean | Min. | Max. | Mean |
| G1A | 1423 | 1694 | 1520 | 2.0 | 39.3 | 19.3 |
| G1B | 1533 | 1533 | 1533 | 16.7 | 101.1 | 50.2 |
| G2 | 1545 | 2649 | 1844 | 36.1 | 129.0 | 88.0 |
| G3A | 1752 | 3104 | 1917 | | | |
| G3B | 1886 | 2704 | 2366 | | | |
| G4 | 2039 | 2697 | 2277 | | | |
| | Cone strength (kPa) | | | PP strength (kPa) | | |
| Unit | Min. | Max. | Mean | Min. | Max. | Mean |
| G1A | 1.8 | 61.8 | 29.4 | | | |
| G1B | 17.7 | 245.2 | 97.6 | | | |
| G2 | 61.8 | 245.2 | 167.5 | 62.0 | 207.0 | 133.0 |

Note: PP = pocket penetrometer.

Table 18. Thermal conductivity measurements from Hole 986C.

| Core, section, interval (cm) | Depth (mbsf) | Thermal conductivity (W/[m·K]) | Standard error (W/[m·K]) | Needle probe |
|---|---|---|---|---|
| 162-986C- | | | | |
| 4H-1, 53 | 26.33 | 1.338 | 0.00320 | 352 |
| 6H-1, 53 | 45.33 | 1.109 | 0.00267 | 353 |
| 8H-1, 53 | 64.33 | 1.205 | 0.00372 | 354 |
| 4H-1, 56 | 26.36 | 1.239 | 0.00245 | 354 |
| 6H-1, 56 | 45.36 | 1.213 | 0.00429 | 352 |
| 8H-1, 56 | 64.36 | 0.988 | 0.00203 | 353 |
| 4H-1, 59 | 26.39 | 1.133 | 0.00239 | 361 |
| 6H-1, 59 | 45.39 | 0.955 | 0.00625 | 360 |
| 8H-1, 59 | 64.39 | 1.251 | 0.00635 | 352 |
| 4H-1, 54 | 26.33 | 1.171 | 0.00321 | 360 |
| 6H-1, 54 | 45.33 | 1.515 | 0.00289 | 352 |
| 8H-1, 54 | 64.33 | 1.080 | 0.00289 | 361 |
| 4H-1, 57 | 26.37 | 1.070 | 0.00718 | 354 |
| 6H-1, 57 | 45.37 | 1.051 | 0.00219 | 361 |
| 8H-1, 57 | 64.37 | 1.141 | 0.00289 | 360 |
| 4H-1, 59 | 26.39 | 1.097 | 0.00303 | 360 |
| 6H-1, 59 | 45.39 | 1.187 | 0.00506 | 354 |
| 8H-1, 59 | 64.39 | 1.061 | 0.00461 | 353 |

gle-channel seismic coverage was provided by NPI during two cruises, in 1990 (NP90) and 1994 (NP94). SVAL-1 was located at the intersection between BEL-4 and Line NP94-5. Line BEL-4 is part of a regional seismic grid that covers the entire western Svalbard–Barents Sea continental margin. A regional seismic stratigraphy has recently been defined for this margin (Faleide et al., 1996) and a good seismic tie to the regional seismic grid was therefore considered of prime importance at SVAL-1, which is located approximately 5 km east of a prominent north-south-trending basement ridge.

Three important issues with respect to designing the present site survey were that the MCS Line BEL-4 did not have GPS navigation, the NP90 and NP94 SCS lines did not penetrate to basement, and an apparent debris flow seen in SCS Line NP94-5 had a thickness of more than 50 m at the proposed site, with its upper boundary shallower than 100 mbsf. The Leg 162 site survey consisted of five seismic lines (Fig. 32), of which three are the most important: Line 986-S1 duplicates the western part of Line BEL-4, crossing over the crest of the basement ridge, Line 986-S3 parallels Line BEL-4, 2.5 nmi to the south, and Line 986-S5 ties the two former lines, running roughly north-south, parallel to the ridge. Site 986 was chosen at shotpoint 1498 of Line 986-S5, 2.4 nmi south-southeast of the originally proposed SVAL-1. By moving the site to the new position, we avoided the thickest part of the shallow debris flow, while the distance from the basement ridge as well as thicknesses of individual seismic units were maintained.

Only Hole 986C and a small part of Hole 986D were logged (see "Wireline Logging" section, this chapter). Therefore, *P*-wave velocities from the downhole measurements were used for time-depth conversion in the interval between 80 and 460 mbsf. Laboratory measurements were used for the nonlogged intervals, corrected by 3% for core expansion during recovery in the upper 80 mbsf.

## Description of Seismic Stratigraphic Units

The sedimentary section above acoustic basement at Site 986 has a total thickness of 1.1 s two-way traveltime (TWT). In the following, the regional seismic stratigraphy recently defined for the entire Svalbard–Barents Sea margin (Faleide et al., 1996) has been adopted, with only small modifications which relate to the site-specific data set acquired during this survey. Since the main sequence boundaries are defined based on their regional character, they are not necessarily the most distinct seismic reflectors on a local scale.

Eight seismic sequences bounded by Reflectors R1 through R7, were defined between the seafloor and acoustic basement by Faleide et al. (1996). The upper seven sequences were believed to be of glacial origin. With the exception of Reflector R1, all sequence boundaries can be traced from the regional, pre-cruise seismic grid to the site. Reflector R1 is too shallow to be distinguished from the seafloor response in the shipboard seismic records. The 3.5-kHz PDR records, however, give good resolution within the upper section, and Reflector R1 is tentatively placed at the base of the 3.5-kHz penetration, which is within the lower part of the seafloor reflection in the water-gun seismic records. Reflector R2 has been defined with certainty only farther east, at shallower depth on the continental slope (Solheim et al., 1996a, 1996b) and its exact position adjacent to the site is more uncertain than for the deeper sequence boundaries. Faleide et al. (1996) did not assign names to the seismic sequences. To be consistent with name assignments used in earlier site chapters, they are therefore named seismic Units SV-I through SV-VII in the present report.

Seismic Unit SV-I, as recorded by 3.5-kHz PDR records, shows a distinctly layered character (Fig. 33A). The distance between individual internal reflectors is 2–3 milliseconds (ms), which equals 1.5–2 m, using a velocity of 1.55 km/s. Lens-shaped sediment bodies can be identified within this unit, immediately below the seafloor (Fig. 33B).

Units SV-II, SV-III, and SV-IV display similar seismic characters in the vicinity of Site 986. In general, they show a relatively low-amplitude, subhorizontal stratification. There is a distinct difference be-

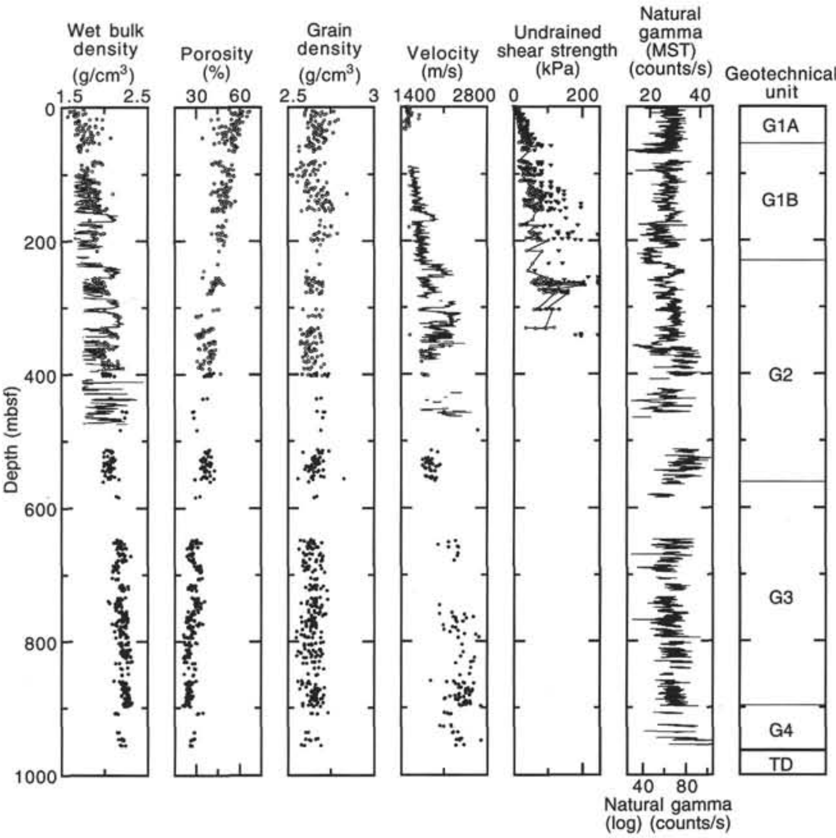


Figure 25. Geotechnical stratigraphy of Site 986, with vertical profiles of wet bulk density, porosity, grain density, *P*-wave velocity, undrained shear strength, and natural gamma radiation. Open and solid circles represent split-core measurements from Holes 986C and 986D, respectively, and lines represent measurements of bulk density and velocity from the downhole logging. Undrained shear strength measurements ($S_u$) were made only in Hole 986C. Open circles represent $S_u$ measured with the motorized vane, and triangles represent fall-cone penetrometer readings. Natural-gamma-ray counts from the downhole logging are plotted in the intervals of 100–375 mbsf and 420–455 mbsf.

tween the north-south-trending lines and the east-west-trending lines. In Line 986-S5, individual reflectors are discontinuous and display a low hummocky relief, locally defining lens-shaped bodies (Fig. 34). In Line 986-S3, however, most individual reflectors are conformable with the seafloor and are continuous over the length of the line (Fig. 35). Thicknesses of the three seismic units are 48, 59, and 53 m, using average interval velocities of 1.60, 1.68, and 1.75 km/s, respectively.

A large wedge-shaped body with a distinct, high-amplitude reflector as its upper boundary forms a prominent feature within Unit SV-III. In Line 986-S3, the upper and lower boundaries are conformable and continuous. By correlation with preexisting high-resolution seismic data from this area (Andersen et al., 1994; Solheim et al., 1996a), the wedge-shaped body is the southern portion of a southwestward-trending lens-shaped feature, believed to be a debris flow. Its thickness varies from 70 ms at the northern end of Line 986-S5 to 20 ms at the southern end of the line, while it is approximately 30 ms at Site 986. Using a velocity of 1.8 km/s, these time-thicknesses correspond to 63, 18, and 27 m, respectively. There are no velocity measurements for this interval (see "Physical Properties" section, this chapter), but based on velocities from downhole logging (see "Wireline Logging" section, this chapter) deeper in the hole, 1.8 km/s is a good estimate. Because the debris flow is a local feature, it has not been defined as a subunit, despite the unconformable character of its upper and lower boundaries.

The upper boundary of seismic Unit SV-V, Reflector R4, is a distinct, high-amplitude event at, and near, the site. Farther toward the west and north along Lines 986-S3 and 986-S5 (Figs. 34, 35), respectively, it does not differ from other low-amplitude reflections above and below. Eastward along Line 986-S3, however, it forms a consistent, strong reflector with only slight variation in amplitude in the middle part of the section (Fig. 35).

Seismic Unit SV-V is divided in two subunits along Reflector R4A, SV-VA and SV-VB, respectively, based on a distinct change in seismic character. Subunit SV-VA exhibits the same character as the overlying seismic Unit SV-IV, with low-amplitude reflectors that are more continuous in the east-west direction than in the north-south direction. Subunit SV-VB, below 3.2 s in the seismic section (Fig. 34), is characterized by a series of very strong reflectors that show the same east-west and north-south differences as the reflectors described above.

Reflector R5 is recognized as an important seismic sequence boundary along the entire Svalbard–Barents Sea margin (Faleide et al., 1996; Solheim et al., 1996a, 1996b), and its position in the present data set is determined through ties to the regional seismic grid. The seismic character of Subunit SV-VB continues below Reflector R5, and forms the predominant character of Unit SV-VI.

Reflector R6 marks the most distinct change in seismic character at Site 986, from the distinctly stratified unit above Reflector R6, to the essentially structureless Unit SV-VII. Broad, low-amplitude reflectors can be seen in the eastern part of Line 986-S3 (Fig. 35), but near the site, the unit has a seismically chaotic appearance. This is also recognized on a regional scale (Schlüter and Hinz, 1978; Eiken, 1994; Faleide et al., 1996; Hjelstuen et al., 1996). The chaotic character of Unit SV-VII is best developed and has its greatest areal extent south of Site 986, adjacent to the Storfjorden Fan (Hjelstuen et al., 1996). To the north and east of the site, as well as to the south of the Storfjorden Fan, the unit changes its character to seismically more stratified.

Although Reflector R7 is recognized as a prominent unconformity over the entire Svalbard–Barents Sea margin, it forms only a weak band of reflections in the area of Site 986. Based on correlation with pre-cruise seismic Line BEL-4, Reflector R7 is placed at the lower boundary of this reflecting band. Only a subtle change to fewer high-amplitude, discontinuous reflectors marks the change across Reflector R7, into seismic Unit SV-VIII. However, over large parts of the Svalbard–Barents Sea margin, to the north of Site 986, and to the

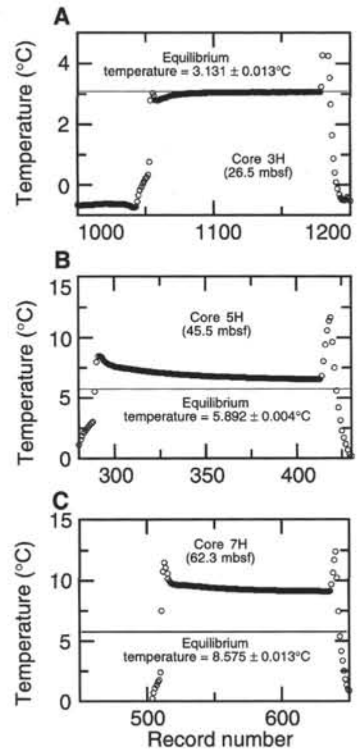


Figure 26. **A–C.** Downhole temperature measurements from Hole 986C.

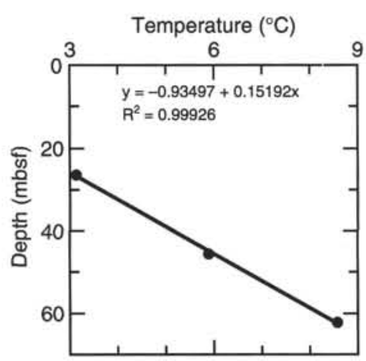


Figure 27. Calculated geothermal gradient for Hole 986C.

south of the Storfjorden Fan, this seismic unit is seismically well stratified.

Acoustic basement is defined at 3.98 s depth in the seismic section at the site (Fig. 34). Extrapolating seismic velocities from the velocities measured near the base of Hole 986D (see "Physical Properties" section, this chapter) gives a basement depth of 1170 mbsf at Site 986.

## Synthetic Seismogram

A synthetic seismogram was generated to facilitate correlation between seismic and lithostratigraphic units. The recalculated sonic log and edited density log from Holes 986C and 986D (see "Wireline Logging" section, this chapter) were used to calculate reflection coefficients between 90.4–378.2 and 428.3–475.0 mbsf. In the interval where log data from Holes 986C and 986D overlap (306–360 mbsf), the data from Hole 986C were used. The density logs from both holes contain many measurements that are thought to be too low as a result of data acquisition problems (see "Wireline Logging" section, this chapter). To prevent calculation of spurious reflection coefficients from these measurements, bulk density values less than 1.65 g/cm$^3$ were edited from the log data for depths less than 250 mbsf, and values less than 1.75 g/cm$^3$ were edited from the log data for greater depths. Discrete measurements of density and compressional velocity on the recovered cores (see "Physical Properties" section, this chapter) were used to calculate reflection coefficients above 90.4, between 378.2–428.3 and below 475.0 mbsf. There are no compressional velocity data between 33 mbsf and the start of the log data at 90.5 mbsf as a result of measurement difficulties (see "Physical Properties" section, this chapter), so velocities were linearly interpolated within this interval. Similarly, there are intervals at greater depths in which no wireline log data were collected and laboratory measurements of velocity are also lacking, as a result of measurement difficulties and nonrecovery. In intervals for which there are density data but no velocity data, velocities were linearly interpolated. A water velocity of 1480 m/s and density of 1.03 g/cm$^3$ were assumed to calculate a reflection coefficient for the seafloor. Reflection coefficients were calculated as a function of both depth and TWT, to enable TWT on the synthetic seismogram to be related directly to depth (Fig. 36).

The seismic line used for correlation is Line 986-S5 of the Site 986 site survey. The seismic source signature of Line 984-S5 data was estimated by stacking the seafloor reflection on the 21 shots closest to Site 986 (see "Explanatory Notes" chapter, this volume). On the stacked trace, the first 53 ms after the start of the seafloor reflection was interpreted as representing the reflection of the source signature from the seafloor. These data were extracted and convolved with the reflection coefficient series to produce an initial synthetic seismogram. Most of the significant reflectors in the survey data were clearly recognizable on this, but it showed a steadily increasing time lag with respect to the survey data with increasing two-way traveltime. An average velocity discrepancy of 3% was calculated from the lag. All of the velocity values were increased by 3%, then the reflection coefficient series and integrated TWT scale were recalculated using these revised velocities (Fig. 36B), and the convolution was repeated to produce the synthetic seismogram shown in Figure 36C.

Figure 37 shows the synthetic seismogram inserted into Line 986-S5 at the location of the site. Most of the significant reflectors are clearly recognizable on the synthetic seismogram from their shape and amplitude. The close correspondence between the TWT's of reflectors on the synthetic seismogram and on the survey data confirms the accuracy of the revised velocity function.

The origin of the TWT axis in Figure 36C is at the start of the initial trough of the seafloor reflection. All other TWT's reported in this chapter are measured from just before the onset of the first peak of the seafloor reflection, so the TWT's of all reflectors in Figure 36C have an apparent lag of 10 ms. The estimated seismic source signature contains two main peaks 17 and 38 ms after its start, separated by a trough of similar amplitude 28 ms after its start. Therefore, the main seismic response to each reflection coefficient in Figure 36B is delayed by 17–38 ms. This is well illustrated by Reflector R4, which shows large reflection amplitudes between 218 and 248 ms on the synthetic seismogram in Figure 36C and a large, central peak at 232 ms. These large amplitudes are mainly the result of constructive interference between reflections from a boundary with a positive reflection coefficient at 195 ms and a boundary with a negative reflection coefficient at 208 ms in Figure 36B. These reflection coefficients are at the top and base, respectively, of a high-velocity layer between 159 and 172 mbsf, which is interpreted as a large debris flow (see "Lithostratigraphy" section, this chapter).

The large reflection amplitudes between 345 and 400 ms in Figure 36C, above Reflector R5, are a response to the large reflection coefficients between 330 and 385 ms, shown in Figure 36B, which occur at depths of 285–344 mbsf. Reflector R5 itself, the peak of which is at 413 ms in Figure 36C, receives a contribution from the latter part

**Table 19. Logged depth intervals in Hole 986C for Quad, FMS, and GHMT runs.**

| String | Run | Depth interval logged (mbsf) | (mbrf) | Tools |
|---|---|---|---|---|
| **Quad combo:** | Down | 100.0–387.0 | 2165.0–2450.0 | NGT/SDT/CNT-G/HLDT/DIT/TLT |
| | Up | 392.0–87.0 | 2455.0–2150.0 | NGT/SDT/CNT-G/HLDT/DIT/TLT |
| | Up* | 188.0–128.0 | 2190.0–2250.0 | NGT/SDT/CNT-G/HLDT/DIT/TLT |
| Start time: | 0015 hr | | | |
| Stop time: | 0300 hr | | | |
| Logging speeds: | 375 m/hr down log | | | |
| | 275 m/hr up log | | | |
| (Mudline measured at 2062.5 mbrf with NGT) | | | | |
| **FMS**: | Up | 293.0–85.0 | 2357.0–2150.0 | NGT/FMS/GPIT |
| | Up | 368.0–85.0 | 2160.0–2150.0 | NGT/FMS/GPIT |
| Start time: | 0500 hr | | | |
| Stop time: | 0700 hr | | | |
| Logging speed: | 460m/hr | | | |
| **GHMT:** | Up* | 370.0–318.0 | 2432.0–2380.0 | NGT/GHMT |
| | Up | 370.0–88.0 | 2432.0–2051.0 | NGT/GHMT |
| Start time: | 0830 hr | | | |
| Stop time: | 1100 hr (8/14/95)—logging completed | | | |
| Logging speed: | 550 m/hr | | | |
| Wiper trip: | Hole conditioning prior to logging | | | |
| Start time: | 1630 hr (8/13/95)—logging started | | | |
| Stop time: | 2330 hr | | | |
| Total logging time: 18.5 hr | | | | |
| Estimated time: ~19–21 hr | | | | |

Notes: Depths are in meters below seafloor (mbsf) and meters below rig floor (mbrf). * = repeat section for quality control. NGT = Natural Gamma-ray Tool, SDT = Sonic Digital Tool (Array), CNT-G = Compensated Neutron Porosity Tool, HLDT = High-temperature Litho-Density Tool, DIT = Dual Induction Resistivity Tool, TLT = Lamont-Doherty Temperature Tool, FMS = Formation MicroScanner, GPIT = General Purpose Inclinometry Tool, GHMT = Geological High-sensitivity Magnetic Tool.

**Table 20. Logged depth intervals in Hole 986D for Quad combo runs.**

| Run | Depth interval logged (mbsf) | (mbrf) | Tools |
|---|---|---|---|
| Down | 325.0–387.0 | 2385.0–2460.0 | NGT/SDT/CNT-G/HLDT/DIT/TLT |
| Up | 410.0–308.0 | 2472.0–2370.0 | NGT/SDT/CNT-G/HLDT/DIT/TLT |
| Second logging run attempted after lowering pipe ~116 m to 2501 mbrf: | | | |
| Up* | 493.0–425.0 | 2555.0–2487.0 | NGT/SDT/CNT-G/HLDT/DIT/TLT |
| Start time: | 0130 hr | | |
| Stop time: | 1130 hr (8/20/95) | | |
| Logging speeds: | 375 m/hr down log | | |
| | 275 m/hr up log | | |
| (Mudline measured at 2062.5 mbrf with NGT) | | | |
| Wiper trip: | Hole conditioning prior to logging | | |
| Start time: | 0600 hr (8/19/95)—logging started | | |
| Stop time: | 0130 hr (8/20/95) | | |
| Total logging time: 29 hr | | | |
| Estimated time: ~27 hr | | | |

Notes: Depths are in meters below seafloor (mbsf) and meters below rig floor (mbrf). * = logging efforts terminated at 1130 hr after decision was made that borehole conditons were too difficult to continue.

of the reflections from some of the boundaries that cause the high amplitudes above, but is probably mainly a response to more large-reflection coefficients between 395 and 402 ms, corresponding to depths of 354–361 m. Two high-amplitude reflections on the survey data, 50 and 80 ms below Reflector R5, are not represented on the synthetic seismogram because the boundaries that cause them lie in the interval 378.2–428.3 mbsf, where there are no wireline log data and hardly any laboratory velocity or density measurements. Reflector R6 is rather weak near Site 986, but there is a high-amplitude reflection immediately above it (peak at 570 ms in Figure 36B). On the synthetic seismogram this reflection is mainly a response to the isolated, large negative reflection coefficient at 544 ms (513 mbsf). However, this reflection coefficient was calculated from the acoustic impedance change across a 29-m-thick interval above 513 mbsf in which there are no velocity or density data, so the actual change in acoustic impedance that causes the reflector on the survey data could occur anywhere within that interval.

In the interpretation of the survey data, the delayed seismic response has been accounted for by always making the reflectors well above the first peak. Still, this may explain some of the discrepancies between core and seismic data.

## Discussion

The drilled sedimentary sequence at Site 986 consisted of four lithostratigraphic units and four geotechnical units (see "Lithostratig-

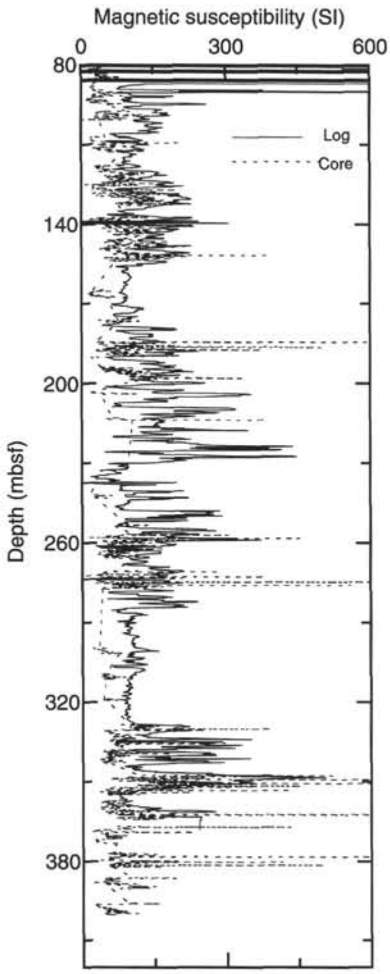


Figure 28. Comparison of log magnetic susceptibility data with magnetic susceptibility core measurements from Hole 986C. Depth scales for both data sets are given in meters below seafloor (mbsf). Seafloor depth measurements from both logs and drillers were within 0.5 m, so only a small depth correction had to be made in order to compare the data. No other downhole depth shifts were applied.

raphy" and "Physical Properties" sections, this chapter, and Fig. 38). Below 500 mbsf, the different stratigraphies correlate with each other, showing the lithologic and physical significance of Reflectors R6 and R7. In the upper 500 mbsf, however, the lithostratigraphy shows less variation than that detected by seismic and geotechnical methods.

The seismic character of the upper four units, SV-I through SV-IV, as well as Subunit SV-VA, seems to reflect the presence of debris flows. This interpretation is strongly supported by the different character of the low-amplitude, internal reflection pattern between north-south-trending and east-west-trending seismic lines, respectively (Figs. 34, 35). The east-west lines run subparallel to the flow direction of debris flows from the margin, while the north-south lines, running subperpendicular to the flow direction, portray the shape of individual lobes. From the seismic records, this upper interval of approximately 250 m represents a period of frequent but relatively small debris flows, but with occasional larger events, as observed by the large wedge-shaped body between 2.97 and 3.00 s TWT (Fig. 34). The large debris flows are confined to seismic Units SV-III and SV-IV adjacent to Site 986. While the large flows exceed 20 m thickness, the smaller flows apparently rarely exceed 8 m thickness, but the resolution of the shipboard seismic data limits the detail to which we can map individual lobes. The sediments in the upper 350 mbsf have a relatively high content of methane (see "Organic Geochemistry" section, this chapter). However, this does not seem to have a significant effect on the seismic records, as seen from the distinct, high-amplitude reflections from the thicker debris flows.

Reflector R4A seems to indicate a major change in depositional style at Site 986. From seismic Subunit SV-VB, larger debris flows seem to dominate through this and the next, lower seismic Unit SV-VI. These are represented as strong internal reflectors in the seismic sections, but still with the same change in character between the east-west- and north-south-trending lines. The change from Subunit SV-VA to SV-VB is also detected in the physical property characteristics of the sediments, as the change from geotechnical Unit G1B to G2 (Fig. 38; see "Physical Properties" section, this chapter). The lithologic character, unsorted silty clays with frequent shell fragments and varying amounts of larger clasts, also support a debris-flow origin for these upper sediments. The change from larger to smaller debris flows, however, does not affect the lithology, and this is the reason why lithostratigraphic Unit II covers most of the debris-flow-dominated part of the drilled section.

The change across Reflector R6, from seismic Unit SV-VI to SV-VII, is also observed as a lithostratigraphic boundary, marked by a decrease in the clast content and increase in the sand content of the sediments (see "Lithostratigraphy" section, this chapter). The boundary is also clearly seen as a boundary in the geotechnical stratigraphy. From the regional seismic stratigraphy of the Svalbard–Barents Sea continental margin, Unit SV-VII has its largest thickness southwest of Spitsbergen off a major shelf trough, the Storfjorden Trough (Hjelstuen et al., 1996). The unit also differs from the units above and below in having a landward-decreasing thickness. Hence, it clearly represents a different depositional regime than the sediments above Reflector R6; it has less ice-rafted debris and no or considerably less frequent debris flows, but still shows a significant terrigenous input, with southern Svalbard and the northwestern Barents Sea as likely source areas.

The lowermost seismic Unit SV-VIII, displays a seismic character similar to that of Unit SV-VII at Site 986. Reflector R7 corresponds to the boundary between lithostratigraphic Subunits IVA and IVB, with a lower sand content relative to clay in the latter subunit. The transition is also clearly marked in the geotechnical stratigraphy (see "Lithostratigraphy" and "Physical Properties" sections, this chapter). On a regional scale, this unit is generally acoustically stratified and thickens rapidly eastward (Faleide et al., 1996), and Reflector R7 is the most distinct regional seismic reflector along the entire Svalbard–Barents Sea continental margin.

In summary, the seismic stratigraphy at Site 986 corresponds well with the lithostratigraphy and, in particular, the geotechnical stratigraphy. The variation in seismic character, supported by lithological observations and physical properties, indicate a considerable change in depositional environment through the drilled Pliocene–Pleistocene section. A lower, mud-dominated period, prior to Reflector R7 time, was followed by a period of sand-rich deposition forming a 300-m-thick seismically homogeneous unit at Site 986. The wide and indistinct character of Reflector R7 indicates a transitional period. This is also indicated by lithostratigraphic Subunit IVA, above Reflector R7, in which there is also evidence for deformation (see "Lithostratigraphy" section, this chapter). After Reflector R6 time, deposition in this part of the Svalbard Margin was dominated by downslope, gravity-driven sedimentary processes, with debris flows as the volumetrically most important component. With improved age information, these changes can probably be related to changes in the style and frequency of glaciations.

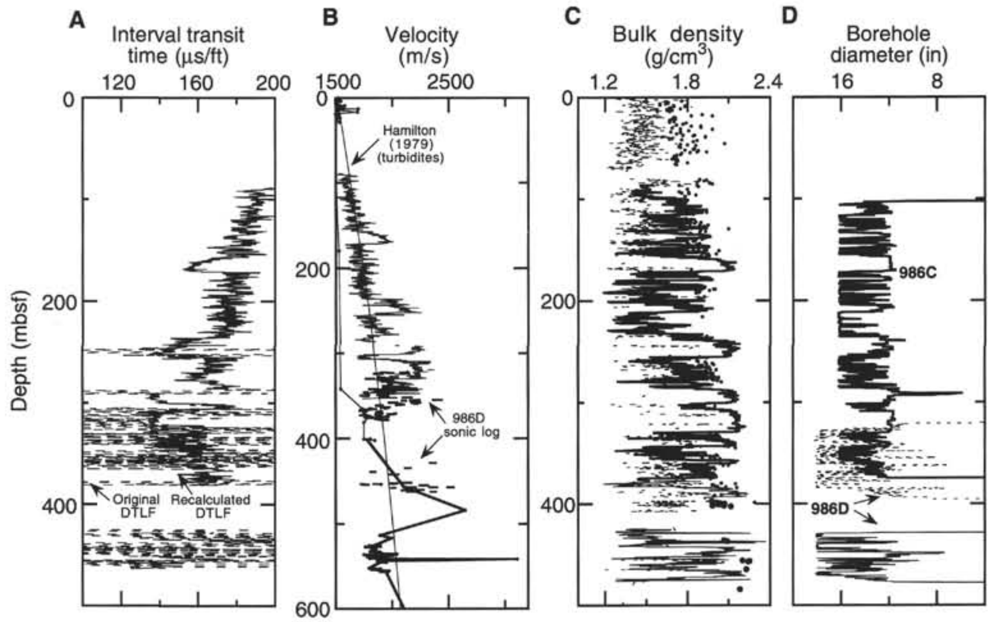


Figure 29. **A.** Comparison of original depth-derived, borehole-compensated sonic logs (DTLF) from Holes 986C and 986D, computed during logging, with the same logs recalculated after removal of noise spikes from the original transit-time data. **B.** Comparison of seismic velocities from recalculated sonic logs with laboratory velocity measurements on core samples (line with solid dots) and the empirical velocity vs. depth functions for turbidite successions from Hamilton (1979). **C.** Comparison of wireline log bulk density measurements (solid line) with GRAPE bulk density measurements (dashed line) and gravimetric wet bulk density measurements (solid circles). In the interval in which the wireline log data from Holes 986C and 986D overlap, only the data from Hole 986C are shown. **D.** Downhole caliper measurements show the washed-out zones that account for the very low densities observed.

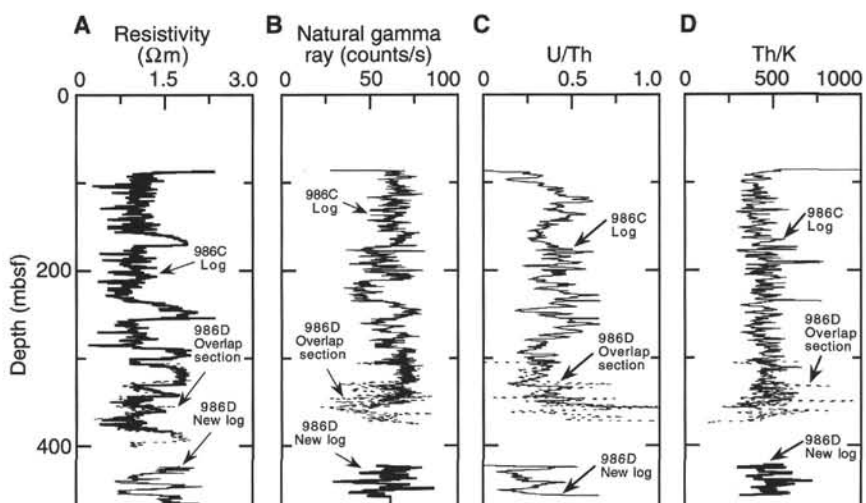


Figure 30. **A.** Downhole resistivity measurements from Site 986 clearly show the "stacked" sequence of debris flows. Note the consistency between the overlapped sections from Holes 986C and 986D. **B.** Downhole natural gamma-ray measurements at Site 986. Note that the similar wireline response of natural gamma-ray log to debris-flow layers. **C, D.** A comparison of downhole U/Th and Th/K ratios.

## REFERENCES


Andersen, E.S., Solheim, A., and Elverhøi, A., 1994. Development of a glaciated Arctic continental margin exemplified by the western margin of Svalbard. *In* Thurston, D.K., and Fujita, K. (Eds.), *Proc. Int. Conf. on Arctic Margins.* U.S. Dept. of the Interior, Mineral Management Service, Alaska Outer Shelf Region, OCS Study, MMS 94-0040, 155–160.

Baumann, K.-H., Lackschewitz, K.S., Mangerud, J., Spielhagen, R.F., Wolf-Welling, T.C.W., Henrich, R., and Kassens, H., 1995. Reflection of Scandinavian ice sheet fluctuations in Norwegian Sea sediments during the past 150,000 years. *Quat. Res.,* 43:185–197.

Berger, W.H., and Jansen, E., 1994. Mid-Pleistocene climate shift: the Nansen connection. *In* Johannessen, O.M., Muensch, R.D., and Overland, J.E. (Eds.), *The Role of the Polar Oceans in Shaping the Global Environment.* Geophys. Monogr., Am. Geophys. Union, 85:295–311.

Berggren, W.A., Hilgen, F.J., Langereis, C.G., Kent, D.V., Obradovich, J.D., Raffi, I., Raymo, M.E., and Shackleton, N.J., 1995. Late Neogene chronology: new perspectives in high-resolution stratigraphy. *Geol. Soc. Am. Bull.,* 107:1272–1287.

Borehole Research Group, 1994. *Wireline Logging Services Guide:* Palisades, NY (Lamont-Doherty Earth Observatory, Columbia Univ.).

Crane, K., and Sundvor, E., 1995. Crustal heat flow in the northern Norwegian-Greenland Sea. *In* Crane, K., and Solheim, A. (Eds.), *Seafloor Atlas of the Northern Norwegian-Greenland Sea.* Norsk Polarinst. Medd., 137:24–29.

Eidvin, T., Jansen, E., and Riis, F., 1993. Chronology of Tertiary fan deposits off the western Barents Sea: implications for the uplift and erosion history of the Barents Shelf. *Mar. Geol.,* 112:109–131.

Eiken, O., 1994. *Seismic Atlas of Western Svalbard.* Norsk Polarinst. Medd., 130:1–73.

Faleide, J.I., Solheim, A., Fiedler, A., Hjelstuen, B.O., Andersen, E.S., and Vanneste, K., 1996. Late Cenozoic evolution of the western Barents Sea-Svalbard continental margin. *Global Planet. Change,* 12:53–74.

Flower, B., in press. Late Quaternary stable isotopic stratigraphy of Hole 910A, Yermak Plateau, Arctic Ocean: relations with Svalbard/Barents Sea ice-sheet history. *In* Thiede, J., Myhre, A.M., Firth, J.V., Johnson, G.L., and Ruddiman, W.F. (Eds.), *Proc. ODP, Sci. Results,* 151: College Station, TX (Ocean Drilling Program).

Fronval, T., and Jansen, E., in press, Late Neogene paleoclimates and paleoceanography in the Iceland-Norwegian Sea: evidence from the Iceland and Vøring Plateaus. *In* Thiede, J., Myhre, A.M., Firth, J.V., Johnson, G.L., and Ruddiman, W.F. (Eds.), *Proc. ODP, Sci. Results,* 151: College Station, TX (Ocean Drilling Program).

Hamilton, E.L., 1979. Sound velocity gradients in marine sediments. *J. Acoust. Soc. Am.,* 65:909–922.

Henrich, R., and Baumann, K.H. 1994. Evolution of the Norwegian Current and the Scandinavian Ice Sheets during the past 2.6 m.y.: evidence from ODP Leg 104 biogenic carbonate and terrigenous records. *Palaeogeogr., Palaeoclimatol., Palaeoecol.,* 108:75–94.

Hjelstuen, B.O., Elverhøi, A., and Faleide, J.I., 1996. Cenozoic erosion and sediment yield in the drainage area of the Storfjorden Fan. *Global Planet. Change.*

Jansen, E., Bleil, U., Henrich, R., Kringstad, L., and Slettemark, B., 1988. Paleoenvironmental changes in the Norwegian Sea and Northeast Atlantic during the last 2.8 m.y.: Deep Sea Drilling Project/Ocean Drilling Program Sites 610, 642, 643, and 644. *Paleoceanography,* 3:563–581.

Jansen, E., and Sjøholm, J., 1991. Reconstruction of glaciation over the past 6 Myr from ice-borne deposits in the Norwegian Sea. *Nature,* 349:600–603.

Jones, G.A., and Keigwin, L.D., 1988. Evidence from Fram Strait (78°N) for early deglaciation. *Nature,* 336:56–59.

Kastner, M., Elderfield, H., Jenkins, W.J., Gieskes, J.M., and Gamo, T., 1993. Geochemical and isotopic evidence for fluid flow in the western Nankai subduction zone, Japan. *In* Hill, I.A., Taira, A., Firth, J.V., et al., *Proc. ODP, Sci. Results,* 131: College Station, TX (Ocean Drilling Program), 397–413.

Kvenvolden, K.A., and Barnard, L.A., 1983. Gas hydrates of the Blake Outer Ridge, Site 533, Deep Sea Drilling Project Leg 76. *In* Sheridan, R.E., Gradstein, F.M., et al., *Init. Repts. DSDP,* 76: Washington (U.S. Govt. Printing Office), 353–365.

Lindsley-Griffin, N., Kemp, A., and Swartz, J.F., 1990. Vein structures of the Peru Margin, Leg 112. *In* Suess, E., von Huene, R., et al., *Proc. ODP, Sci. Results,* 112: College Station, TX (Ocean Drilling Program), 3–16.

Molnar, P., and England, P., 1990. Late Cenozoic uplift of mountain ranges and global climate change: chicken or egg? *Nature,* 346:29–34.

Myhre, A.M., Thiede, J., Firth, J.V., et al., 1995. *Proc. ODP, Init. Repts.,* 151: College Station, TX (Ocean Drilling Program).

Okada, H., and Bukry, D., 1980. Supplementary modification and introduction of code numbers to the low-latitude coccolith biostratigraphic zonation (Bukry, 1973; 1975). *Mar. Micropaleontol.,* 5:321–325.

Peters, K.E., 1986. Guidelines for evaluating petroleum source rock using programmed pyrolysis. *AAPG Bull.,* 70:318–329.

Riis, F., and Fjeldskaar, W., 1989. On the magnitude of the late Tertiary and Quaternary erosion and its significance for the uplift of Scandinavia and the Barents Sea. *In* Larsen, R.M., Brekke, H., Larsen, B.T., and Talleräs, E. (Eds.), *Structural and Tectonic Modelling and Its Application to Petroleum Geology.* Norw. Pet. Soc. Spec. Publ.: Amsterdam (Elsevier), 1:163–185.

Schlüter, H.U., and Hinz, K., 1978. The continental margin of west Spitsbergen. *Polarforschung,* 48:151–169.

Solheim, A., Andersen, E.S., Elverhøi, A., and Fiedler, A., 1996a. Late Cenozoic depositional history of the western Svalbard continental shelf, controlled by subsidence and climate. *Global Planet. Change,* 12:135–148.

Solheim, A., Riis, F., Elverhøi, A., Faleide, J.I., Jensen, L.N., and Cloetingh, S., 1996b. Impact of glaciations on basin evolution: data and models from the Norwegian margin and adjacent areas. *Global Planet. Change,* 12:1–9.

Spiegler, D., and Jansen, E., 1989. Planktonic foraminifer biostratigraphy of Norwegian Sea sediments: ODP Leg 104. *In* Eldholm, O., Thiede, J., Taylor, E., et al., *Proc. ODP, Sci. Results,* 104: College Station, TX (Ocean Drilling Program), 681–696.

Stein, R., Brass, G., Graham, D., Pimmel, A., and the Shipboard Scientific Party, 1995. Hydrocarbon measurements at Arctic Gateways sites (ODP Leg 151). *In* Myhre, A.M., Thiede, J., Firth, J.V., et al., *Proc. ODP, Init. Repts.,* 151: College Station, TX (Ocean Drilling Program), 385–395.

Wolf, T.C.W., and Thiede, J., 1991. History of terrigenous sedimentation during the past 10 m.y. in the North Atlantic (ODP Legs 104 and 105 and DSDP Leg 94). *Mar. Geol.,* 101:83–102.

Wolf-Welling, T.C.W., Cremer, M., and O'Connell, S., in press. Cenozoic Arctic Gateway paleoclimate variability: indications from changes in coarse fraction composition. *In* Thiede, J., Myhre, A.M., Firth, J.V., Johnson, G.L., and Ruddiman, W.F. (Eds.), *Proc. ODP, Sci. Results,* 151: College Station, TX (Ocean Drilling Program).

**Ms 162IR-109**

**Note: For all sites drilled, core description forms ("barrel sheets") and core photographs can be found in Section 3, beginning on page 391. Forms containing smear slide data can be found in Section 4, beginning on page 1147. All processed logs (including FMS, dipmeter, temperature data, high-resolution density and neutron data, and sonic waveforms not shown in printed form) are on the CD-ROM enclosed in the back pocket of this volume. Also on the CD-ROM are all tables from this chapter (including an extended coring summary table) and shipboard measurements (files containing GRAPE density, *P*-wave velocity, natural gamma radiation, magnetic susceptibiltiy, index properties, and spectral reflectance data).**

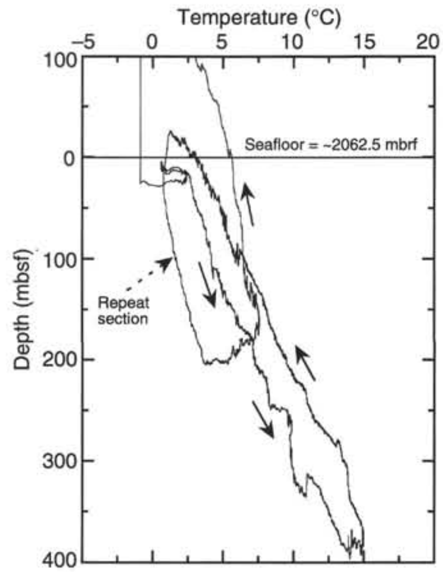


Figure 31. Borehole fluid temperature profile recorded in Hole 986C using the Lamont temperature logging tool (TLT) on the Quad combo logging run.

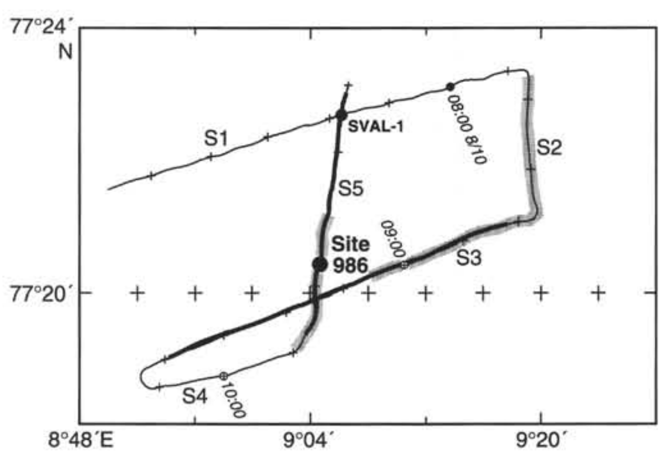


Figure 32. Map showing the site survey near Site 986. Thick gray lines indicate 3.5-kHz profiles shown in Figure 33. Bold black lines mark seismic profiles shown in Figures 34 and 35.

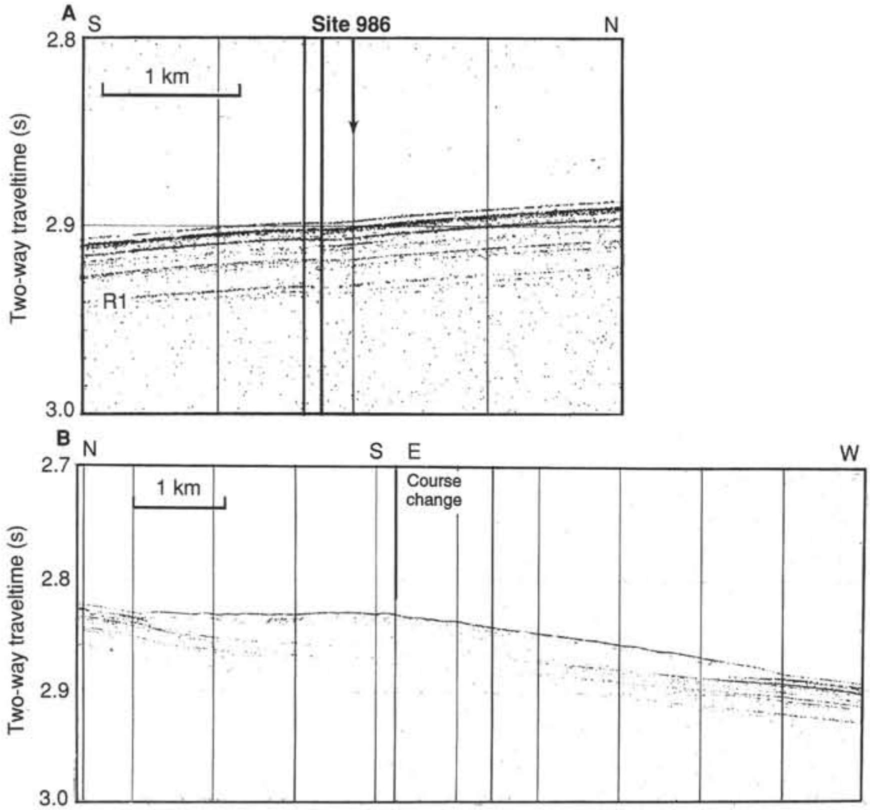


Figure 33. **A.** Sample of 3.5-kHz PDR record along Line 986-S5, showing seismic Unit SV-I. **B.** Sample of 3.5-kHz record along Lines 986-S2 and S3, showing lobe-shaped deposit, possibly a debris flow, in the youngest sediments. See Figure 32 for location.

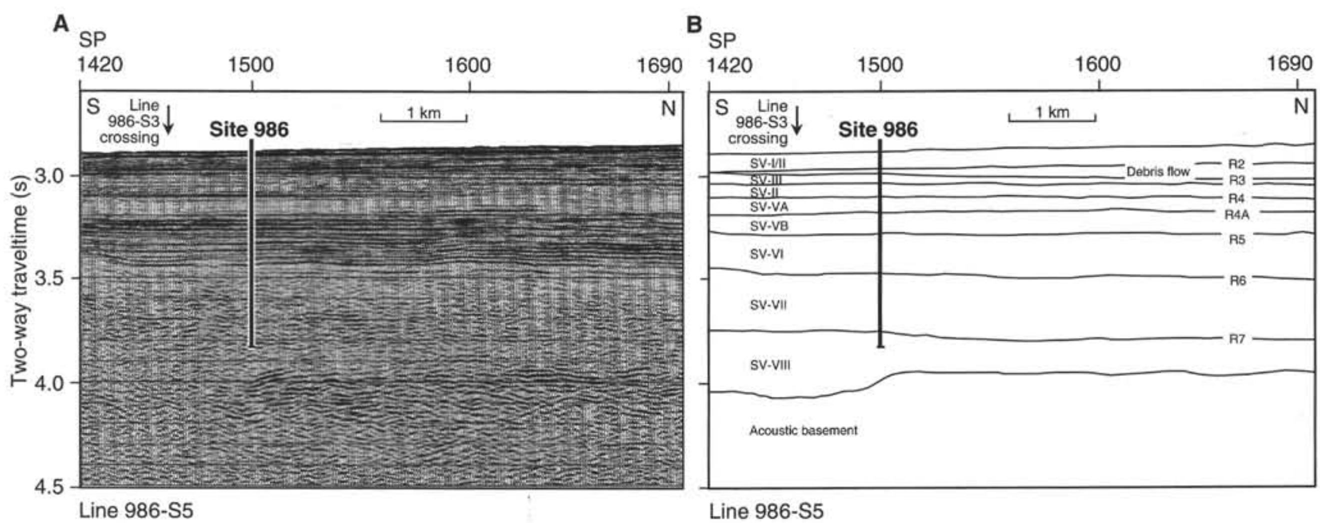


Figure 34. **A.** Seismic Line 986-S5, crossing Site 986. **B.** Interpretation of seismic Line 986-S5. The thickest debris flow in the upper part of the section is marked. See Figure 32 for location.

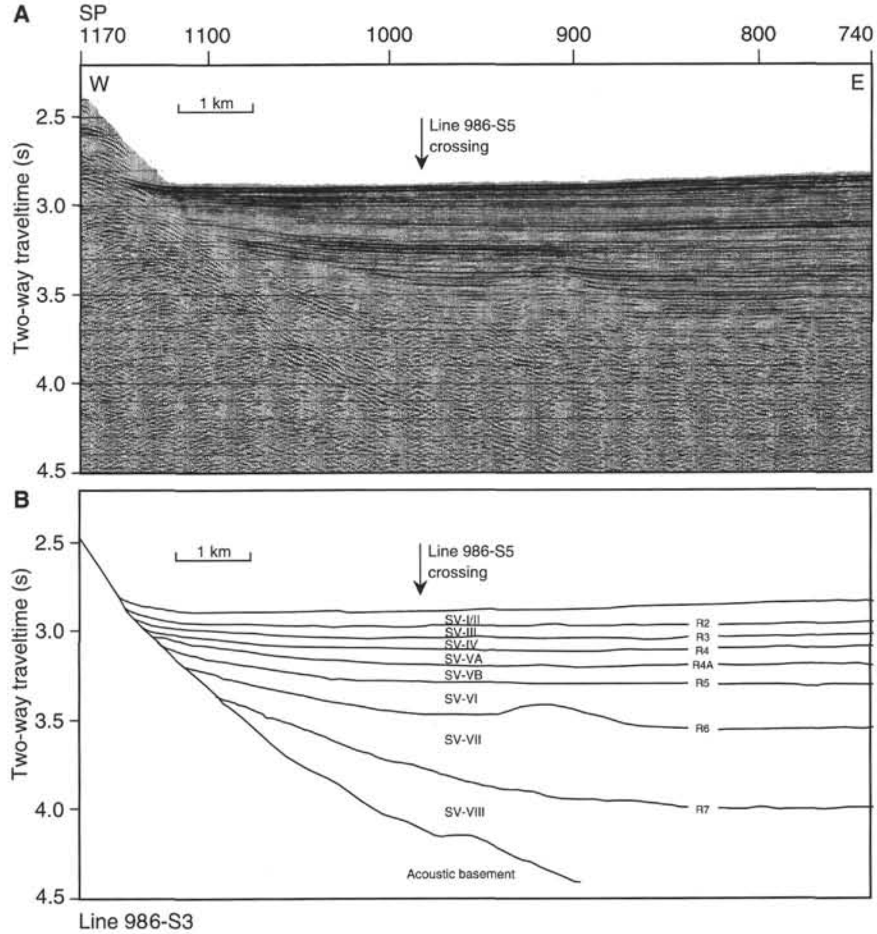


Figure 35. **A.** Seismic Line 986-S3. **B.** Interpretation of seismic Line 986-S3, with seismic units and reflectors shown. See Figure 32 for location.

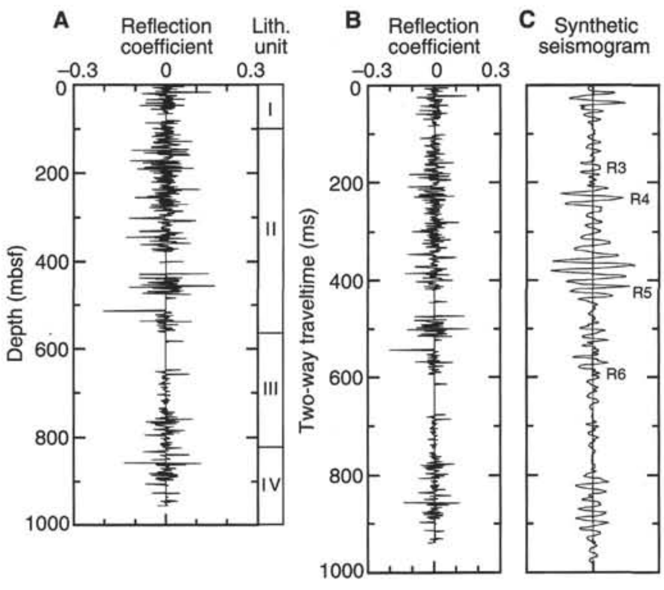


Figure 36. **A.** Reflection coefficients plotted vs. depth. Reflection coefficients were calculated from log data between 90.4 and 378.2 mbsf and 428.3 and 475.0 mbsf, and from discrete measurements on cores outside these intervals. Also shown are the lithostratigraphic unit boundaries (see "Lithostratigraphy" section, this chapter). **B.** Reflection coefficients plotted vs. two-way traveltime below seafloor. **C.** Synthetic seismogram plotted vs. two-way traveltime below seafloor. Significant seismic reflectors, which have been identified by comparison with site survey Line 986-S5, are labeled on the synthetic seismogram.

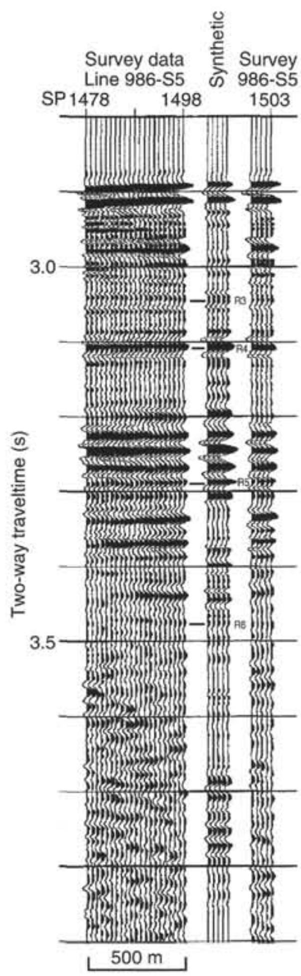


Figure 37. Part of site survey Line 986-S5 with five copies of the synthetic seismogram inserted at the location of Site 986.

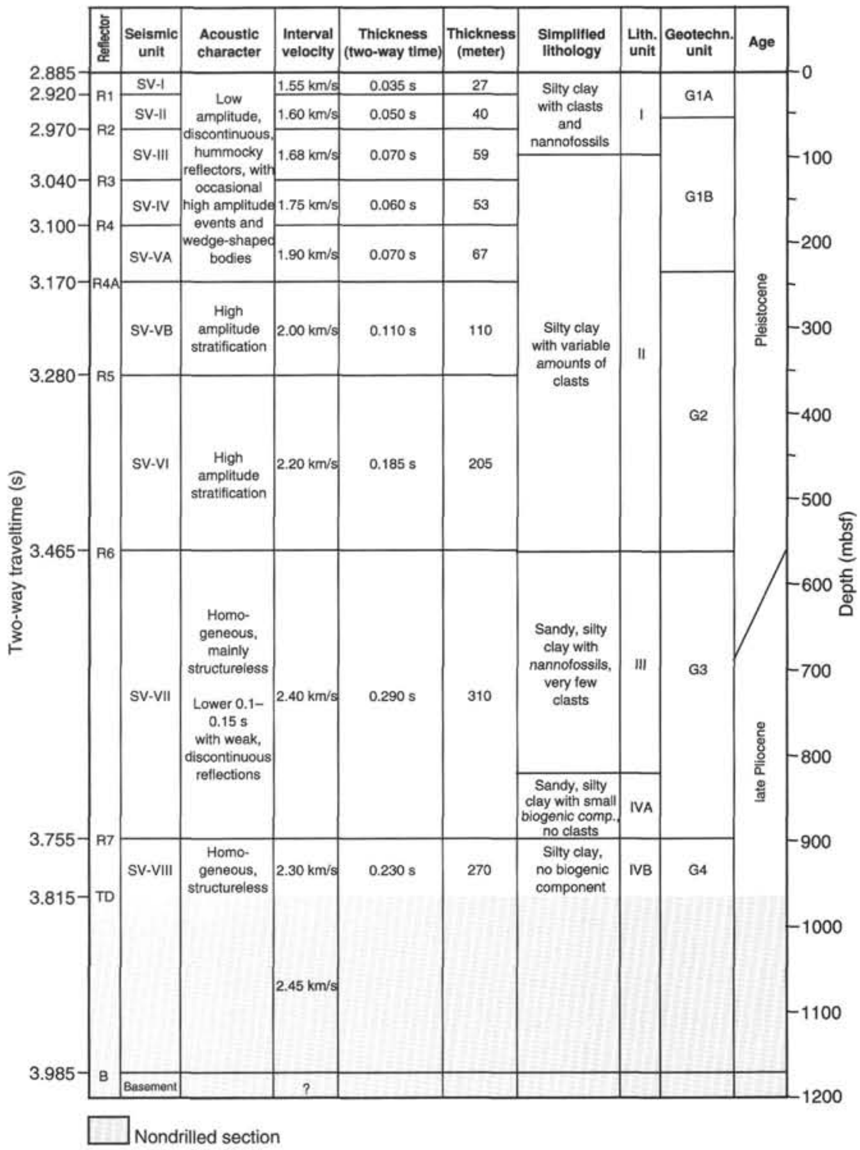


Figure 38. Correlation of the seismic stratigraphy with lithostratigraphy and geotechnical stratigraphy.

## SHORE-BASED LOG PROCESSING

### Hole 986C

**Bottom felt:** 2062.5 mbrf (used for depth shift to seafloor)
**Total penetration:** 408 mbsf
**Total core recovered:** 229.8 m (56.3%)

#### *Logging Runs*

**Logging string 1:** DIT/SDT/HLDT/CNTG/NGT
**Logging string 2:** FMS/GPIT/NGT (2 passes)
**Logging string 3:** GHMT/NGT
Wireline heave compensator was used to counter ship's heave.

#### *Bottom-Hole Assembly*

The following bottom-hole assembly (BHA) depths are as they appear on the logs after differential depth shift (see "Depth shift" section) and depth shift to the seafloor. As such, there might be a discrepancy with the original depths given by the drillers on board. Possible reasons for depth discrepancies are ship's heave, use of wireline heave compensator, and drill string and/or wireline stretch.
DIT/SDT/HLDT/CNTG/NGT: BHA at ~86 mbsf.
FMS/GPIT/NGT: Did not reach BHA.
GHMT/NGT: BHA at ~87 mbsf.

#### *Processing*

**Depth shift:** Original logs have been interactively depth shifted with reference to NGT from DIT/SDT/HLDT/CNTG/NGT main run and to the seafloor (−2062.5 m).

**Gamma-ray processing:** Data have been processed to correct for borehole size and type of drilling fluid.

**Acoustic data processing:** The array sonic tool was operated in depth-derived, borehole compensated mode using the long-spacing (8–10–10–12 ft) configuration. The sonic logs have been processed to eliminate some of the noise and cycle skipping experienced during the recording.

#### *Quality Control*

Data recorded through bottom-hole assembly, such as the gamma-ray and neutron porosity data above 86 mbsf, should be used qualitatively only because of the attenuation on the incoming signal. Invalid gamma-ray spikes were recorded at 74–78 and 81–85.5 mbsf.

Hole diameter was recorded by the hydraulic caliper on the HLDT tool (CALI) and the caliper on the FMS string (C1 and C2).

### Hole 986D

**Bottom felt:** 2062.5 mbrf (used for depth shift to seafloor)
**Total penetration:** 576.8 mbsf
**Total core recovered:** 241.6 m (41.9%)

#### *Logging Runs*

**Logging string 1:** DIT/SDT/HLDT/CNTG/NGT (upper and lower sections)
Wireline heave compensator was used to counter ship's heave.

#### *Bottom-Hole Assembly*

The following bottom-hole assembly (BHA) depths are as they appear on the logs after differential depth shift (see "Depth shift" section) and depth shift to the seafloor. As such, there might be a discrepancy with the original depths given by the drillers on board. Possible reasons for depth discrepancies are ship's heave, use of wireline heave compensator, and drill string and/or wireline stretch.
DIT/SDT/HLDT/CNTG/NGT: BHA at ~306 mbsf (upper section)
DIT/SDT/HLDT/CNTG/NGT: BHA at ~422.5 mbsf (lower section).

#### *Processing*

**Depth shift:** No differential depth shift has been applied as the two sections do not overlap. Original logs have been depth shifted to the seafloor (−2062.5 m).

**Gamma-ray processing:** Data have been processed to correct for borehole size and the heavy barite drilling fluid used to stabilize the hole.

**Acoustic data processing:** The array sonic tool was operated in depth-derived, borehole compensated mode using the long-spacing (8–10–10–12 ft) configuration. The sonic logs from have been processed to eliminate some of the noise and cycle skipping experienced during the recording.

#### *Quality Control*

Data recorded through bottom-hole assembly, such as the gamma-ray and neutron porosity data above 306 and between 422.5 and 405 mbsf, should be used qualitatively only because of the attenuation on the incoming signal. Invalid gamma-ray spikes were recorded at 300–305.5 and 418–422.5 mbsf.

Hole diameter was recorded by the hydraulic caliper on the HLDT tool (CALI).

For further information about the logs, please contact:

Cristina Broglia
Phone: 914-365-8343
Fax: 914-365-3182
E-mail: chris@ldeo.columbia.edu

Elizabeth Pratson
Phone: 914-365-8313
Fax: 914-365-3182
E-mail: beth@ldeo.columbia.edu

Hole 986C: Natural Gamma Ray-Resistivity-Sonic Logging Data

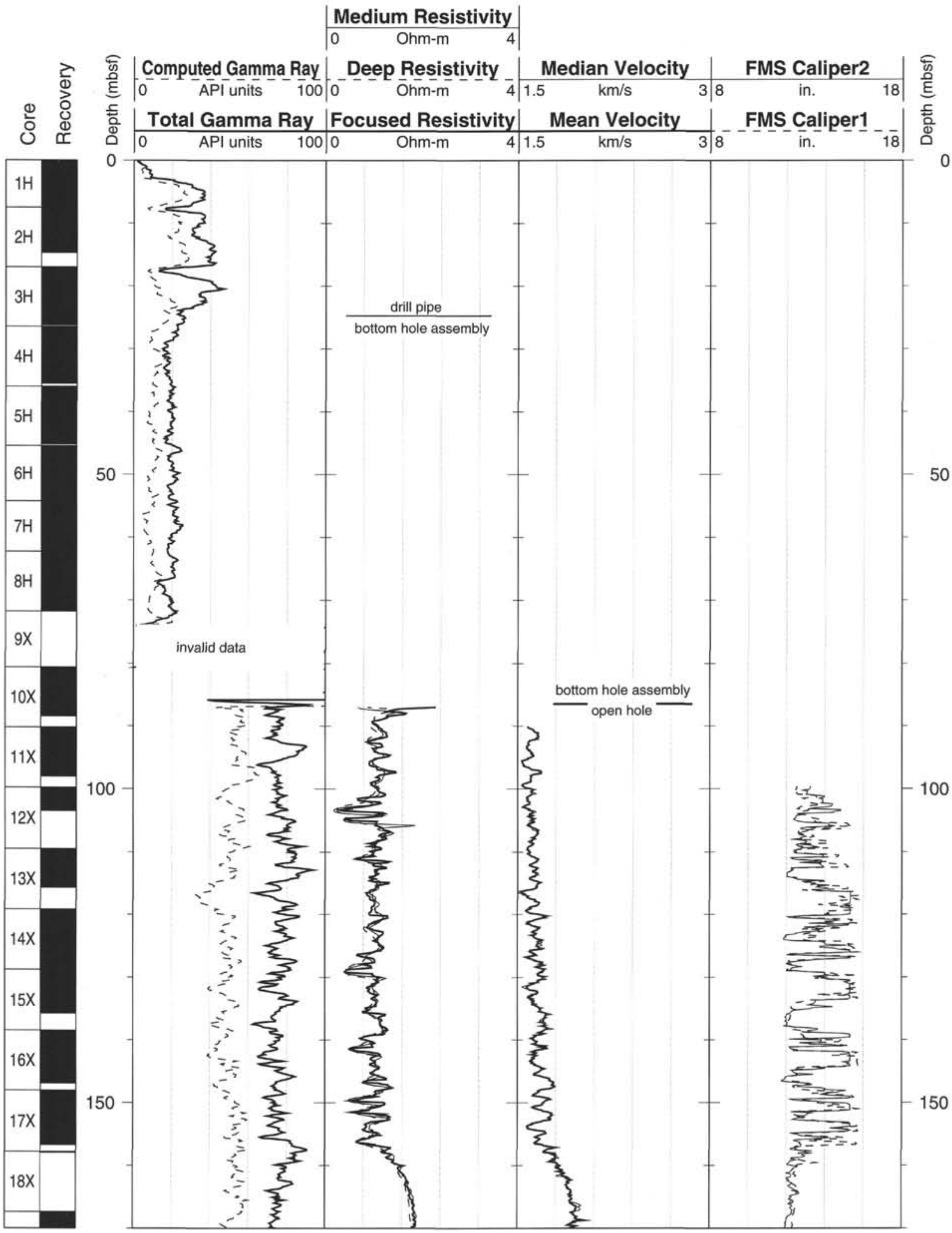

Hole 986C: Natural Gamma Ray-Resistivity-Sonic Logging Data (cont.)

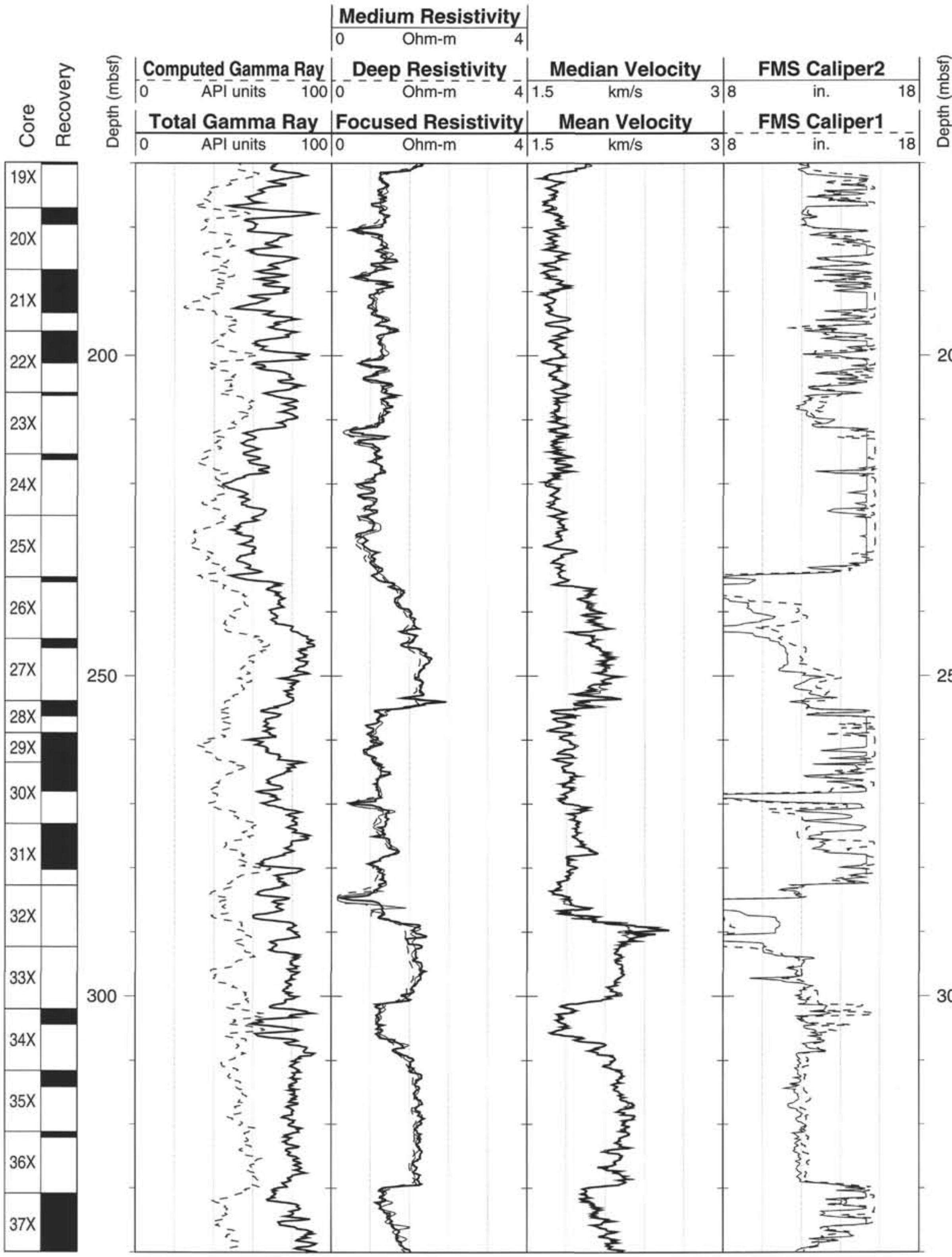

Hole 986C: Natural Gamma Ray-Resistivity-Sonic Logging Data (cont.)

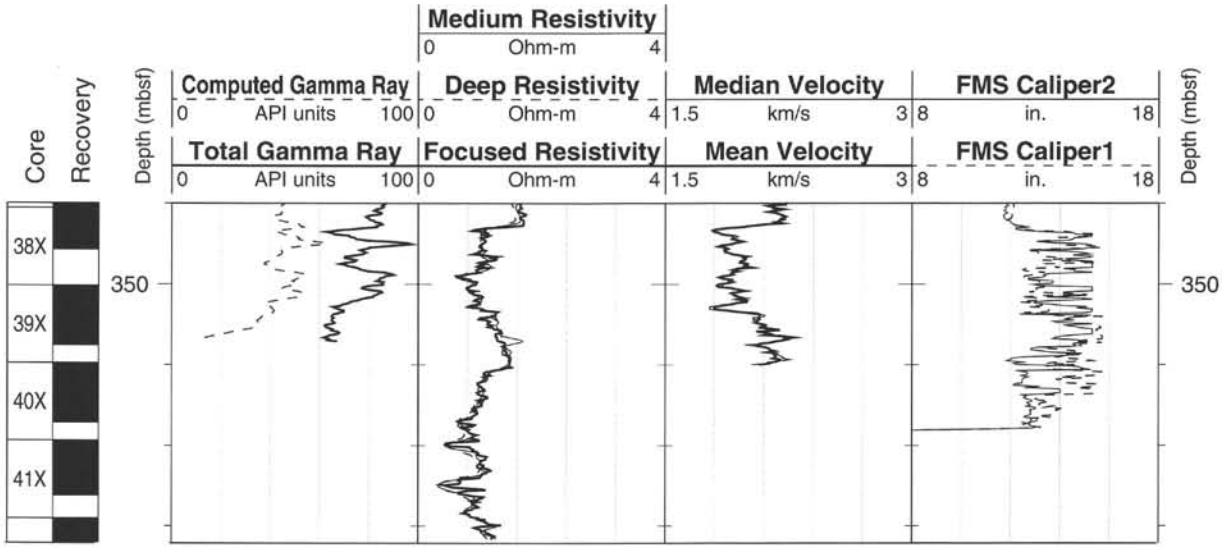

Hole 986C: Natural Gamma Ray-Density-Porosity Logging Data

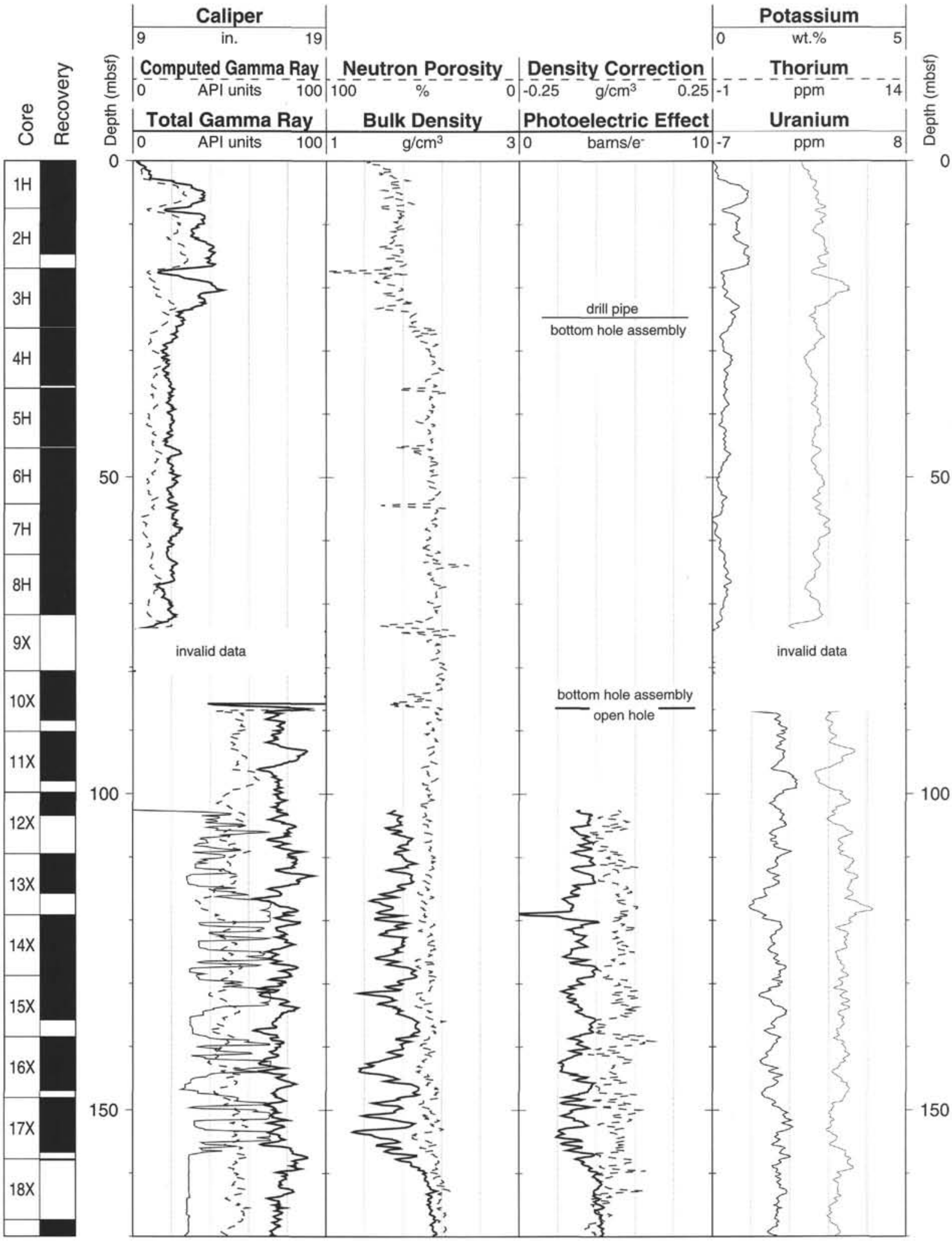

Hole 986C: Natural Gamma Ray-Density-Porosity Logging Data (cont.)

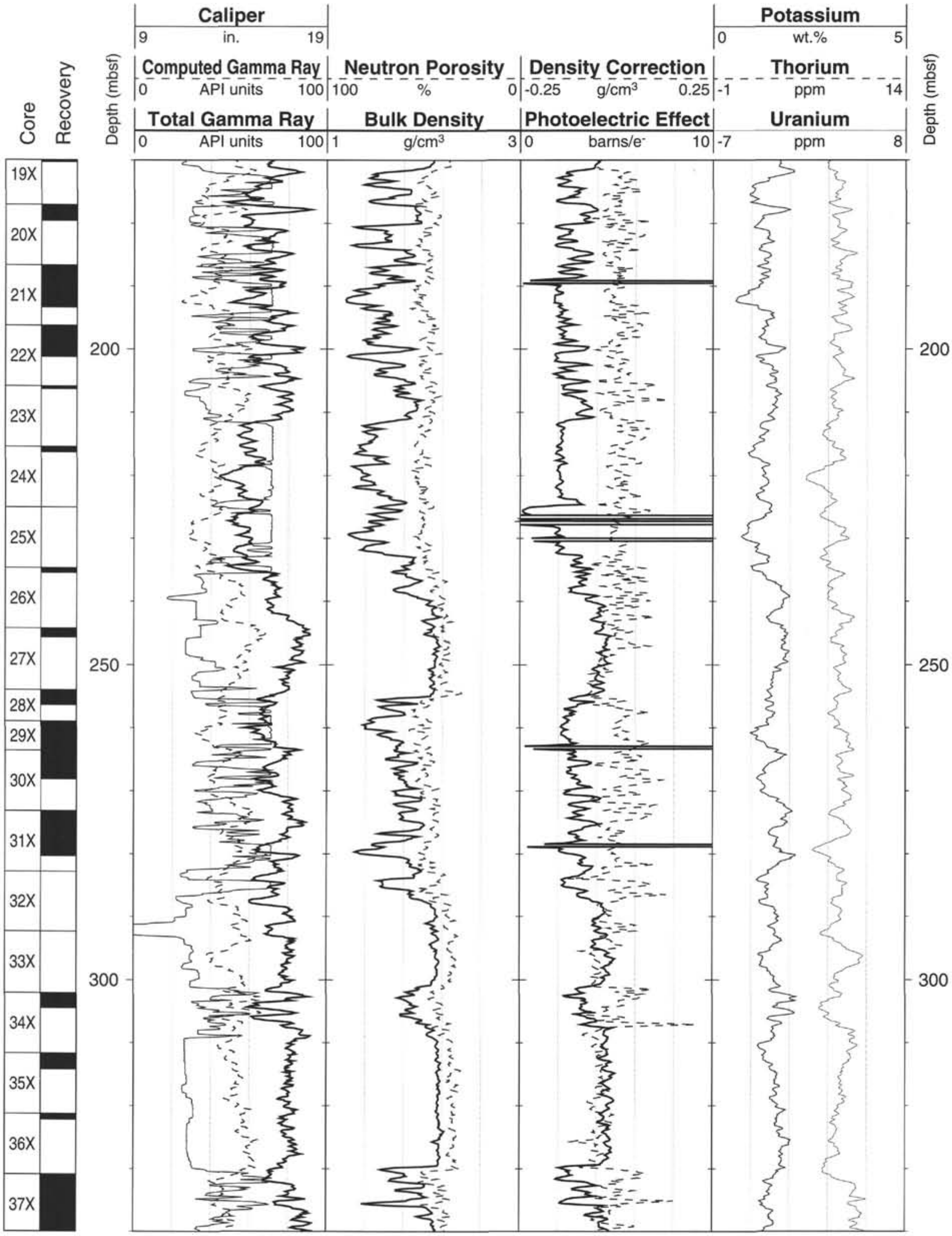

Hole 986C: Natural Gamma Ray-Density-Porosity Logging Data (cont.)

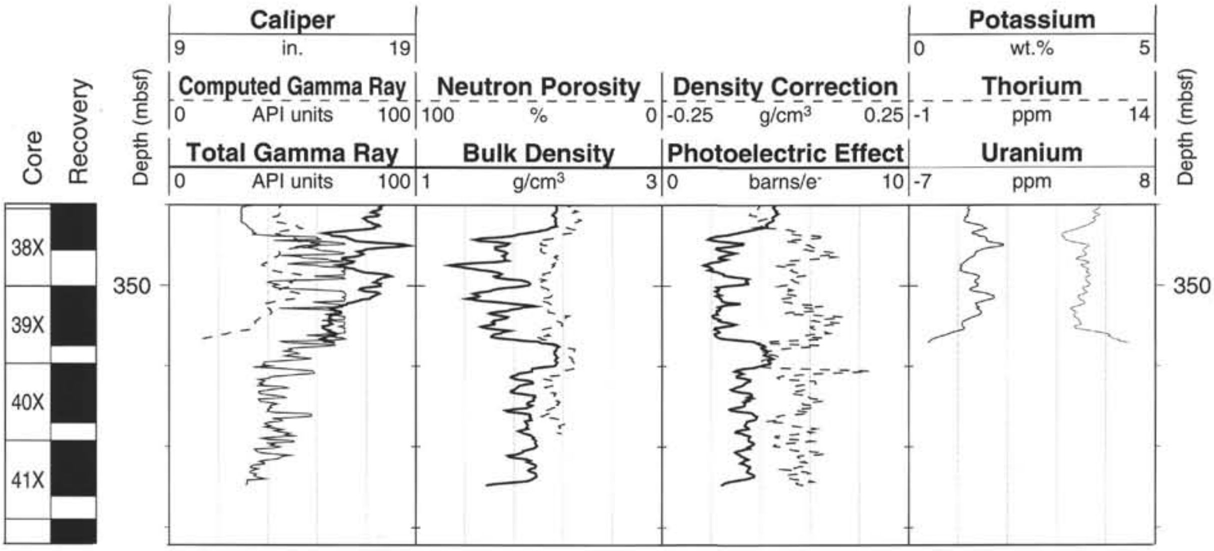

Hole 986D: Natural Gamma Ray-Resistivity-Sonic Logging Data

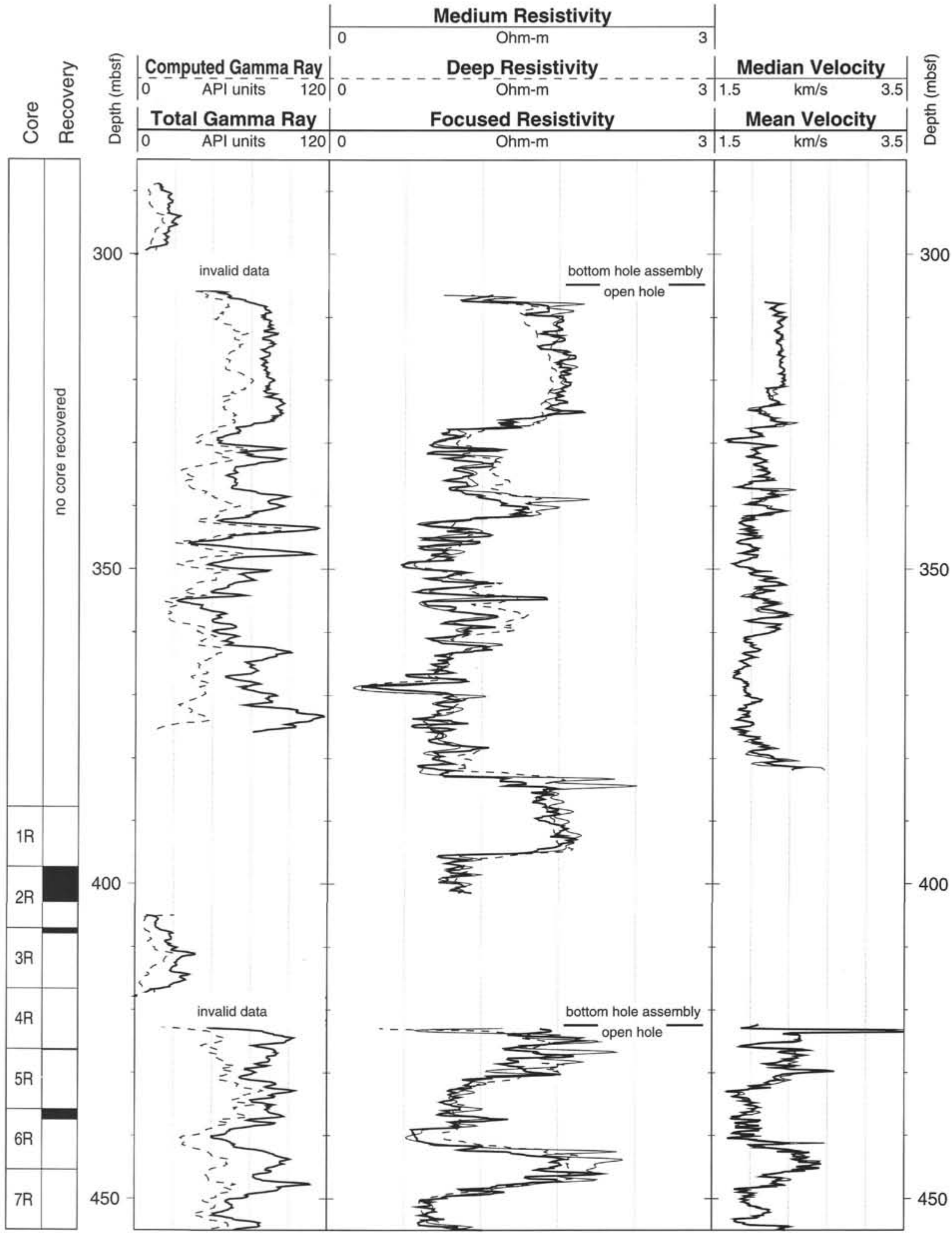

Hole 986D: Natural Gamma Ray-Resistivity-Sonic Logging Data (cont.)

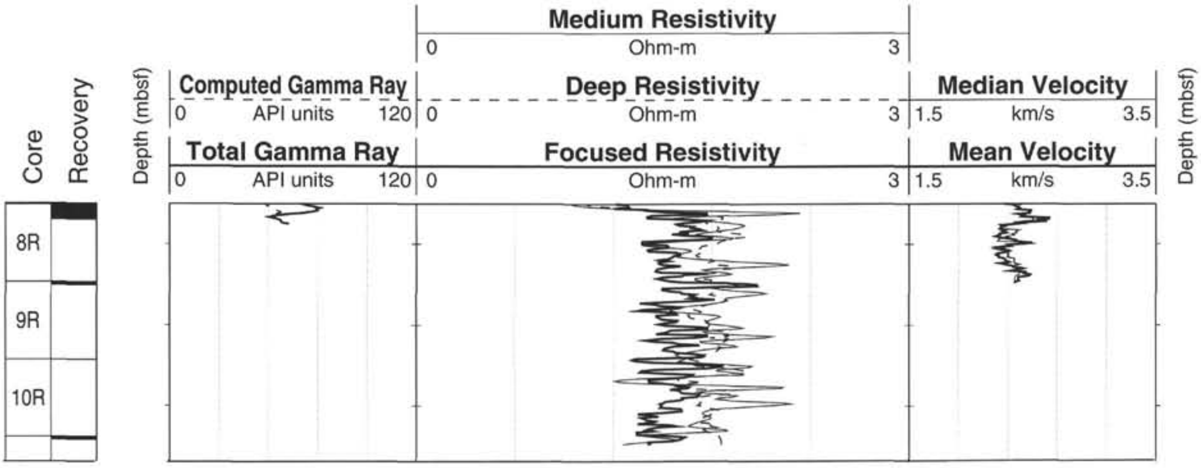

Hole 986D: Natural Gamma Ray-Density-Porosity Logging Data

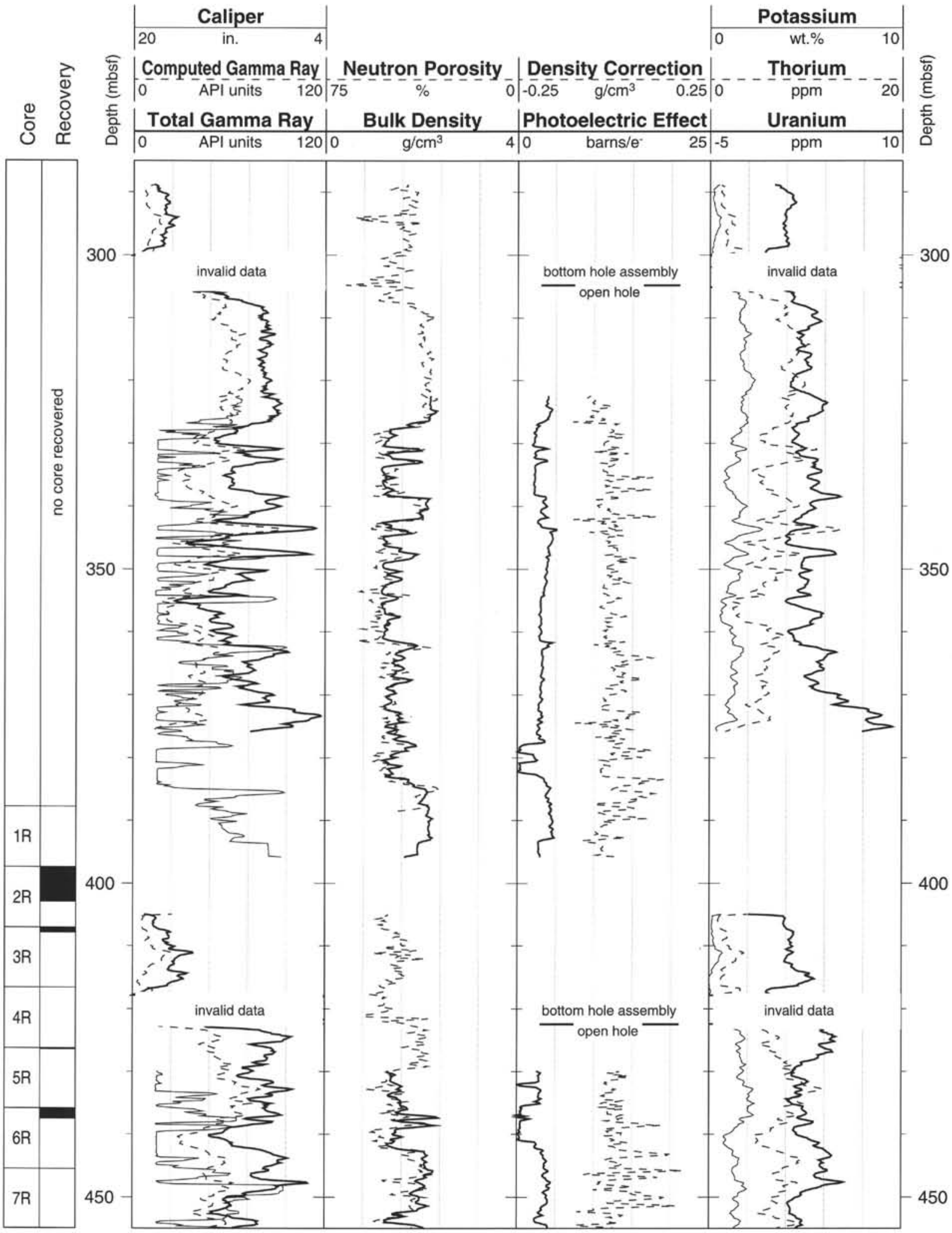

Hole 986D: Natural Gamma Ray-Density-Porosity Logging Data (cont.)